

THREE DIMENSIONAL RIGID-BODY IMPACT MECHANICS WITH FRICTION

BY HAN SUN

A dissertation submitted to the
Graduate School—New Brunswick
Rutgers, The State University of New Jersey
in partial fulfillment of the requirements
for the degree of
Doctor of Philosophy
Graduate Program in Mechanical and Aerospace Engineering

Written under the direction of
Professor Haim Baruh
and approved by

New Brunswick, New Jersey

October, 2017

ABSTRACT OF THE DISSERTATION

Three Dimensional Rigid-Body Impact Mechanics with Friction

by Han Sun

Dissertation Director: Professor Haim Baruh

By formulating the rigid-body impact model and deriving the post-impact dynamic quantities, a reliable computational model for analyzing two dimensional rigid-body impact with the ground is developed. The complicated structure of different objects and slide/stick/reverse slide conditions changing on ground suggested that the rigid body impact model should be used. And these three conditions are classified into seven impact cases. A two-dimensional experiment was conducted to validate the simulation impact model. Based on an experimental study on the impacts, and available experimental data in the literature, a validation study is conducted to ensure its accuracy.

After that, the impact computational model is extended into three dimensional rigid-body impact by formulating the governing equations. The seven cases are extended to eleven possible cases. Then the rigid-body impact analysis was concluded with three examples, ball, rod and bar, which validated the use of the two dimensional model for analyzing certain three dimensional impacts. Several examples were presented to study the influence of input parameters such as orientation angles, coefficient of friction and coefficient of restitution on post-impact dynamic quantities, case study and energy dissipation. After the discussion, we conclude that the characteristics of 3D impact follow closely those of two-dimensional impact.

A three-dimensional experiment is conducted to validate the computational impact model. For processing of impact image, Matlab programs are developed for image enhancement and motion capture. An error analysis is also performed to study the accuracy of the experiments. With the comparison between experiment and computational modeling, we observed that the simulation predictions were quite close to the experimental results with less than 10% error in the dissipation energy thereby validating our analysis.

Acknowledgements

First and foremost, I would like to express my sincere gratitude to my advisor, Prof. Haim Baruh for his continuous support of my PhD study and research. This dissertation is accomplished with his guidance in every aspect. It is his enthusiasm, professionalism and unrelenting pursuit of high-quality work that always pushed me forward to improve myself in academics. It is his tolerance, patience and consideration that has helped me overcome the difficulties during my PhD program. He has been a mentor of not only my academic life, but also my personal life. It is truly a fortune for me to have him as my Ph.D. advisor.

I would like to express my gratitude to my dissertation committee members: Professors Haym Benaroya, William J. Bottega and Dr. Joey Sanchez for their review of this dissertation. Their valuable comments and helpful suggestions helped to improve the clarity of this dissertation.

I would like to thank my colleague Qiming Guan, Kuo Chen, Fei Liu, Jiandong Meng and Sun Wong for their consistent helps and helpful discussions in our research, and especially for the experimental assistance provided to me. I would like to give special thanks to all my group members and friends in the United States for their support in the past years. Also, I would like to thank Department of Mechanical and Aerospace Engineering for the Graduate Fellowship and Teaching Assistantship for the past years. Also I would like to thank all the faculty members who taught me and staff members who helped me.

Finally, I would like to express heartfelt thanks to my dear wife, Xiaoting Liang, and to my lovely daughter, Olivia Sun, my parents, Huili Sun and Xiaoxia Yang. They were always there cheering me up and stood by me through the good times and bad.

Table of Contents

Abstract	ii
Acknowledgements	iv
List of Tables	x
List of Figures	xi
1. Introduction	1
1.1. Introduction	1
1.2. Literature Review	3
1.2.1. Basic Impact Theory	4
1.2.2. Discrete Contact Dynamics Models	6
General Formulation	7
Governing Equations A-Algebraic Equations	9
Governing Equations B-Integral–Differential Equations	9
Summary of Discrete Model	10
1.2.3. Continuous Contact Dynamics Model	11
Spring-Dashpot Model	13
Hertz’s Model	14
Non-linear Damping	15
1.2.4. Review of Contact Dynamics Models	16
1.2.5. Different Stages During Impact	17
1.2.6. Coefficient of Restitution (COR)	19
Newton’s Model	19
Poisson’s Model	19

Stronge's Model	20
1.2.7. Review of Experimental Verification	21
Coefficient of Restitution	22
Contact Stiffness and Damping	23
Tangential Coefficients	24
Validation of Contact Force Models	24
1.2.8. Summary	25
2. Planar Rigid Body Impact Mechanics	27
2.1. Description of Planar Rigid Body Impact Model	27
2.2. Dimensionless Governing Equations	30
2.3. Coefficient of Restitution (COR)	31
2.3.1. The Kinematic Model: Newton's model	32
2.3.2. The Impulsive Model: Poisson's model	32
2.3.3. The Energetic Model: Stronge's model	32
2.4. Tribology of Impact	33
2.4.1. Analytical Expression for Coefficient of Friction	35
2.4.2. Critical Value for Sliding	36
2.4.3. Critical Value for Reverse Sliding	37
2.4.4. Transition in Reverse Sliding and Sticking Mode	37
2.4.5. Coefficient of Static and Kinetic Friction	38
2.4.6. Summary	39
2.5. Cases of Impact	39
2.6. Summary of the Procedure	48
2.7. Energy Dissipation	49
2.8. Analysis of a Point-to-Line Impact Process-Impact of a Falling Rod with the Ground	50
2.8.1. Case Study	50
2.8.2. Energy Dissipation Study	53

2.8.3.	Special Values of μ and e_n on the Energy Loss	54
2.8.4.	Comparison for Different Friction Coefficient Models (μ_k and μ_s)	55
	Cases Comparison	55
	Energy Dissipation Comparison	56
2.8.5.	Discussion on choosing e_n among Newton's, Poisson's and Stronge's hypothesis	56
2.9.	Experimental Validation	59
	Single Camera Calibration	62
2.10.	Discussion and Conclusion	69
3.	Three Dimensional Rigid Body Impact Mechanics	71
3.1.	Description of Three Dimensional Rigid Body Impact Model	71
3.2.	Compression and Restitution stages conditions in Three Dimensions . .	75
3.3.	Calculation of rotated inertia matrix $[I_G^{xyz}]$	76
3.4.	Tribology of Impact in Three Dimensions	78
3.4.1.	Sticking Mode in Three Dimensions	79
3.4.2.	Sliding Mode in Three Dimensions	80
3.4.3.	Reverse Sliding Mode in Three Dimensions	81
3.5.	Cases of Impact	82
3.6.	Summary of the Procedure	82
3.7.	Numerical Examples	87
3.7.1.	Impact of a Falling Ball with the Ground	88
3.7.2.	Impact of a Rod with the Ground	95
	Sticking Mode	97
	Sliding Mode	98
	Reverse Sliding Mode	98
	Numerical Simulation Results	101
3.7.3.	Impact of a Rectangular Bar with the Ground	113
	Sliding, sticking and reverse sliding modes	116

Numerical simulation results	117
3.8. Discussion and Conclusion	120
4. Experimental Study for Three Dimensional Rigid Body Impact . . .	121
4.1. Experimental Set-up	121
4.1.1. Moving Objects	124
4.1.2. Dropping Device	125
4.1.3. Data Acquisition System	125
Camera Calibration	125
Synchronizing Cameras	127
4.1.4. Image Processing System	128
4.2. Video Recording and Image Processing	129
4.2.1. Setting and Synchronizing Cameras for Video Recording	129
4.2.2. Setting Reference Point on the Ground and Camera Calibration	130
Reference Point	130
Camera Calibration	130
4.2.3. Acquiring Displacement Information from Image Processing . . .	134
Image Enhancement	136
Object Tracking using Kalman Filter	136
4.2.4. Converting Displacement Information into a 3D(x, y, z) Reference	
Frame	137
4.2.5. Calculation of Pre- and Post-impact Dynamic Quantities	141
Dimensional Scale Factor C	141
Calculation for Dynamic Quantities	141
Calculation for Velocity	146
4.2.6. Flow Chart for a Single Impact Test	146
4.3. Error Analysis	148
4.4. Experiment Results for Coefficients of Friction and Restitution	151
4.4.1. Measuring Coefficients of Friction μ_s and μ_k	151

Measurement for Static Friction Coefficient μ_s	152
Measurement for Kinetic Friction Coefficient μ_k	152
4.4.2. Measuring Coefficient of Restitution e_n	155
4.4.3. Assumptions on Experimental Results	157
4.5. Comparison With Numerical Simulation Results	158
4.5.1. Rod Impact	158
4.5.2. Rectangle Bar Impact Experiments	166
5. Conclusions and Future Work	176
5.1. Summary of Key Results	176
5.2. Future Work	178

List of Tables

2.1. Conditions on different modes	39
2.2. Cases for two-dimensional impact	45
2.3. Parameters used in a single impact simulation	51
2.4. Parameters of camera 1	64
2.5. Quantitative comparison for two-body impact: $\mu = 0.195$	68
3.1. Cases for three-dimensional impact	83
3.2. Parameters used in a single impact simulation	88
4.1. Kinematic and dynamic parameters of the objects used in impact tests .	125
4.2. Intrinsic and Extrinsic Matrix of camera 1 and 2	135
4.3. Parameters of camera 1 and 2	136
4.4. Pre- and post-impact dynamic quantities for different tests on rod . . .	161
4.5. Pre- and post-impact dynamic quantities for different tests on rod . . .	162
4.6. Experiment validation for the rod with $\mu_s = 0.251$, $e_n = 0.292$	166
4.7. Pre- and post-impact dynamic quantities for different tests on bar . . .	167
4.8. Pre- and post-impact dynamic quantities for different tests on bar . . .	170
4.9. Experiment validation for the bar with $\mu_s = 0.416$, $e_n = 0.458$	175

List of Figures

1.1. Impact between two rigid bodies	4
1.2. Impact model for two rigid bodies	8
1.3. Change in velocity of particle with mass M resulting from impulse P . .	9
1.4. Contact force history for spring-dashpot model	13
1.5. Different stages during impact	18
2.1. Free body diagram of 2D model during impact	28
2.2. Special case in reverse sliding	38
2.3. Notation for different stages	40
2.4. Flow chart for compression impulse computation	46
2.5. Flow chart for restitution impulse computation	47
2.6. Falling rod colliding with ground	51
2.7. Seven cases variation with initial parameters γ and p	52
2.8. Influence of initial parameters γ and p on the energy loss contour	53
2.9. Influence of e_n and μ on the energy loss with $\gamma = \frac{5\pi}{4}$; reverse sliding; axisymmetric body	54
2.10. Influence of e_n and μ on the energy loss with $\gamma = \frac{3\pi}{4}$; sliding; axisym- metric body	55
2.11. Influence of initial parameters γ and p on cases contour with $\omega_z = 0$, $\mu_k = 0.4, \mu_s = 0.48$; with μ_s and μ_k models	56
2.12. Influence of initial parameters γ and p on the energy loss contour with $\omega_z = 0, \mu_k = 0.4, \mu_s = 0.48$; with μ_s and μ_k models	57
2.13. Newton's COR hypothesis	57
2.14. Poisson's COR hypothesis	58
2.15. Stronge's COR hypothesis	58

2.16. Schematic diagram of 2D Experiment platform	60
2.17. Experiment set-up	61
2.18. The rod	61
2.19. Image with identifications and green circles to indicate detected points	62
2.20. Camera 1 and pattern positions calculated in world coordinate	63
2.21. The bar graph of reprojection errors images	63
2.22. Comparison of original and undistorted images	64
2.23. Experiments A, B & C	67
3.1. Falling rod colliding with ground in three dimension	72
3.2. Rotations from xyz to XYZ coordinate	77
3.3. Tangential impulses in $x - z$ plane (the impact plane)	78
3.4. Reverse Sliding in (x, z) plane	81
3.5. 3D Flow chart for compression impulse computation	84
3.6. 3D Flow chart for restitution impulse computation	85
3.7. A bounce of a ball colliding with ground in three dimensions	89
3.8. Three cases variation with initial parameters v_x, ω_x, μ and e_n	93
3.9. Energy dissipation with initial parameters v_x, ω_x, μ and e_n	94
3.10. Falling rod colliding with ground in three dimensions	95
3.11. Flow Chart for Reverse Sliding in Compression	100
3.12. Example 1: Influence of initial velocity v_x on cases of impact with $\mu = 0$, $e_n = 1, v_x = -2 : 0.05 : 0$	102
3.13. Example 2: Influence of initial velocity v_x on cases of impact with $\mu = 1$, $e_n = 1, v_x = -2 : 0.05 : 0$	103
3.14. Examples 3: Influence of μ and e_n on (A) cases of impact, (B) energy dissipation $K_{dissipation}$, (C) post-impact velocity v'_x	105
3.15. Examples 4: Influence of μ and e_n on (A) cases of impact, (B) energy dissipation $K_{dissipation}$, (C) post-impact velocity v'_x	107
3.16. Influence of orientation angle β on energy dissipation $K_{dissipation}$ and cases of impact with $\mu = 0.4, e_n = 0.4$	108

3.17. Influence of orientation angle β and coefficient of friction μ on energy dissipation $K_{dissipation}$ and cases of impact with $e_n = 0.4$	110
3.18. Influence of orientation angle β and coefficient of restitution e_n on energy dissipation $K_{dissipation}$ and cases of impact with $\mu = 0.4$	112
3.19. Comparison of μ_k and μ_s models on energy dissipation $K_{dissipation}$, post impact velocity v'_x and cases with $e_n = 0.4$	114
3.20. Falling bar colliding with ground in three dimensions	115
3.21. Influence of initial velocity v_x and v_z on cases study and engergy dissipa- tion $K_{dissipation}$	118
3.22. Influence of initial velocity v_x and v_z on post-impact velocities v'_x, v'_z . .	119
3.23. Influence of initial velocity v_x and v_z on post-impact angular velocities ω'_x, ω'_z	119
4.1. Schematic diagram of 3D Experiment platform	122
4.2. Experiment set-up	123
4.3. Moving objects	124
4.4. Dropping device	126
4.5. Huawei Honor 8 with tripod	128
4.6. Images from 2 cameras before and after flash	128
4.7. Comparison 120fps with high resolution (800*450 pixels) image to 240fps with high resolution (640*480 pixels) image	129
4.8. Reference point on ground	130
4.9. Projective transformation between two images from stereo camera (rear view shown)	131
4.10. Checkerboard pattern	132
4.11. Example of checkerboard pattern placement	132
4.12. Checkerboard pattern detected from image	133
4.13. 3D view of cameras and pattern positions	133
4.14. Reprojection errors illustration	134
4.15. Reprojection errors in images	135

4.16. Image enhancement	137
4.17. Markers tagged in each frame	138
4.18. Position of markers and relative point O	138
4.19. Three markers positions data collected from 50 frames	140
4.20. Frame constructed using three markers	143
4.21. Examples of frame constructed using three markers positions	144
4.22. Schematic of the 2-1-3 motion in terms of the Euler angles $(\theta_1, \theta_2, \theta_3)$. .	144
4.23. Flow chart for one impact test	147
4.24. Large error occurs when object placed in large angle	149
4.25. Example of blurry marker boundry	149
4.26. Repeatability test on same experiment configurations	150
4.27. Relative position (x, y, z) of reference point to camera 1	151
4.28. Measuring static friction coefficient μ_s	153
4.29. Measuring kinetic friction coefficient μ_k	154
4.30. Drop test for measuring e_n	156
4.31. Impact example of a bar colliding with ground	157
4.32. Example A for rod	159
4.33. Example B for rod	160
4.34. Example C for rod	161
4.35. Example D for rod	163
4.36. Example E for rod	164
4.37. Experiments F for rod	165
4.38. Example A for bar	168
4.39. Example B for bar	169
4.40. Example C for bar	170
4.41. Example D for bar	171
4.42. Example E for bar	173
4.43. Example F for bar	174

Chapter 1

Introduction

1.1 Introduction

Impulse-based manipulation is an area in robotics where little work [58, 59] has appeared. An impulsive force has a very short execution time, and thus good potential of application in improving task efficiency. Its use could considerably simplify the robotic mechanism needed to perform a manipulation task, while avoiding uncertainties accumulated over repeated complex operations. Despite this advantage and many potential applications, impulsive manipulation has remained an under-explored area in robotics with little known work (Higuchi [60]; Izumi and Kitaka [61]; Hirai [62]; Huang and Mason [59]; Han and Park [38]; Tagawa [58]).

Efforts on impact analysis have struggled over the consistencies between laws of Coulomb’s friction and energy conservation, and Poisson’s impulse-based hypothesis of restitution. Routh’s graphical method [15] to construct the impulse trajectory has proven successful for analyzing two-dimensional impacts, and has been later extended by various researchers [63, 6, 16]. For three-dimensional impact, Darboux [46] was the first to describe impact dynamics in terms of normal impulse in the form of a differential equation. His result was later rediscovered by Keller [5] who also used the equation’s solution to determine the varying slip direction. These efforts have neglected the effect of tangential compliance and assumed that all work done by the tangential reaction force is lost to friction. When tangential compliance is not negligible, however, part of the work is converted into recoverable internal energy, despite the loss of the remaining part to friction. The approaches [19, 20], designed to produce a ratio of tangential to normal impulse equal to the coefficient of friction, did not exactly follow Coulomb’s law of friction. Stronge [18] developed a lumped parameter representation of compliance,

and applied a time-dependent analysis to track the change in the tangential velocity during a collision. His model could predict slip or stick at the contact under Coulomb's law. However, without knowing the duration of impact, the analysis can only be used to perceive contact modes qualitatively rather than to carry out specific computation. Recently, Jia [37, 44] provided an method on studying modeling of tangential compliance as two rigid bodies collide in the space. In his paper [44], Stronge's spring-based contact structure is extended to three dimensions. Slip or stick is indicated by the tangential motion of a mass connected to the contact point (viewed as an infinitesimal region) on one body via three orthogonal springs.

Overall, computation of tangential impulse is the key to solving an impact problem and the focus of this dissertation. We extend the structure of Stronge's linear model of planar impact with compliance to develop a theory for three-dimensional impact that is based on normal impulse only and consistent with both laws of Coulomb friction and energy conservation.

In this dissertation, we focus on studying rigid-body impact with friction. This three-dimensional impact problem usually requires numerical simulations. We have investigated two-dimensional and three-dimensional problems in both fundamental understanding, relevance to applications and experimental validation.

1. We developed a general analysis for 2D rigid-body impact model. The main contribution is that we present both analytical and numerical approaches which includes three different types of coefficient of restitution models. In addition, to validate these models, we have also conducted a series of experiments, which follow closely to our simulation results and analytical conclusions.
2. We developed a numerical analysis for three-dimensional impacts. The analysis is general by assuming the objects in impact are rigid-bodies. The effects of coefficient parameters and initial dynamic quantities are systematically analyzed taking advantage of the explicit formulae on their influences.
3. Extending from task two above, we have also constructed an three-dimensional

impact experiment platform with high standard of accuracy and test-retest reliability. Numerical simulation results are directly compared with these experimental measurements to reveal good quantitative agreements. Such experiment validation is previously not available for impulse-momentum manipulation. Similarly, the results provide predictions in quantitative agreements with experimental data, and physical insights on sliding/reverse sliding behavior and friction properties.

1.2 Literature Review

The nature of impact in a multibody system is complex as abrupt changes occur in the system momenta and velocities. This is not solely due to the impulsive forces of the colliding bodies but also involves the changes in the reaction forces or impulses associated with the kinematic joints. Impact problems are best studied utilizing a piecewise or discontinuous analysis approach. In this approach, the integration of the equations of motion is halted at the time of impact. A momentum balance is then performed to evaluate the velocity jumps. The integration is resumed with the updated velocities until the next impact occurs. This piecewise analysis methodology has been used in previous work by Wittenburg [1], Wehage [2], and Khulief [3]. These studies are restricted to direct central or frictionless impact. The presence of friction at the contact points or surfaces makes the problem more complicated as the friction may lead to different modes of impact such as sticking, sliding, or reverse sliding. The inclusion of friction in the impact analysis has been addressed by Whittaker [4], Keller [5], Han and Gilmore [6] and Jean and Moreau [7], but not extended to jointed mechanical systems. These studies use the coefficient of friction μ and coefficient of restitution e_n as known quantities. The corresponding momentum and impulse-balance equations contain the velocity changes and two impulse components, one in the normal and the other in the tangential directions of the impacting surfaces. Therefore, to solve the impulse-momentum equations, two additional conditions are needed. One condition comes from Coulomb's law of friction, while the other comes from the definition of the coefficient of restitution [8, 9].

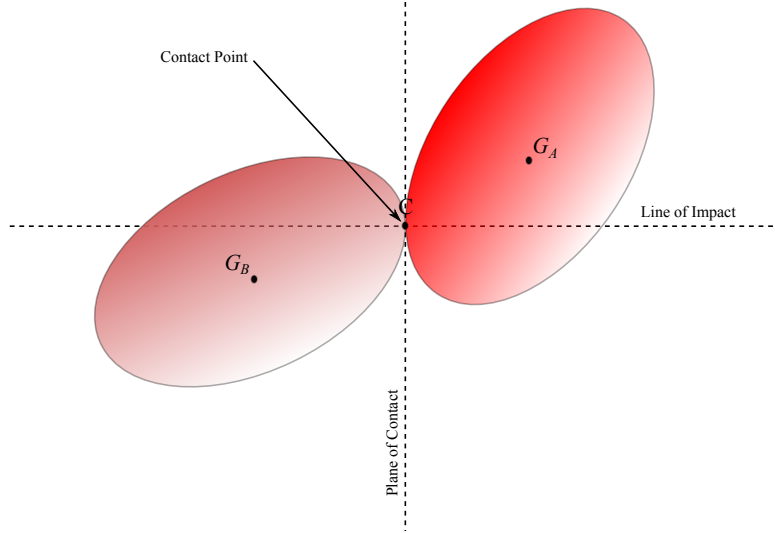


Figure 1.1: Impact between two rigid bodies

1.2.1 Basic Impact Theory

Contact is an ambiguous term although it is frequently used interchangeably with impact. In our work, we use the term *contact* to describe situations where two or more bodies touch each other at some location as shown in Figure (1.1). Inherently, contact implies a continuous process which takes place over a finite time.

In general, two different approaches can be distinguished for impact and contact analysis. The first approach assumes that the interaction between the objects occurs in a short time and that the configuration of impacting bodies does not change significantly. The dynamic analysis is divided mainly in two intervals, before and after impact, and in secondary phases during impact, such as sliding, sticking and reverse sliding. To model the process of energy transfer and dissipation, various coefficients are employed, mainly the coefficient of restitution and the impulse ratio [10, 11]. Application of these methods, referred to as impulse-momentum or discrete methods [12], has been confined primarily to impact between rigid bodies. The extension to flexible systems as well as extension to more general cases involving multiple contacts and intermittent contact is more complicated.

The second approach is based on the fact that the interaction forces act in a continuous manner during the impact. Thus, the analysis may be performed in the usual

way, by simply adding the contact forces to the equations of motion during their action period. This allows for a better description of the real behavior of the system, in particular, with respect to friction modeling. More importantly, this approach is naturally suitable for contact modeling and complex contact scenarios involving multiple contacts and bodies. This approach is referred to as continuous analysis or force-based methods [12].

In the following section, we present basic concepts and definitions used in impact theory. This is followed by a general historical overview of the research on impact and contact dynamics modeling. The overview begins and extends with the initial models of Newton, Poisson and Stronge through to the modern formulations capable of dealing with complex contact scenarios. Given the complexity of impact modeling, it is preferable that results obtained from theoretical analysis are confirmed with experimental measurements. Furthermore, as in any modeling of reality, the quality of the model depends on the choice and accuracy of model parameters. The last section of the dissertation is devoted to experimental model validation and identification of impact/contact parameters.

It is important to emphasize that the literature on contact/impact analysis is vast and that it spans many diverse disciplines. Our review focuses on contact (and impact) dynamics, rather than contact mechanics treatments of the subject. The latter traditionally aims to solve for stress and displacement distributions, as well as the wave propagation problem. Analytical results are often sought for ‘simple’ geometry and material combinations of the contacting bodies, such as two spheres with identical elastic constants or impact of a mass on an elastic half-space. In addition, contact mechanics solutions are obtained for a known loading condition, as in the case of the classical Cattaneo problem [13], where the normal loading is held fixed while the tangential load is increased monotonically. Jaeger [14] presents an excellent overview of several contact mechanics analysis. In distinction, contact dynamics models tend to deal with, not surprisingly, dynamic quantities such as forces, impulses and velocities of the contacting bodies. Being motivated by space robotic applications, our review favors the works presenting general contact dynamics formulations for multi-body systems.

1.2.2 Discrete Contact Dynamics Models

The impact between two rigid bodies was analyzed initially by Sir Isaac Newton, and expanded by Whittaker [4] to account for frictional impulse. In that model the coefficient of restitution is a kinematic property that defines a relationship between the normal components of the velocities before and after the impact at the contact point (referred to as Newton’s model). Routh [15] presented a graphic method based on a kinetic hypothesis to define the coefficient of restitution (referred to as Poisson’s model). The coefficient of restitution is defined as a kinetic quantity that relates the normal impulses that occur during the compression and restitution phases. The two approaches are also different in the treatment of the motion in the tangential direction during impact. In Routh’s study, the possibility of changes in slip direction during contact is taken into account, while in Whittaker’s study it is not. In many simple cases, the two approaches lead to the same result, as shown by Wang and Mason [16], while in other cases, they can produce inconsistent results, as shown by Stronge [17]. This is a consequence of the possible changes in the slip direction. Ignoring these can lead to the overestimation of the final velocity after the impact, as illustrated with the Newtonian and Poisson’s approach for a perfectly elastic impact [18].

Brach [19, 11] proposed an algebraic solution scheme, revising Newton’s model and introducing impulse ratios to describe the behavior in the tangential directions. He defined the tangential impulse as a constant fraction of the normal impulse—the constant ratio of the two being the impulse ratio. This model is equivalent to the friction coefficient in many cases. Brach also demonstrated that work-energy and kinematic constraints impose an upper bound on the impulse ratio. He also expanded this approach to include the impulse moments. Alternatively, the motion in the tangential direction was described by using the tangential coefficient of restitution. Smith [20] proposed another purely algebraic approach to the problem using the Newtonian definition for the coefficient of restitution. Impulse ratio is determined using an average value of different slipping velocities. Keller [5] developed an approach which involves the integration of

the contact impulse variables. Thus, the system is treated as an evolving process parameterized by a cumulative normal impulse. Also, by using a revised Poisson's model, Keller concluded that no increase in energy is possible during impact. Using Routh's graphical method to analyze the contact models, Wang and Mason [16] identified the impact conditions under which Newton's and Poisson's models give the same solution. Stronge [18] demonstrated the energy inconsistencies in some solutions obtained with Poisson's model when the coefficient of restitution is assumed to be independent of the coefficient of friction. In that case, Poisson's model does not lead to vanishing dissipation for a perfectly elastic impact. As a result, Stronge proposed to define the coefficient of restitution as the square root of the ratio of the elastic strain energy released during restitution to the energy absorbed by deformation during compression. With this definition, no energetic inconsistencies are present [14].

General Formulation

The discrete formulation [16] is based on the assumptions that the impact process is instantaneous and impact forces are impulsive, kinetic variables have discontinuous changes while no displacements occur during the impact, and that other finite forces are negligible. This model is used mainly if the impact involves rigid or very hard and compact bodies, while the effects of deformation at the contact point are taken into account through coefficients. The impact problem is solved by using the linear impulse-momentum principle, the angular impulse-momentum principle, and the kinematic relations between the variables before and after impact [10, 11]. As shown in Figure (1.2), if m is the mass, \vec{v} velocity of the center of mass, \vec{P} the linear impulse due to impact, \vec{H} the angular momentum about the center of mass, \vec{R} the vector from the center of mass to the point of impact and \vec{M} the angular impulse due to impact, the impact dynamics equations are

$$m_A(\vec{v}'_A - \vec{v}_A) = \vec{P} \quad (1.1)$$

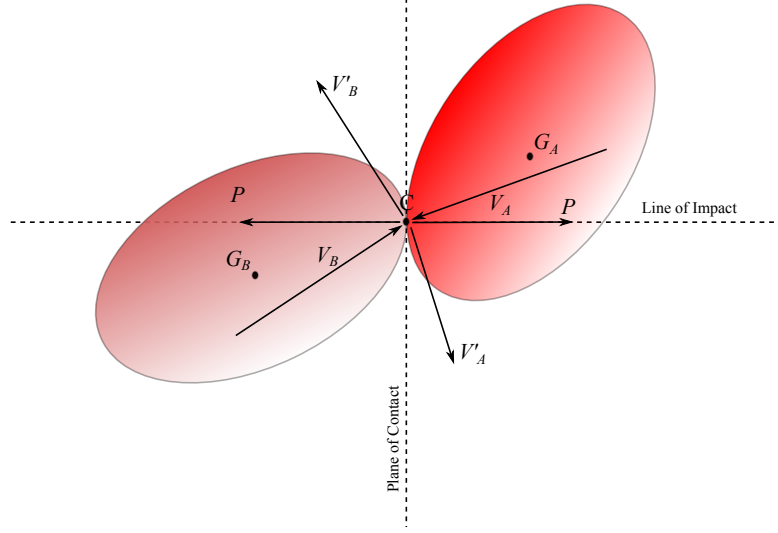


Figure 1.2: Impact model for two rigid bodies

$$m_B(\vec{v}'_B - \vec{v}_B) = -\vec{P} \quad (1.2)$$

$$\vec{H}'_A - \vec{H}_A = \vec{R}_A \times \vec{P} + \vec{M} \quad (1.3)$$

$$\vec{H}'_B - \vec{H}_B = \vec{R}_B \times \vec{P} - \vec{M} \quad (1.4)$$

In the above equations, indexes A and B specify the body, while subscript $()'$ denotes the post-impact conditions. The unknowns are the linear and angular velocities of the two bodies and the impulses P and M . The angular impulse M is neglected in the majority of formulations since, consequently to the basic assumptions, the contact region must be small. Additional relations are required to solve for the unknown impact variables. For the normal direction, one relation is provided by the coefficient of restitution. In the tangential direction, the relational laws may have to be replaced with kinematic constraints (for instance, during sticking, zero tangential velocity is imposed).

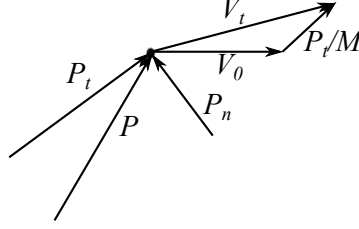


Figure 1.3: Change in velocity of particle with mass M resulting from impulse P

Governing Equations A-Algebraic Equations

Using Newton's or Poisson's models to define the coefficients of restitution in any direction (or about any axes), purely algebraic equations are obtained. Together with the impulse ratios, these equations can be written in the form

$$e = e(P, M, v), \quad \mu = \mu(P, M) \quad (1.5)$$

Examples of analytical solutions of Eqns. (1.5) can be found in Brach [19, 11], and Smith [20]. Lagrange's equations describing impact between two rigid bodies are presented in [21]. These formulations solve for generalized coordinates, the Lagrange multipliers associated with impact forces (or normal impulses) and the friction forces due to stiction. This approach has also been applied by some authors to flexible-body systems (see, for example, Kulief and Shabana [22], Yigit et al. [23]). In this case, the coefficient of restitution value for relatively compact bodies must be used with care as it may be affected by the flexibility.

Governing Equations B-Integral-Differential Equations

Another approach to solving the impact problem is to think of the impact as an evolving process parameterized by cumulative normal impulse [5, 24]. An application of this approach is reported by Keller [5], where Poisson's model of restitution is used. Stronge [18] employs a similar analytical method to investigate changes in relative velocity, but with the use of the energy aspect of coefficient of restitution. The linear impulse \vec{P} is divided into two components shown in Figure (1.3), normal and tangential, given by:

$$P_n(t) = \int_0^t \vec{F}_C(s) \cdot \vec{n} ds = \int_0^t \vec{F}_n ds \quad (1.6)$$

$$P_t = - \int_0^{t_f} \mu \vec{F}_n t dt = - \int_0^{P_f} \mu \vec{t} dP_n = - \int_0^{(1+e)P_m} \mu \vec{t} dP_n \quad (1.7)$$

\vec{F}_C is the force at contact point. The normal component P_n is used as an independent variable. The solution of the impact problem is reduced to determining P_t , as well as the variation in the slip direction specified by the tangential unit vector \vec{t} . The differential equation for the tangential component can be integrated to solve for the tangential impulse defined in Eqs. (1.6)-(1.7).

Summary of Discrete Model

As implied by the discussion above, the definition of restitution is a key aspect of the discrete formulation of impact dynamics. Three theories of restitution have been proposed to date and it is appropriate to discuss how they compare against each other. In particular, energy dissipation analysis of a planar impact of two bodies [16] leads to the following conclusions:

1. The three restitution models are equivalent if there is no friction, or there is friction but the motion along the tangential direction does not stop (i.e., there is no reverse sliding).
2. If friction is present and the impact is eccentric, the normal velocity during and at the end of impact depends on the direction of slip. Since Newton's model does not differentiate between the possible contact modes, it neglects the change in the slip direction.
3. Poisson's and Stronge's models dissipate more energy than Newton's model, and this energy is always positive. However, it is different for the two when sticking or reverse motion is present.
4. Newton's and Poisson's models are inconsistent when $e_n = 1$ since, for this case, they can produce non-zero energy dissipation in the normal direction.

It has been suggested that a way to resolve some of the problems with the existing

restitution models is to allow an interdependency between the coefficients of restitution and friction [11]. Nevertheless, at this time, it appears that Stronge's hypothesis of restitution is the most accurate of the three theories.

Another important aspect of discrete models is the use of Coulomb's law to model friction during impact. Several authors have noted the inconsistencies that arise when rigid body models are used with Coulomb's empirical law of friction. Examples are described by Wang and Kumar [25] where the aforementioned inconsistencies are demonstrated by either no feasible solution or by multiple solutions for particular initial conditions. This has been attributed to the approximate nature of Coulomb's model and to the inadequacy of the rigid body model, but no clear explanation has been found.

Finally, we observe once again that the discrete models are based on the assumption that impact time is small and the bodies involved in the impact are mainly rigid. The use of these models with flexible bodies is not straightforward because of the "rigid body" concept of the coefficient of restitution [23]. However, the results presented in [26] for transverse impact of a rotating flexible beam demonstrate relatively little sensitivity to the coefficient of restitution. The application of discrete modeling to contact scenarios such as robotic insertion tasks envisioned for the space station is not straightforward. In these cases, the approach velocities are small and there is time-varying contact between the fixture and the mating object at many points. To deal with the multiplicity of contact points would require additional assumptions regarding the order of impulses [18, 27, 10].

1.2.3 Continuous Contact Dynamics Model

Application of impulse-momentum methods to model the impact dynamics of rigid bodies leads to several problems. First, in the presence of Coulomb friction, cases arise in which no solution or multiple solutions exist. Examples and analysis of these inconsistencies can be found in Wang and Kumar [25] and Mason and Wang [16]. The second problem is that energy conservation principles may be violated during frictional impacts, as shown by Stronge [18], as a consequence of the definition of the coefficient of restitution. Finally, the discrete approach is not easily extendable to generic multi-body

systems. The use of compliance or continuous contact models where the impact force is a function of local indentation can overcome the problems encountered in the discrete formulation [25, 28].

Different models have been postulated to represent the interaction force at the surfaces of two contacting bodies [10]. The first model was developed by Hertz [29], in which an elastostatic theory was used to calculate local indentation without the use of damping. The corresponding relationship between the impact force and the indentation is allowed to be non-linear. In the first and simplest model of damping, referred to as spring-dashpot model [30], the contact force is related to a linear spring-damper element. Hunt and Crossley [8] showed that a linear damping model does not truthfully represent the physical nature of the energy transfer process. Thus, they proposed a model based on Hertz's theory of contact with a non-linear damping force defined in terms of local penetration and the corresponding rate. Lee and Wang [31] proposed a similar model, but with a different function specifying the non-linear damping term. Other damping models have been proposed to describe totally or partially plastic impacts [19, 11, 10, 18].

Contact stiffness and damping forces are dependent, at the minimum, on two parameters—the coefficient of stiffness and the coefficient of damping. For simple contact between two bodies, the coefficient of stiffness is determined by the geometry and the material of the contacting objects, while the coefficient of damping can be related to the coefficient of restitution [32]. An important advantage of continuous contact dynamics analysis is the possibility of using one of many friction models available in the literature. Different models have been developed to permit a smooth transition from sticking to sliding friction [28, 33]. Non-linear models, as well as non-local models, have been used to represent the behavior of the surface irregularities that cause the friction. The use of continuous model for contact forces allows one to generalize the contact dynamics methodology to multi-body/multi-contact scenarios, as well as contact involving flexible bodies [34, 12, 33].

The continuous model, also referred to as compliant contact model, overcomes the problems associated with the discrete models. The basis of the continuous formulation for contact dynamics is to explicitly account for the deformation of the bodies during

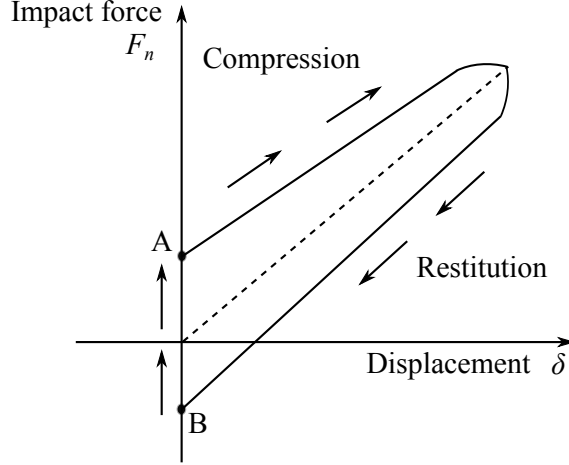


Figure 1.4: Contact force history for spring-dashpot model

impact or contact. In a large class of continuous models, referred here as explicit modes, this is done by defining the normal contact force F_n as an explicit function of local indentation δ and its rate, i.e., [19]:

$$F_n = F_n(\dot{\delta}, \delta) = F_{\dot{\delta}}(\dot{\delta}) + F_{\delta}(\delta) \quad (1.8)$$

In the following, we summarize three existing contact force models, including the initial model of Hertz [29] and the non-linear damping model of Hunt and Crossley [8].

Spring-Dashpot Model

The impact is schematically represented with a linear damper (dashpot) for the dissipation of energy in parallel with a linear spring for the elastic behavior [35]. The contact force is defined as [19, 11] and is represented schematically in Figure (1.4).

$$F_n = b\dot{\delta} + k\delta \quad (1.9)$$

This model has three shortcomings [36]:

1. The contact force at the beginning of impact (point A) is discontinuous, because of the damping term. In a more realistic model, both elastic and damping forces should be initially at zero and increase over time.

2. As the impacting objects are separating (point B), i.e., the indentation tends to zero, their relative velocity tends to be negative. As a result, a negative force holding the objects together is present.

3. The equivalent coefficient of restitution defined for this model does not depend on impact velocity. As we discuss in Section 4, velocity dependence of e has been demonstrated experimentally [35].

Although the spring-dashpot model is not physically realistic, its simplicity has made it a popular choice [37, 38, 28]. This model provides a reasonable method for capturing the energy dissipation associated with the normal forces without explicitly considering plastic deformation issues.

Hertz's Model

The Hertz's model is a non-linear model, however it is limited to impacts with elastic deformation and it does not include damping in its original form. With this model, the contact process can be pictured as two rigid bodies interacting via a non-linear elastic spring along the line of impact. The hypotheses states that the deformation is concentrated in the vicinity of the contact area, elastic wave motion is neglected, and the total mass of each body moves with the velocity of its mass center. The impact force is defined as [35, 39]

$$F_n = k\delta^n \tag{1.10}$$

where k and n are constants, depending on material and geometric properties and computed by using elastostatic theory. For instance, in the case of two spheres in central impact, $n = \frac{3}{2}$ and k is defined in terms of Poisson's ratios, Young's moduli and the radii of the two spheres [32]. Since the Hertzian model does not account for energy dissipation, its equivalent coefficient of restitution is one. Therefore, this model can be used only for low impact speeds and infinitesimal (local) deformation.

The elastic contact law of Hertz can be augmented to account for plastic deformation by introducing hysteresis in the contact force law. This can be accomplished by using

a different force indentation relationship for the unloading phase of the contact which generally takes the following form [40]:

$$F_n = F_{n,max} \left(\frac{\delta - \delta_p}{\delta_{max} - \delta_p} \right)^n \quad (1.11)$$

In Eqn. (1.11), $F_{n,max}$ and δ_{max} are the maximum normal force and indentation reached during the loading phase and δ_p is the permanent indentation. Note that in the context of contact dynamics simulation, the maximum quantities in Eqn. (1.11) can be calculated at every instant of the numerical integration. By contrast, the value of δ_p must be specified as an additional parameter in this contact force model. The hysteretic force law of Eqn. (1.11) has not been previously applied to solve multi-body contact scenarios, partly because it is somewhat cumbersome to implement and the plastic deformation per se is unimportant in the majority of applications.

Non-linear Damping

To overcome the problems of the spring-dashpot model and to retain the advantages of the Hertz's model, an alternative model for energy dissipation was introduced by Hunt and Crossley [8]. It includes a non-linear damping term and hence the impact/contact force is modeled as

$$F_n = -(\lambda x^n) \dot{x} - kx^n \quad (1.12)$$

where x is penetration, \dot{x} is penetration velocity, k is the spring constant and λ is the damping constant and power n is often close to one and depends on the surface geometry of the contact. As with the spring-dashpot model, the damping constant λ can be related to the coefficient of restitution e , since both are related to the energy dissipated by the impact process. For the central impact of two bodies Hunt and Crossley [8], Lankarani and Nikravesh [32], and Marhefka and Orin [36] established the relations

$$e = 1 - \alpha \dot{\delta}_0, \quad \alpha = \frac{2\lambda}{3k} \quad (1.13)$$

An important aspect of this model is that damping depends on the indentation. This is physically sound since the contact area increases with deformation and a plastic region is more likely to develop for larger indentations. Another advantage is that the contact force has no discontinuities at initial contact and separation, but it begins and finishes with the correct value of zero. This model has been studied and used by several authors [23, 1, 41, 42, 38, 43, 44].

1.2.4 Review of Contact Dynamics Models

In a recent review of contact mechanics with an emphasis on the development of energy absorbing material [45], various constitutive relations related to impact mechanics were examined. Analytical models for impact mechanics were classified into four categories:

1. Models based on rigid-body dynamics,
2. Models for propagation of stress waves in perfectly elastic materials,
3. Models for propagation of stress waves through solids that are not perfectly elastic, such as shock and plastic waves,
4. Non-local or non-classical models that describe spallation and fragmentation upon impact.

In general, multibody mechanical systems represent mechanisms, machines, and articulated structures, which may experience collisions/impacts during their functional usage without subjecting components to deformations in the plastic range. Accordingly, most researchers in the area of multibody mechanical systems have tackled the problem of modeling impact with two primary contact configurations: (a) rigid-body contact, and (b) elastic-body contact. In rigid-body contact, one assumes that when the impact force is applied to a point in a body, all of the points in that body are instantaneously set in motion and the relative distances between any two material points never change. This rigid-body dynamics model is based on the impulse-momentum law for rigid bodies, attuned with the conditions of elastic and inelastic restitution [30]. In contrast, the actual impact generates stress waves that propagate strain energy away from the region

of impact. If the energy transformed into elastic vibrations accounts for an appreciable amount of the total energy, the rigid-body dynamics model is no longer applicable and the approach based on elastic body contact is more suitable. In general, the multidimensional aspect of wave propagation and the description of stress distribution at the zone of contact are not considered in impact formulations using macroscopic laws commonly adopted in multibody formulations. In the next section, the key studies for modeling impact in multidimensional systems will be reviewed.

1.2.5 Different Stages During Impact

The classical theory of rigid-body impact is primarily based on impulse-momentum balance relations and does not involve mathematical difficulties. However, it is inadequate for describing the resulting deformations and the associated transient stress wave propagation [27]. The classical theory further assumes that a negligible amount of the system's kinetic energy is transformed into vibrations of the colliding bodies. This hypothesis has been found by Stronge [40] to be reasonably valid for the collision of bulky objects, e.g., the collision of two spheres or a sphere against a large rigid mass. However, it is inadequate for collisions involving elastic beams and thin plates. It is important to note that the classical theory of rigid-body impact does not take the shape of the contacting surfaces into consideration.

For the perfectly elastic two-body collision between smooth surfaces, the impulse-momentum and conservation of mechanical energy laws are sufficient to determine the post-impact velocities. However, when impacts produce some indentation or permanent deformation, the law of conservation of energy is replaced by the restitution relationship. The coefficient of restitution is introduced to account for energy dissipation during the impact process.

The dynamics of impact is a complex event, depending on many properties of contacting bodies such as material, geometry and velocity. In general, two stages can be identified during impact: compression and restitution [18], as shown in Figure (1.5). The first stage begins when the two bodies come in contact at the instant t_0 (point O), and ends when the maximum deformation is reached at the instant t_m (point A), at

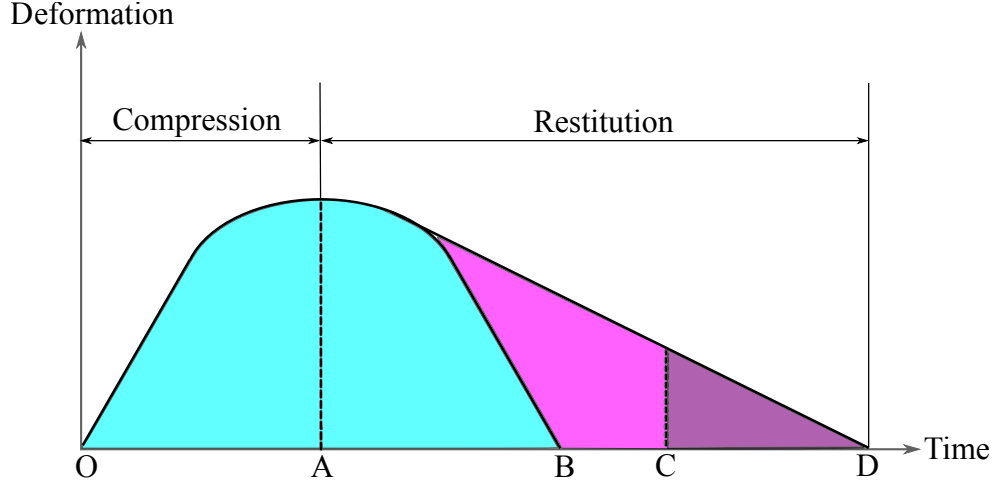


Figure 1.5: Different stages during impact

which point the relative normal velocity at the contact point is zero. The second phase begins at t_m and ends when the two bodies separate, i.e., instant t_f (points B , C or D).

For impacts with sufficiently high velocities, not all of the deformation is recoverable because of the permanent (plastic) deformation and the resulting energy loss. With respect to the latter, impact can also be classified into: (a) perfectly elastic, curve $O \rightsquigarrow A \rightsquigarrow B$, where no energy is lost; (b) perfectly plastic, curve $O \rightsquigarrow A$, where all energy is lost and the deformation is permanent; (c) partially elastic, curve $O \rightsquigarrow A \rightsquigarrow D$, with energy loss but no permanent deformation; (d) partially plastic, described by $O \rightsquigarrow A \rightsquigarrow C$, with energy loss and permanent deformation. The objective of impact modeling is to determine the after-impact conditions of the system, given its initial (pre-impact) configuration. Because of the complex dependencies on many parameters, one possible solution is to use experimentally measured coefficients. Coefficient of restitution, defined along the normal direction, and friction coefficients defined along the tangential directions are the most important [9].

1.2.6 Coefficient of Restitution (COR)

In multibody dynamics modeling and analysis, researchers back to 1800s [46] have leaned towards treating impact via macroscopic laws. Accordingly, they treated the impact between two mechanical components using some macroscopic laws that relate motion parameters before and after impact, without explicit modeling of the mechanics of contact for the case of compliant bodies. In this subsection, some basic laws, such as Newton's or Poisson's restitution, are extended to include situations when there is friction and slip during impact.

The coefficient of restitution is a non-dimensional parameter. This coefficient can take on values in the range $0 \leq e_n \leq 1$, where $e_n = 1$ denotes a completely elastic impact and $e_n = 0$ denotes a completely plastic impact. A coefficient of restitution greater than one is theoretically possible, representing a collision that generates kinetic energy, such as land mines being thrown together and exploding. A coefficient of restitution less than zero would represent a collision in which the separation velocity of the objects has the same direction (sgn) as the closing velocity, implying the objects passed through one another without fully engaging. This may also be thought of as an incomplete transfer of momentum.

Newton's Model

In Newton's model [4], the coefficient of restitution is defined as

$$e_n = -\frac{v_f \cdot \mathbf{n}}{v_0 \cdot \mathbf{n}} \quad (1.14)$$

This model is based on a kinematic point of view. The coefficient of restitution e_n is the negative ratio of initial and final values of normal velocity at the contact point C .

Poisson's Model

In Poisson's model [15], the total normal impulsive force P^f is divided in two parts, P^c and P^r corresponding to compression and restitution phases, respectively. The coefficient of restitution is defined as [16]

$$e_n = \frac{P^r}{P^c} \quad (1.15)$$

where

$$P^f = P^c + P^r \quad (1.16)$$

The condition for the end of the compression phase is zero relative velocity along the normal direction. That is, $\vec{V} \cdot \mathbf{n} = 0$. The parameter P_n is the impulsive force along the normal direction and P_t is the impulsive force along tangential direction.

Using this definition, and Eqns. (1.1,1.2,1.3,1.4) and (1.15,1.16), it is possible to define the line of termination as:

$$v_0 + \frac{v_1}{1+e}P_n + v_2P_t = 0 \quad (1.17)$$

where v_0 is the approach velocity, v_1 and v_2 are parameters depending on initial conditions, geometry and inertia [16].

Stronge's Model

To obtain non-frictional energy dissipation for elastic collisions, Stronge[17, 47] proposes a different relation between impulses for the restitution and compression phases of the collision. The coefficient of restitution is defined as the square root of the ratio of energy released during restitution, W_r , to the energy absorbed during compression, W_c . This definition explicitly relates the coefficient of restitution e to the dissipation by irreversible deformation processes. With this definition, e is independent of the friction coefficient. In terms of the work done by the normal force during the two phases, the coefficient of restitution can be calculated from:

$$e_n^2 = \frac{W_r}{-W_c} \quad (1.18)$$

It can be shown that the energy hypothesis leads to the only model which ensures that the energy loss from sources other than friction is non-negative, and is zero when

$e_n = 1$ among these models. In [17], Stronge applies the above definition to derive a theoretical expression for e_n in terms of W_c and the work required to initiate yield. In [40], Stronge considers the problem of oblique impact of a rigid cylinder on a deformable half-space. It is noted that in this and similar cases of collisions between objects of very different sizes, the energy loss caused by material damping to stress waves W_w is substantial and can be accounted for with the following definition of the coefficient of restitution:

$$e_n^2 = \frac{W_r - W_w}{-W_c} \quad (1.19)$$

where

$$W_w = \int_{-\infty}^{\infty} 2aP(t) \frac{d\bar{u}}{dt} dt \quad (1.20)$$

and \bar{u} is the mean normal displacement of the free surface of a semi-infinite body subjected to an oscillating surface pressure $Pe^{i\omega t}$ that acts on a strip of width $2a$.

1.2.7 Review of Experimental Verification

The complexity of impact dynamics requires verification through experiments. Experimental validation can be applied to two aspects: the first being a validation of the basic theories of coefficients or contact force models, while the second is a validation of the overall contact dynamics simulation. Also, parameters characterizing the impact are required to be determined by experimental measurements or by other means. For discrete models, this involves determination of the coefficient of restitution, while for continuous models, contact stiffness and damping are needed. Both modelling approaches also use one or several parameters to define the coefficient of friction μ .

Much of the experimental work related to impact/contact dynamics has focused on measuring model parameters and verifying the contact force models. The main results are summarized in the following subsections.

Coefficient of Restitution

The principal and most general study of the coefficient of restitution is due to Goldsmith [30], who measured the displacements of the impacting bodies, the duration of impact, the geometry of the crater and the stress waves generated by the impact. Using the initial impact velocity and the measured displacements, the final (post-impact) velocity was calculated and used to compute the coefficient of restitution and impact velocity for a direct central impact of two spheres. The experimental data was used to find the dependencies between different quantities such as coefficient of restitution and the initial impact velocity, as well as to check the limits of the known impact theories. Results obtained for the coefficient of restitution clearly demonstrated the dependence of this parameter on the geometry and material of the impacting bodies, as well as on the initial impact geometry and velocity. More specifically, the coefficient of restitution decreases with the increase of the initial impact velocity, and for most materials, it is significantly smaller than unity, even at very low impact speeds. This implies that Hertz's theory [29] of perfectly elastic impact is not valid in most impact situations and that some plastic deformation always takes place. As a conclusion, Goldsmith [30] states that Hertz's theory provides a good description for impact of two spheres or a sphere and a plate, if the materials are hard and the initial speed is low. Under more general conditions, plastic deformation and/or energy loss associated with wave propagation should be taken into account.

Based on the studies reported by Goldsmith, it is possible to establish the following relationship:

$$e = 1 - \alpha \dot{\delta}_0^m \quad (1.21)$$

where the parameter α and the exponent m are dependent on the material properties and geometry of the impact of bodies. Other researchers have measured e for specific contact situations, such as measurement for glass particles with two different diameters at different relative velocities and liquid layer thicknesses [48]. Another example is Wang [49], who studied particles of maize, including wedged particles, quadrature particles and

round particles impacting on the oblique wall. All experiments demonstrate that the coefficient of restitution depends on many properties and impact characteristics, in addition to the material properties of impacting bodies. It is therefore difficult to use this parameter to model complex impact scenarios with multiple-point contacts.

Contact Stiffness and Damping

Contact stiffness and damping, also known as contact parameters, are used to define the contact force law in the explicit continuous formulation of impact dynamics. Although this model is conceptually simple, the physical meaning of contact parameters is not obvious, and thus it is not straightforward to define their values for complex contact scenarios. This is particularly true for robotic insertions where the contacting bodies—parts to be mated—are subcomponents of a multi-body chain, which itself may comprise many compliant and dissipative elements. In such situations, the characteristics of impact are very much determined by the relative compliance and damping of local (contact) regions, the structural flexibility and damping of the contacting bodies and/or other constituents of the system. Nevertheless, for simple impact geometries, one can use an analytical approach to estimate the contact parameters. For example, one can calculate the contact stiffness by applying Hertz’ theory of contact [39]. For contact damping, one can use the energy-balance to find a relationship between contact damping and the coefficient of restitution [36], although, inevitably, such a result is limited by the accuracy of the coefficient of restitution.

An alternative estimation of contact stiffness was used in Van Vliet et al. [50] for a relatively complex case of a peg contacting a wall. There, the contact stiffness was calculated by using the stiffness of the most compliant element of the wall—the load cells between the hole sides and the fixed support. Possibly the most practical approach is to determine the contact parameters by direct experimental measurements. Some research in this area has been carried out in the robotics community where several identification algorithms have been developed to estimate the stiffness of the robot environment [51]. As done by [48, 49], one can always tune the parameter values used in the numerical simulation to achieve agreement with the experimental results.

Tangential Coefficients

Extension of experiments to oblique impacts allows a verification of tangential models, in particular, Coulomb's model of friction as well as tangential compliance [43, 37, 44]. The former is effectively done by measuring the coefficient of friction for different impact geometries and demonstrating that it is approximately constant [52, 53]. Results indicate the presence of two main zones. In the first zone, the initial tangential velocity is low (i.e., the angle of incidence is high) and the impulse ratio increases rapidly. In this zone, both slipping and sticking is possible. In the second zone, the tangential velocity is high (i.e., the angle of incidence is low). For any tangential velocity in this zone, only slipping is present until the termination of impact. In this zone, the coefficient of friction decreases slowly with increase in tangential velocity.

Validation of Contact Force Models

It is difficult to make general statements on the validity of discrete impact dynamics models. It is commonly said that they depend on the applicability of the rigid-body hypothesis, more specifically, whether it is reasonable to neglect deformations at the contact point. Discrete models have been used, however, to predict the impact dynamics of flexible bodies, such as flexible beams [49,50,52,53]. The strong dependency of the energy lost transferred to vibrations of the contacting bodies has been confirmed. Although the discrete formulation is capable of capturing the energy loss—through the coefficient of restitution—this parameter depends on many factors and it is difficult to use for general impact scenarios. If the rigid body hypothesis is not applicable, a continuous contact model can be used. The non-linear contact force model has been validated experimentally by using flexible beams, as in [43,56,64]. It was shown that the dynamic behavior of the system is not sensitive to the value of the damping coefficient over a wide range. Comparison of simulated and measured velocities of the contact point shows good agreement, especially for low speed impact.

1.2.8 Summary

This chapter reviewed the state of the art on the subject of impact and contact dynamics modeling. Models were classified in two categories: impulse-momentum (or discrete) and continuous. In the former, the impact analysis is divided into discrete events and energy dissipation is accounted for via coefficient of restitution and the impulse ratio. In the continuous approach, a dynamics analysis is conducted continuously, by admitting (explicitly or implicitly) a relationship between contact force and deformation.

The discrete formulation has been applied mainly to rigid-body collisions since its main premise is the rigid-body hypothesis which imposes a limit on the energy loss. Definition of the coefficient of restitution is a key aspect of the discrete approach and three such definitions exist in the literature. Closed-form solutions for simple impact geometries demonstrate that, under general impact conditions, the three models of restitution do not produce the same results. Moreover, Newton's and Poisson's models may produce solutions which are energetically inconsistent. Naturally, predictions of the discrete impact analysis depend on the accuracy of the coefficient of restitution. However, experiments have proven that this parameter depends on many impact characteristics, which makes accurate estimation very difficult. The use of the coefficient of restitution for impacts involving flexible bodies is precarious. Various solution methods to solve the discrete impact dynamics equations have been presented, as well as the generalization of the methodology to multi-body systems subjected to multiple contacts. It was noted that the discrete formulation is not easily extendible to handle general impact scenarios, more specifically those where impacts occur at many points in the system. Finally, the necessary use of Coulomb's law with the discrete approach may lead to inconsistencies or multiple solutions.

The continuous approach has several advantages over the discrete formulation. More importantly, it does not require one to differentiate between impact and contact situations, and it permits the use of solution methods employed for non-impact dynamics problems. The approach extends quite naturally to contact scenarios with multiple

bodies and/or multiple points of contact. The added complexity of the minimum distance/interference determination problem seems minimal when compared to making ad hoc assumptions on the impulse histories at different contact locations. Different models for contact force have been presented and, as noted by several researchers and verified experimentally, the model with a non-linear damping term represents quite well the real behavior of the system during impact. Unlike the discrete formulation, the continuous approach allows for use of any friction model. Two principal solution methods were identified by Gilardi [54] in the context of continuous formulation; explicit and implicit. The latter is typically used in conjunction with a finite-element discretization of the contacting bodies.

Chapter 2

Planar Rigid Body Impact Mechanics

In impact study, we often begin the analysis with the rigid body model of impact. The rigid body assumption is primarily made to obtain a simple model. However, its utility should not be underestimated. In this chapter, we show that a great deal of useful information can be found from this model. The simplicity comes from lumping all of the pertinent impact parameters into a few coefficients. The main concern is whether single-valued coefficients can be used for a range of initial conditions. In the literature, numerous experiments have been devised to study the applicability of the model and they will be discussed later in this chapter. As the name suggests, we are assuming that the impacting bodies do not deform during impact and that the impact itself is instantaneous. Although it becomes impossible to determine the motion of the bodies during impact and our solutions consist of post impact velocities and angular velocities, we can still apply rigid-body impact theory to a lot of useful problems.

2.1 Description of Planar Rigid Body Impact Model

In this subsection we discuss developing the tools to analyze planar rigid body impact. We take into account that frictional effects can no longer be neglected. A good example to such impact is in almost every sport that utilizes a ball. The planar impact assumption restricts the initial angular velocity to only have a component about an axis perpendicular to the plane defined by the components of the initial velocity referred to here as the $x - y$ plane. We begin the analysis by introducing an arbitrary body in a Cartesian coordinate system oriented such that the horizontal or x -axis is tangent to the surface at the point of impact C .

Consider a rigid body of mass m and centroidal moment of inertia I_G making impact

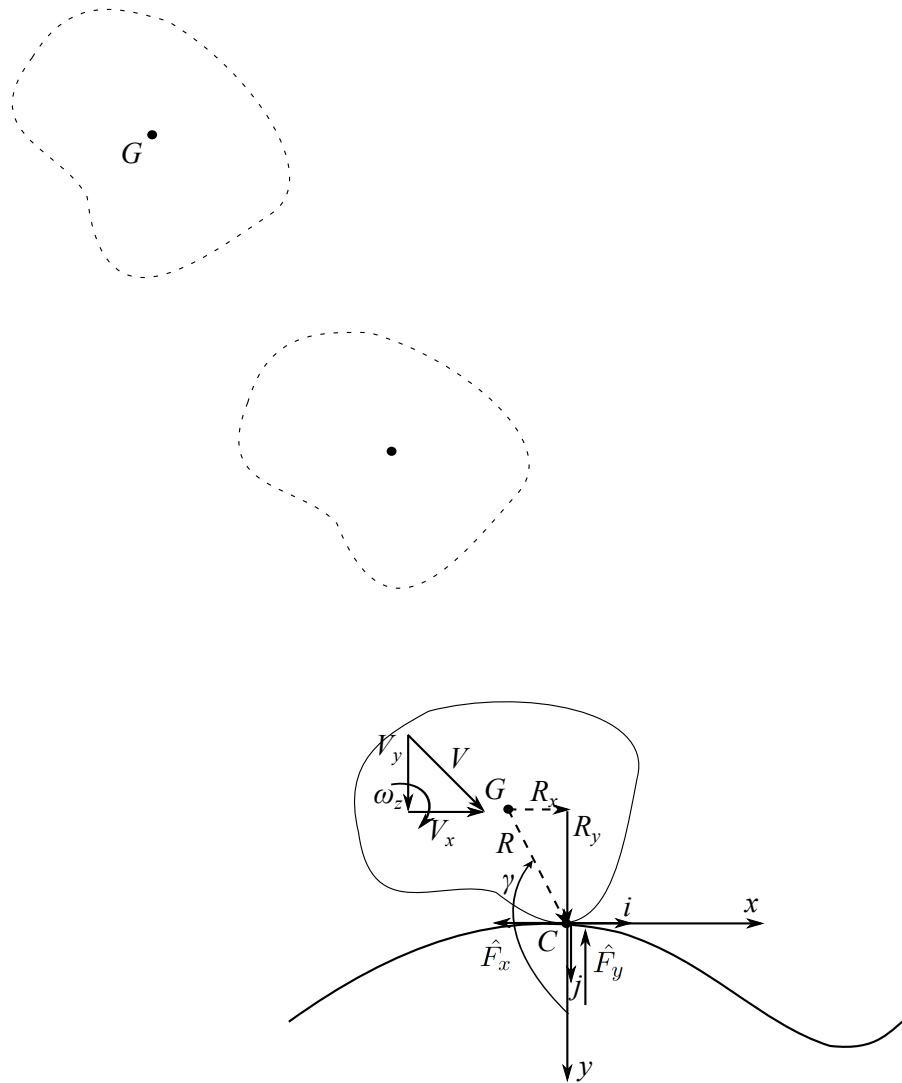


Figure 2.1: Free body diagram of 2D model during impact

with a surface. The orientation is shown in Figure (2.1), where C is the impact point. Since the impact is two-dimensional, there will be only two forces between the object and the impacting surface, the vertical impact force as well as the horizontal friction force acting at the contact point C . We assume that the gravitational force is negligible during impact since it is non-impulsive and in most cases its magnitude is miniscule compared to the large impact force. Therefore, we do not consider the gravitational force in the linear impulse-momentum equation. Also, the direction of the tangential force indicates that the object is traveling in the positive x direction, since friction always opposes motion. The position vector of the contact point with respect to the center of mass is defined by an angle γ from the positive y -axis. This angle will be taken positive clockwise. We express this position vector as

$$\vec{R} = R_x \vec{i} + R_y \vec{j} \quad R_x = -R \sin(\gamma) \quad R_y = R \cos(\gamma) \quad (2.1)$$

The velocity of the center of mass and angular velocity immediately before impact are

$$\vec{v} = v_x \vec{i} + v_y \vec{j} \quad \omega = \omega_z \vec{k} \quad (2.2)$$

The contact point velocity \vec{v}_C at the beginning of impact is

$$\vec{v}_C = \vec{v} + \vec{\omega} \times \vec{R} = (v_x - \omega_z R_x) \vec{i} + (v_y + \omega_z R_y) \vec{j} \quad (2.3)$$

The post-impact or final velocity of the center of mass, angular velocity and contact point velocity will be denoted by a prime in the superscript. The coefficient of friction between the object and impact surface is denoted by μ . During impact an impulsive normal force \hat{F}_y acts in the vertical direction (upwards) and impulsive friction force \hat{F}_x acts in the horizontal direction. Assuming that the impact takes place in a very short period of time, the linear and angular impulse-momentum relationships can be written

as

$$mv_x + \hat{F}_x = mv'_x \quad (2.4)$$

$$mv_y + \hat{F}_y = mv'_y \quad (2.5)$$

$$I_G\omega + \hat{F}_x R_y + \hat{F}_y R_x = I_G\omega' \quad (2.6)$$

where $I_G = amR^2$ is the moment of inertia about the center of mass, G , and the coefficient a depends on the geometry of the impacting body.

2.2 Dimensionless Governing Equations

One can improve the understanding and parametrization of the governing equations of rigid body impact by nondimensionalizing. We will nondimensionalize all velocity quantities with respect to the vertical component of the initial velocity. This allows the use of these equations for vertical impacts, even when the horizontal component of the initial velocity vanishes. We define the following dimensionless pre-impact quantities:

$$p_x = \frac{v_x}{v_y} \quad p_y = \frac{v_y}{v_y} = 1 \quad \lambda_z = \frac{\omega_z R}{v_y} \quad (2.7)$$

Similarly, we nondimensionalize the post-impact quantities and denote them with same notation as before, with a prime.

$$v'_x = \frac{v'_x}{v_y} \quad v'_y = \frac{v'_y}{v_y} \quad \omega' = \frac{\omega'_z R}{v_y} \quad (2.8)$$

The dimensionless representations of the impact impulses and the moment of inertia are

$$\hat{F}'_x = \frac{\hat{F}_x}{mv_y} \quad \hat{F}'_y = \frac{\hat{F}_y}{mv_y} \quad a = \frac{I_G}{mR^2} \quad (2.9)$$

Dividing the linear momentum equations by mv_y and the angular momentum Equation by mR^2 , we obtain the dimensionless representations as

$$p + \hat{F}'_x = v'_x \quad (2.10)$$

$$1 + \hat{F}'_y = v'_y \quad (2.11)$$

$$a\lambda_z - \hat{F}'_x \cos(\gamma) + \hat{F}'_y \sin(\gamma) = a\omega' \quad (2.12)$$

So far, we have obtained the governing equations for rigid body impact. The three Eqns. (2.10,2.11,2.12) do not form a closed system because there are five unknowns: three post-impact velocities v'_x , v'_y , ω' and two impulsive forces \hat{F}'_x , \hat{F}'_y . We need two more equations which will be derived in the following subsections.

2.3 Coefficient of Restitution (COR)

One of the hardest feats to accomplish in any impact analysis is to accurately represent the impact force. The simplest way is to model the gross effects of the impact force rather than try to obtain its transient representation. This is where we introduce the coefficient of restitution based on different models such as Newton's, Poisson's and Stronge's hypotheses. In each model, the equation defining the COR is known as the "Impact Law".

These common models for the Coefficient of Restitution are stated in the subsections that follow,

2.3.1 The Kinematic Model: Newton's model

The definition can be attributed to Newton and stated mathematically as

$$e_n = -\frac{\vec{V}_C' \cdot \vec{j}}{\vec{V}_C \cdot \vec{j}} \quad (2.13)$$

where e_n is the coefficient of restitution, and the subscript $()_n$ denotes the direction normal to the impact surface. In this case, the direction of the unit normal vector is \vec{j} . The negative sign in Eqn. (2.13) guarantees a positive value for the coefficient of restitution in the case when velocity reversal or energy absorption occurs. Putting Eqn. (2.13) in dimensionless form gives

$$e_n = -\frac{v_y' + \omega_z' R_x}{1 + \lambda_z R_x} \quad (2.14)$$

2.3.2 The Impulsive Model: Poisson's model

The definition can be attributed to Poisson and stated mathematically as

$$e_n = \frac{P^r}{P^c} \quad (2.15)$$

where P^r and P^c are the normal impulses during the restitution and the compression stages, respectively. Putting Eqn. (2.15) in dimensionless form gives

$$e_n = \frac{\hat{F}_y^r}{\hat{F}_y^c} \quad (2.16)$$

where \hat{F}_y^r and \hat{F}_y^c are the normal impulsive force during the restitution and compression stages, respectively.

2.3.3 The Energetic Model: Stronge's model

This definition is attributed to Stronge [17] and stated mathematically as

$$e_n^2 = \frac{W^r}{-W^c} \quad (2.17)$$

where

$$W^c = \int_0^{\delta_c} F_y^c(\delta) \cdot d\delta = \int_0^{t_c} F_y^c \cdot \frac{1}{2}(v_{cy} - v_{cy}^c) dt \quad (2.18)$$

$$W^r = \int_0^{\delta_r} F_y^r(\delta) \cdot d\delta = \int_{t_c}^{t_r} F_y^r \cdot \frac{1}{2}(v_{cy}^c - v_{cy}^r) dt \quad (2.19)$$

and t_c and t_r are the ending time of the compression and restitution stages. δ_c and δ_r are the relative maximum deflections of the contact surface at the end of compression and restitution, respectively. v_{cy} , v_{cy}^c and v_{cy}^r are the contact point velocities at the beginning of impact, end of compression and end of restitution, respectively. W^c and W^r are the work done by the normal contact force during the compression and the restitution stages, respectively. If we assume the normal force changes linearly, we can substitute Eqn. (2.5) into Eqn. (2.18) and Eqn. (2.19) to get

$$W^c = \frac{1}{2}(v_{cy} - v_{cy}^c)\hat{F}_y^c = \frac{(\hat{F}_y^c)^2}{2m} \quad (2.20)$$

$$W^r = \frac{1}{2}(v_{cy}^c - v_{cy}^r)\hat{F}_y^r = \frac{(\hat{F}_y^r)^2}{2m} \quad (2.21)$$

Finally, we can get the COR based on Stronge's model as below:

$$e_n^2 = \frac{(v_{cy}^c - v_{cy}^r)\hat{F}_y^r}{(v_{cy} - v_{cy}^c)\hat{F}_y^c} = \frac{(\hat{F}_y^c)^2}{(\hat{F}_y^r)^2} \quad (2.22)$$

Note that, for a object that is a spherical shell, such as a ball, velocity v_{cy} at contact point C can be replaced by velocity v_y at gravitational center G since the impulsive normal force acts along the line $C - G$.

2.4 Tribology of Impact

Friction is an important part of rigid body impact. It governs the transfer of linear momentum to angular momentum and hence all post-impact quantities. According to

the Coulomb Law of Friction [9], the coefficient of friction μ can be defined as the absolute value of the ratio of horizontal to vertical impulse components. This relationship is depicted below as

$$\mu = \left| \frac{\hat{F}_x}{\hat{F}_y} \right| \quad (2.23)$$

where μ is called the coefficient of friction. The above expression governs the relationship between the impulses if sliding occurs. It will also be shown to be the condition required for sliding to initiate. We can nondimensionalize the right side of Eqn. (2.23) with respect to mv_y which leads to

$$\mu = \left| \frac{\hat{F}'_x}{\hat{F}'_y} \right| \quad (2.24)$$

The coefficient of friction is a function of the mechanical properties of both contacting surfaces. It has also been shown that for some objects it can depend on the sliding velocity [55, 56], which is the relative speed between the contact point and the impact surface. Furthermore, the friction force can even reverse its direction during impact [10, 6, 1]. But, as was stated previously in the section on rigid body analysis of impact, we are only concerned with the gross effects of friction.

This dissertation considers the three extremes of frictional effects during impact. One possibility will be that the impacting body pivots during impact, referred to as *sticking*, which is the case when the impulse ratio is less than the critical value governed by Eqn. (2.24) and hence the object does not slide. Also, we assume that R , the distance between the contact point to the center of mass, remains constant throughout the impact. In the case when no sliding occurs, the remaining mathematical condition will come from the equations for sticking [17], namely

$$\vec{V}^C \cdot \vec{i} = 0 \quad (2.25)$$

This means that the horizontal component of the contact point velocity equals to zero if sticking occurs during impact. Substituting Eqn. (2.3) into Eqn. (2.25) and

using dimensionless form gives

$$v'_x - \omega'_z R_y = 0 \quad (2.26)$$

The second and third possibilities occur when the magnitude of the frictional force cannot prevent sliding. This yields an impulse ratio which exceeds the coefficient of friction μ . In the rigid body analysis we need to consider both cases of the object initially sticking and then sliding or vice versa [6].

The case when the impacting body slides at the instant of impact and it continues to slide until the end of impact and doesn't change direction, is referred to as *sliding*. According to the Coulomb Law of friction, when sliding occurs the ratio of the impulsive forces will be governed by Eqn. (2.24) and the x direction of post impact contact point velocity ($v'_x - \omega'_z R_y$) is same as initial contact point velocity ($v_x - \omega_z R_y$). This required condition can be stated mathematically as

$$\mu = \left| \frac{\hat{F}'_x}{\hat{F}'_y} \right| \quad \frac{v'_x - \omega'_z R_y}{v_x - \omega_z R_y} > 0 \quad (2.27)$$

If sliding begins in one direction, then sliding stops and the impact point begins to slide in the reverse direction, we will refer to it as *reverse sliding*. The ratio of the impulsive forces will be also governed by Eqn. (2.24). However, the x direction of post impact contact point velocity ($v'_x - \omega'_z R_y$) will be opposite to the initial contact point velocity ($v_x - \omega_z R_y$). This required condition can be stated mathematically as

$$\mu = \left| \frac{\hat{F}'_x}{\hat{F}'_y} \right| \quad \frac{v'_x - \omega'_z R_y}{v_x - \omega_z R_y} < 0 \quad (2.28)$$

2.4.1 Analytical Expression for Coefficient of Friction

We still need to determine which set of equations should be used in any one of these three possibilities. The sliding and reverse sliding condition is given by Eqn. (2.24) and is based on the idea that sliding will commence if the force ratio exceeds the value of the coefficient of friction. We will use this idea to obtain a general expression for the coefficient of friction for sliding, $\mu_{Sliding}$, and reverse sliding, $\mu_{RSliding}$, in terms of the

initial impact parameters.

2.4.2 Critical Value for Sliding

The five dimensionless governing equations when object slides throughout both compression and restitution stages are Eqn. (2.10), (2.11), (2.12), (2.14) and (2.27). Putting them in matrix form results in

$$\begin{bmatrix} 1 & 0 & 0 & 1 & 0 \\ 0 & 1 & 0 & 0 & -1 \\ 0 & 0 & a & -R_y & -R_x \\ 0 & 1 & R_x & 0 & 0 \\ 0 & 0 & 0 & 1 & S\mu \end{bmatrix} \begin{bmatrix} v'_x \\ v'_y \\ w'_z \\ \hat{F}'_x \\ \hat{F}'_y \end{bmatrix} = \begin{bmatrix} p \\ 1 \\ a\lambda_z \\ -e_n(1 + \lambda_z R_x) \\ 0 \end{bmatrix} \quad (2.29)$$

where

$$S = -sgn(v_x - \omega_z R_y) \quad (2.30)$$

and sgn corresponds to the direction of velocity.

In matrix notation, Eqn. (2.29) can be expressed as

$$\begin{matrix} [A] \\ 5 \times 5 \end{matrix} \begin{matrix} [V'] \\ 5 \times 1 \end{matrix} = \begin{matrix} [V] \\ 5 \times 1 \end{matrix} \quad (2.31)$$

$[A]$ is the coefficient matrix in Eqn. (2.29) and $[V]$ and $[V']$ are the column matrices that contain the final and initial quantities, respectively. The solution can be expressed as

$$\begin{matrix} [V'] \\ 5 \times 1 \end{matrix} = \begin{matrix} [A]^{-1} \\ 5 \times 5 \end{matrix} \begin{matrix} [V] \\ 5 \times 1 \end{matrix} \quad (2.32)$$

Solving Eqn. (2.32) and simplifying, we get the final critical value of μ in sliding as

$$\mu_{Sliding} = \frac{(-R_x R_y + R_y a \lambda - e_n R_y R_x - R_y e_n \lambda R_x^2 - p a - p R_x^2)}{sgn(-v_{cx})(a + R_x a \lambda + a e_n + a e_n \lambda R_x + R_y^2 + e_n R_y^2 + e_n R_y^2 \lambda R_x + p R_x R_y)} \quad (2.33)$$

where $S = sgn(\gamma)$ is determined by the sliding direction.

2.4.3 Critical Value for Reverse Sliding

The five dimensionless governing equations are (2.10), (2.11), (2.12), (2.14) and (2.28).

Putting them in matrix form results in

$$\begin{bmatrix} 1 & 0 & 0 & 1 & 0 \\ 0 & 1 & 0 & 0 & -1 \\ 0 & 0 & a & -R_y & -R_x \\ 0 & 1 & R_x & 0 & 0 \\ 0 & 0 & 0 & 1 & -S\mu \end{bmatrix} \begin{bmatrix} v'_x \\ v'_y \\ w'_z \\ \hat{F}'_x \\ \hat{F}'_y \end{bmatrix} = \begin{bmatrix} p \\ 1 \\ a\lambda_z \\ -e_n(1 + \lambda_z R_x) \\ 0 \end{bmatrix} \quad (2.34)$$

Solving the inverse matrix for the sliding mode, and simplifying, we get the final critical value of μ in reverse sliding condition. Hence,

$$\mu_{RSliding} = \frac{R_y a \lambda - a p - R_y R_x^2 e_n \lambda - R_x^2 p - R_y R_x e_n - R_y R_x}{S \cdot (a e_n \lambda R_x + a e_n + a + a \lambda R_x + R_y^2 + e_n R_y^2 + p R_y R_x + e_n \lambda R_x R_y^2)} \quad (2.35)$$

where $S = Sgn(\gamma)$, it determines which direction the object is sliding from.

2.4.4 Transition in Reverse Sliding and Sticking Mode

Due to the Coulomb's law which states that the magnitude of the frictional force can be related to the magnitude of the normal force via a coefficient and its direction is always opposite to the relative tangential motion. If tangential velocity v_{cx} changes to the opposite direction, friction force \hat{F}_x will also change direction when sliding turns into reverse sliding. As a result, there is a transitional sticking mode that sliding will come to an end when the condition $v_{cx} = v_x - \lambda R_y = 0$ is satisfied. During this transition, the

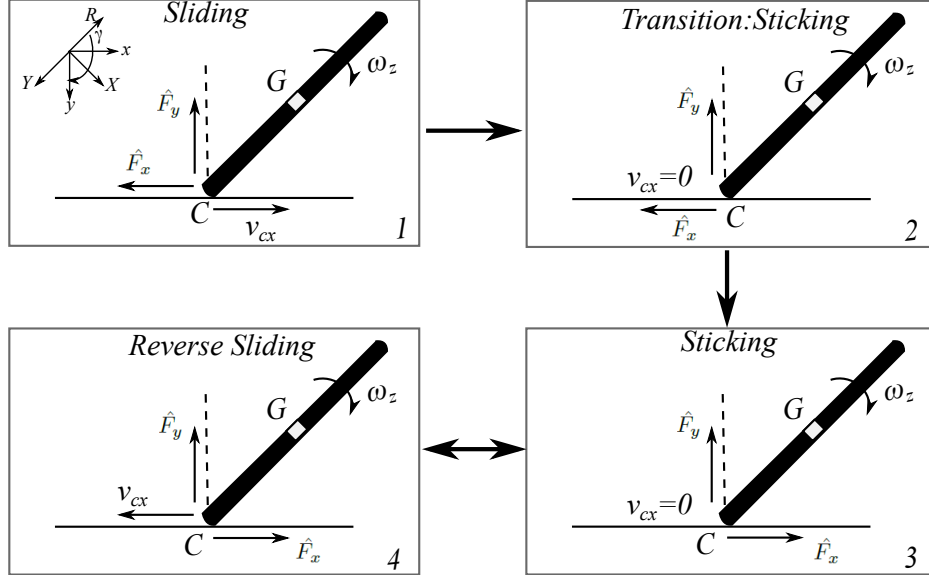


Figure 2.2: Special case in reverse sliding

friction force \hat{F}_x changes directions. Moreover, if the condition $\hat{F}_x > -\text{sgn}(v_{cx})\mu\hat{F}_y$ is satisfied, the object begins reverse sliding. This procedure is described in Figure (2.2).

In the first phase, 1, the rod begins sliding along x^+ direction during compression, and the relative contact point tangential velocity v_{cx} is not zero. In the second phase 2, as v_{cx} becomes zero, the rod sticks to the ground. In the third phase 3, as a result of angular impulse-momentum effect, a tendency for the rod to slide in the x^- direction changes the friction force \hat{F}_x to x^+ direction. In phase 4, if the condition $\hat{F}_x > -\text{sgn}(v_{cx})\mu\hat{F}_y$ is satisfied, the rod begins to slide along x^- direction. Otherwise, the rod stays in sticking in phase 3.

2.4.5 Coefficient of Static and Kinetic Friction

In making a distinction between static and kinetic coefficients of friction, we are dealing with an aspect of "real world" common experience with a phenomenon. The difference between static μ_s and kinetic coefficients μ_k is obtained in simple experiments, such as wooden blocks sliding on wooden inclines. This difference may arise from irregularities, surface contaminants, etc. which is hard to quantify. When such experiments are carried out with smooth metal blocks that are carefully cleaned, the difference between static and kinetic coefficients tends to disappear. When coefficients of friction for specific

Orientation Angle γ	Coefficient of Friction μ	Modes
$\frac{\pi}{2} \leq \gamma \leq \pi$	$\mu \leq \mu_{Sliding}$	Sliding
$\frac{\pi}{2} \leq \gamma \leq \pi$	$\mu > \mu_{Sliding}$	Sticking
$\pi \leq \gamma \leq \frac{3\pi}{2}$	$\mu_{Sliding} \leq \mu \leq \mu_{RSliding}$	Reverse Sliding
$\pi \leq \gamma \leq \frac{3\pi}{2}$	$\mu > \mu_{RSliding}$	Sticking
$\pi \leq \gamma \leq \frac{3\pi}{2}$	$\mu \leq \mu_{Sliding}$	Sliding

Table 2.1: Conditions on different modes

surface combinations are quoted, it is the kinetic coefficient which is generally quoted since it is the more reliable number.

To determine whether we should use both static and kinetic coefficients or only kinetic coefficient, we will do a few comparison tests in the following chapters including simulations and experiments. Generally the maximum static friction is greater than dynamic (kinetic) friction, or

$$\mu_s > \mu_k \quad (2.36)$$

2.4.6 Summary

If initial conditions and parameters $a, \gamma, e_n, p, R, \lambda$ are given, we can determine different possibilities, named as *modes*, by comparing the value μ to $\mu_{Sliding}$ and $\mu_{RSliding}$ using Eqn (2.33) and (2.35). For example, when the coefficient of friction μ is larger than $\mu_{Sliding}$, the result will be sticking mode. Table (2.1) shows the conditions on different modes.

2.5 Cases of Impact

As we discuss in the literature review, impact takes place in two stages: compression and restitution. To avoid confusion with notation, Figure (2.3) shows how the notation of quantities change during impact. The superscript $()^c$ denotes compression stage and $()^r$ denotes restitution stage. The superscript $()'$ denotes post-impact quantities and subscript $()_c$ denotes quantities at contact point. The following quantities are used in the thesis:

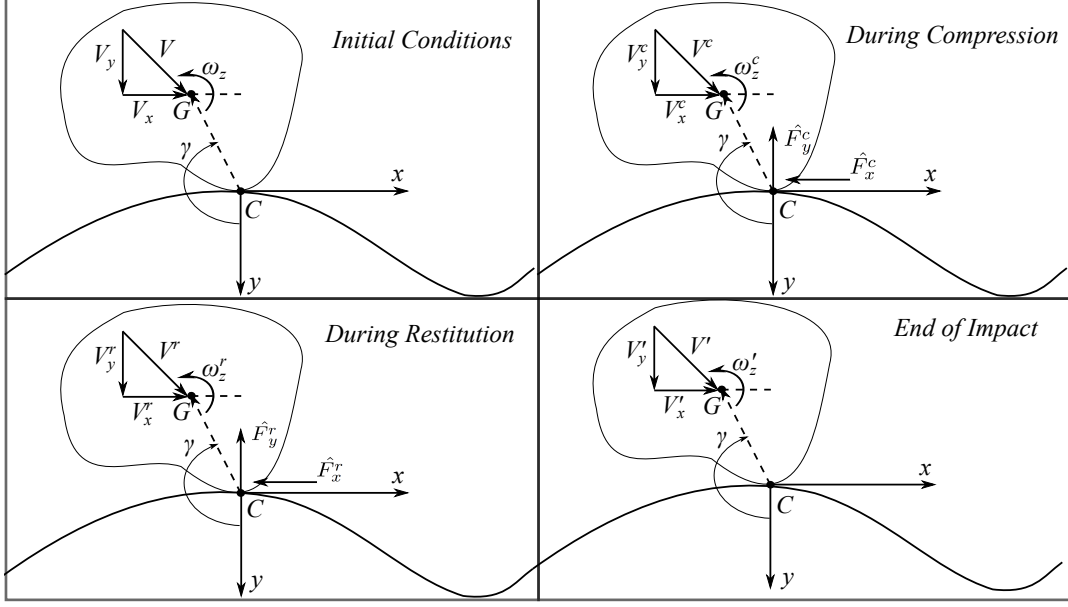


Figure 2.3: Notation for different stages

- Initial condition v_x, v_y, w_z, F_x, F_y .
- During compression, $v_x^c, v_y^c, w_z^c, F_x^c, F_y^c$.
- During restitution, $v_x^r, v_y^r, w_z^r, F_x^r, F_y^r$.
- Post-impact, $v_x', v_y', w_z', F_x', F_y'$.

In addition, one of these impact possibilities (sliding, sticking and reverse sliding) can occur at any stage. Therefore, it is necessary to split the study of impact into two stages, compression and restitution, and analyze the governing equation in each stage separately.

Case 0: Object starts from sliding and continues to slide throughout the compression and restitution stages.

End of compression condition:

$$\hat{F}_x = -\text{sgn}(v_{cx})\mu\hat{F}_y \quad (2.37)$$

$$v_{cy}^c = v_y^c + \lambda^c R_x = 0 \quad (2.38)$$

End of restitution condition:

$$\hat{F}_x = -\text{sgn}(v_{cx})\mu\hat{F}_y \quad (2.39)$$

$$e_n = -\frac{v'_y + \omega'_z R_x}{1 + \lambda_z R_x} \quad (2.40)$$

Case 1: *Object slides at the beginning of impact and stops sliding, or sticks, during compression. It then remains sticking in the restitution stage.*

End of compression condition:

$$v_{cx}^c = v_x^c - \lambda^c R_y = 0 \quad (2.41)$$

$$v_{cy}^c = v_y^c + \lambda^c R_x = 0 \quad (2.42)$$

End of restitution condition:

$$v_{cx}^r = v_x^r - \lambda^r R_y = 0 \quad (2.43)$$

$$e_n = -\frac{v'_y + \omega'_z R_x}{1 + \lambda_z R_x} \quad (2.44)$$

Case 2: *Object slides at the beginning of impact. It ends sliding and begins reverse sliding during compression. It continues in reverse sliding during restitution.*

End of compression condition:

$$\text{sgn}(v_{cx}) = -\text{sgn}(v_{cx}^c) \quad (2.45)$$

$$\hat{F}_x = -\text{sgn}(v_{cx}^c)\mu\hat{F}_y \quad (2.46)$$

$$v_{cy}^c = v_y^c + \lambda^c R_x = 0 \quad (2.47)$$

End of restitution condition:

$$\text{sgn}(v_{cx}) = -\text{sgn}(v_{cx}^r) \quad (2.48)$$

$$\hat{F}_x = -\text{sgn}(v_{cx}^r)\mu\hat{F}_y \quad (2.49)$$

$$e_n = -\frac{v_y' + \omega_z' R_x}{1 + \lambda_z R_x} \quad (2.50)$$

Case 3: Object remains sliding during the compression stage. However, it stops sliding and changes to sticking in the restitution stage.

End of compression condition:

$$\hat{F}_x = -\text{sgn}(v_{cx})\mu\hat{F}_y \quad (2.51)$$

$$v_{cy}^c = v_y^c + \lambda^c R_x = 0 \quad (2.52)$$

End of restitution condition:

$$v_{cx}^r = v_x^r - \lambda^r R_y = 0 \quad (2.53)$$

$$e_n = -\frac{v_y' + \omega_z' R_x}{1 + \lambda_z R_x} \quad (2.54)$$

Case 4: Object continues sliding during the compression stage. However, it stops sliding and changes to reverse sliding during restitution.

End of compression condition:

$$\hat{F}_x = -\text{sgn}(v_{cx})\mu\hat{F}_y \quad (2.55)$$

$$v_{cy}^c = v_y^c + \lambda^c R_x = 0 \quad (2.56)$$

End of restitution condition:

$$\text{sgn}(v_{cx}) = -\text{sgn}(v_{cx}^r) \quad (2.57)$$

$$\hat{F}_x = -\text{sgn}(v_{cx}^r)\mu\hat{F}_y \quad (2.58)$$

$$e_n = -\frac{v_y' + \omega_z' R_x}{1 + \lambda_z R_x} \quad (2.59)$$

Case 5: Object starts from free fall position (no horizontal velocity of impact point), which initial contact point velocity equals zero, and remains sticking throughout both stages.

End of compression condition:

$$v_{cx}^c = v_x^c - \lambda^c R_y = 0 \quad (2.60)$$

$$v_{cy}^c = v_y^c + \lambda^c R_x = 0 \quad (2.61)$$

End of restitution condition:

$$v_{cx}^r = v_x^r - \lambda^r R_y = 0 \quad (2.62)$$

$$e_n = -\frac{v_y' + \omega_z' R_x}{1 + \lambda_z R_x} \quad (2.63)$$

Case 6: Object starts from free fall position, but it changes to reverse sliding during

compression and continues in reverse sliding during the restitution stage.

End of compression condition:

$$\text{sgn}(v_{cx}) = -\text{sgn}(v_{cx}^c) \quad (2.64)$$

$$\hat{F}_x = -\text{sgn}(v_{cx}^c)\mu\hat{F}_y \quad (2.65)$$

$$v_{cy}^c = v_y^c + \lambda^c R_x = 0 \quad (2.66)$$

End of restitution condition:

$$\text{sgn}(v_{cx}) = -\text{sgn}(v_{cx}^r) \quad (2.67)$$

$$\hat{F}_x = -\text{sgn}(v_{cx}^r)\mu\hat{F}_y \quad (2.68)$$

$$e_n = -\frac{v_y' + \omega_z' R_x}{1 + \lambda_z R_x} \quad (2.69)$$







Case #	Color Code	Initial Condition	Compression Stage	Restitution Stage
0		$v_{cx} \neq 0$	Sliding	Sliding
1		$v_{cx} \neq 0$	Sliding ends, Sticking begins	Sticking
2		$v_{cx} \neq 0$	Sliding ends, Reverse Sliding begins	Reverse Sliding
3		$v_{cx} \neq 0$	Sliding	Sliding ends, Sticking begins
4		$v_{cx} \neq 0$	Sliding	Sliding ends, Reverse Sliding begins
5		$v_{cx} = 0$	Sticking	Sticking
6		$v_{cx} = 0$	Sticking ends, Reverse Sliding begins	Reverse Sliding

Table 2.2: Cases for two-dimensional impact

We notice that once the object changes from one mode to another mode, there is no other impulsive force which can change the modes back to original mode again. Thus combining all these scenarios listed above, seven different cases can be identified. These cases are summarized in Table (2.2). Figures (2.4) and (2.5) are flow charts for analysis of what happen during impact and for numerical computation that expands Table (2.2). Note that, the last two cases only take place when the horizontal velocity of the contact point C is zero as initial condition. In subsection 1.8.1, the seven cases variation with initial parameters γ , which denotes the inclination angle, and p , which denotes the initial velocity, are shown in figure (2.7).

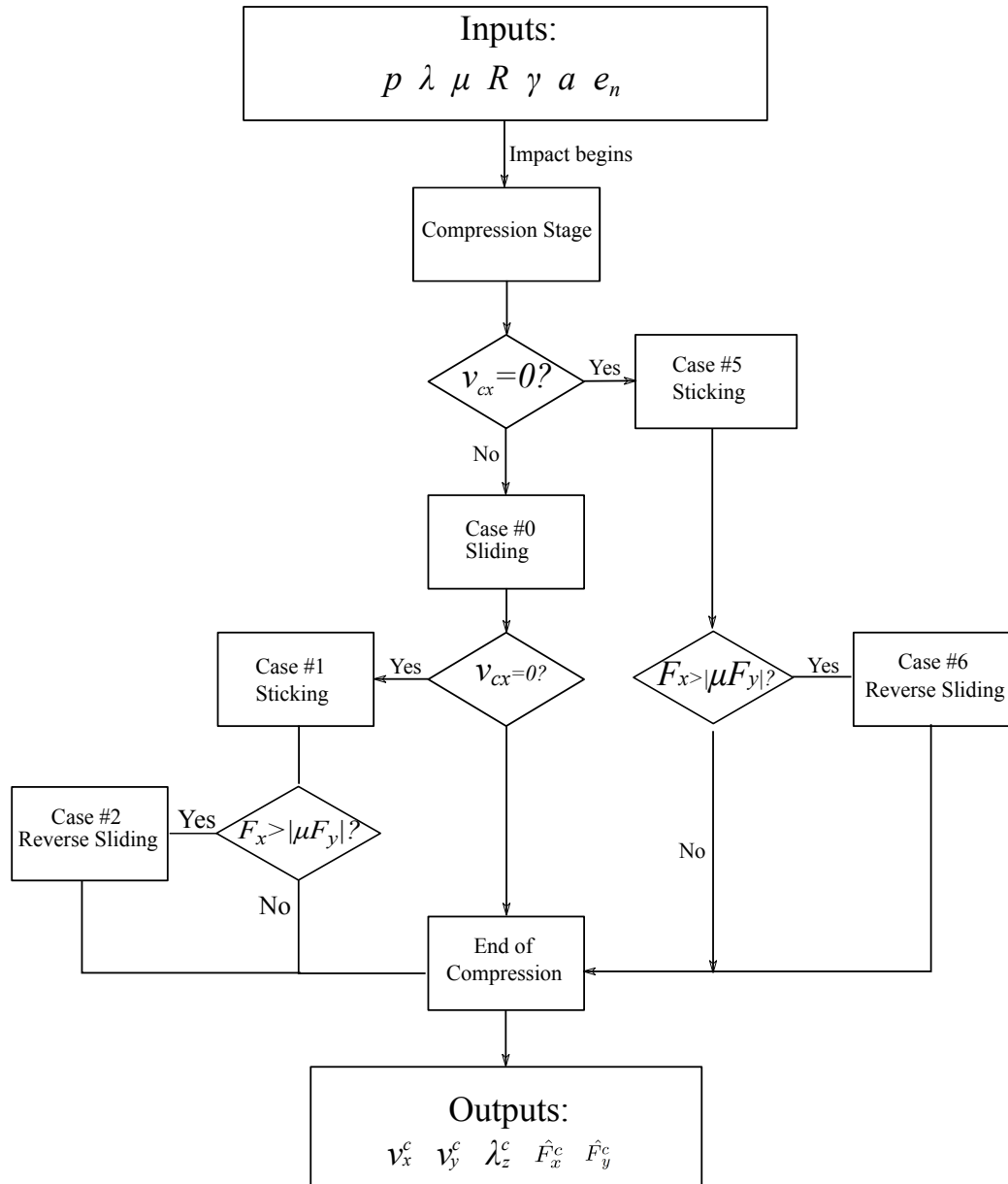


Figure 2.4: Flow chart for compression impulse computation

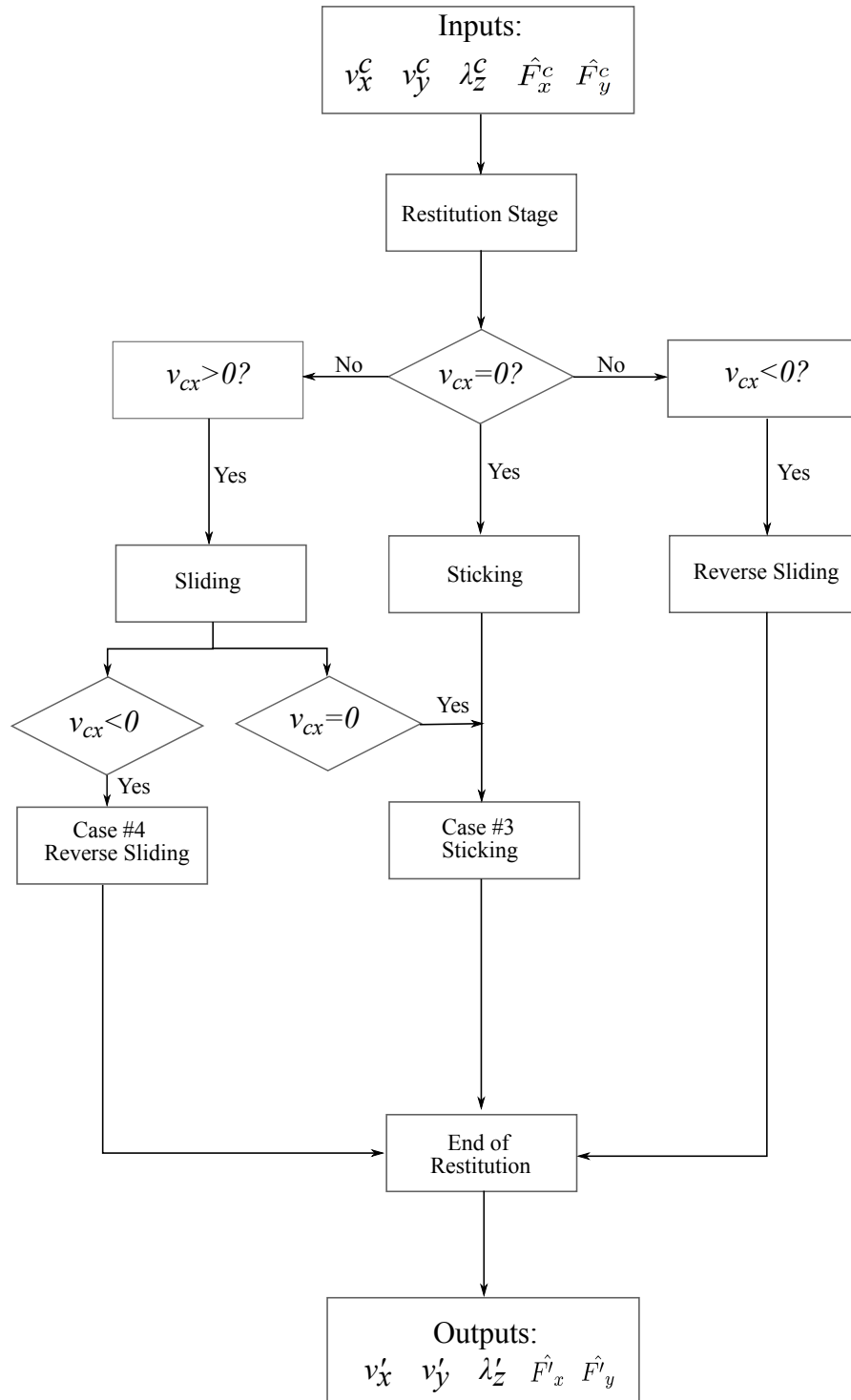


Figure 2.5: Flow chart for restitution impulse computation

2.6 Summary of the Procedure

A summary of the steps for the planar frictional impact analysis of contact problem is presented here. If the pre-impact quantities, coefficient of restitution e_n and dynamic friction coefficient μ are given and assuming $\mu = \mu_s = \mu_k$, the impact can be analyzed by using the following procedure. The entire impact process is divided into two stages: Compression and Restitution. In most of the cases, we assume the object is sliding at the beginning of the compression stage.

1. During the compression stage, evaluate the generalized impact velocities $(v_x^{c1}, v_y^{c1}, \lambda^{c1})$ and the impulsive forces $(\hat{F}_x^{c1}, \hat{F}_y^{c1})$ from Eqn. (2.10,2.11,2.12), sliding condition Eqn. (2.37) and end of compression condition Eqn. (2.38).

$$\hat{F}_x = -sgn(v_{cx})\mu\hat{F}_y \quad (2.70)$$

$$v_y^{c1} + \lambda^{c1}R_x = 0 \quad (2.71)$$

$$v_{cx}^{c1} = v_x^{c1} - \lambda^{c1}R_y > 0 \quad (2.72)$$

$$\hat{F}_x^{c1} = -sgn(v_{cx})\mu\hat{F}_y^{c1} \quad (2.73)$$

$$v_{cx}^{c2} = v_x^{c2} - \lambda^{c2}R_y = 0 \quad (2.74)$$

2. Check for whether sliding ends in compression stage from Eqn. (2.72). If not, switch the sliding condition Eqn. (2.73) to sticking condition Eqn. (2.74) and evaluate the generalized impact quantities $(v_x^{c2}, v_y^{c2}, \lambda^{c2}, \hat{F}_x^{c2}, \hat{F}_y^{c2})$.

$$\hat{F}_x^{c2} \leq abs(\mu\hat{F}_y^{c2}) \quad (2.75)$$

$$\hat{F}_x^{c2} = -sgn(\gamma)\mu\hat{F}_y^{c2} \quad (2.76)$$

3. Check for whether sliding turns into reverse sliding during compression by Eqn. (2.75). If not, replace the sticking condition Eqn. (2.74) with reverse sliding condition Eqn. (2.76) and evaluate the generalized impact quantities $(v_x^c, v_y^c, \lambda^c, \hat{F}_x^c, \hat{F}_y^c)$.

4. During the restitution stage, repeat steps 1 to 3, evaluate the impact velocities $(v_x^r, v_y^r, \lambda^r)$ and the impulsive forces $(\hat{F}_x^r, \hat{F}_y^r)$. The only difference between compression and restitution stages is end of compression condition Eqn. (2.71) changes to Eqn. (2.14,2.15,4.41) based on different coefficient of restitution models.
5. Based on step 1 to 4 above, determine the case of impact from Table (2.2). In general, we get $(v_x^c, v_y^c, \lambda^c, \hat{F}_x^c, \hat{F}_y^c)$ at the end of compression stage and $(v_x^r, v_y^r, \lambda^r, \hat{F}_x^r, \hat{F}_y^r)$ at the end of compression stage.

$$v'_x = v_x^r \quad v'_y = v_y^r \quad \lambda' = \lambda^r \quad (2.77)$$

$$\hat{F}'_x = \hat{F}_x^c + \hat{F}_x^r \quad (2.78)$$

$$\hat{F}'_y = \hat{F}_y^c + \hat{F}_y^r \quad (2.79)$$

According to Eqn. (2.77,2.78,2.79), the post-impact velocities are v'_x, v'_y, λ' and the impulsive forces are \hat{F}'_x and \hat{F}'_y .

2.7 Energy Dissipation

An important indicator of the damage to the object that makes impact is the energy which it absorbs. It is desirable to develop a relationship for the energy loss during impact for both the sliding sticking and reverse sliding cases. These expressions can then be used to determine the initial parameters that will yield the smallest energy loss. Typically, a smaller energy loss during impact corresponds to the object absorbing less energy, which is favorable. The initial and final kinetic energies of the object can be expressed as follows:

$$K_{initial} = \frac{1}{2}m(v_x^2 + v_y^2) + \frac{1}{2}I_G\omega_z^2 \quad (2.80)$$

$$K_{final} = \frac{1}{2}m(v_x'^2 + v_y'^2) + \frac{1}{2}I_G\omega_z'^2 \quad (2.81)$$

The difference in potential energy immediately before and after impact is assumed

to be negligible. The energy lost during impact can be stated as:

$$K_{loss} = \left(\frac{1}{2}m(v_x^2 + v_y^2) + \frac{1}{2}I_G\omega_z^2 \right) - \left(\frac{1}{2}m(v_x'^2 + v_y'^2) + \frac{1}{2}I_G\omega_z'^2 \right) \quad (2.82)$$

We can nondimensionalize Eqn. (2.82) with respect to the initial kinetic energy. Hence,

$$K_{dissipation} = 1 - \frac{v_x'^2 + v_y'^2 + a\lambda_z'^2}{p^2 + 1 + a\lambda_z^2} \quad (2.83)$$

2.8 Analysis of a Point-to-Line Impact Process-Impact of a Falling Rod with the Ground

In rigid body mechanics impact is treated as instantaneous. As a result, we assume that during the small time interval the positions and angle orientations of all bodies remain unchanged, since all velocities remain finite. Here we develop an analytical expression on how to determine modes changed based on initial conditions for a general point-to-line collision with friction.

A rod of unit mass and unit length, falling with a unit normal velocity before impact is shown in Figure (2.6). Running a single impact simulation according to the summary of the procedure in section 2.6, we obtain the post-impact dynamic quantities with initial inputs. A list of the parameters used and calculated is shown in Table (3.2). The angle between the horizontal and impact surface is θ . If the rod is perpendicular to the horizontal before impact, θ equals to the orientation angle $\pi - \gamma$. We shall now graphically ascertain the behavior of the energy loss functions in different cases as we vary the initial parameters including the orientation angle γ and the initial velocity ratio p .

2.8.1 Case Study

We first examine the seven cases in Figure (2.7). This figure shows how the different cases of impact change while varying orientation angle γ and initial velocity ratio p . Different

Initial Parameters	$p, \lambda, \mu, R, \gamma, a, e_n$
Parameters in Compression	$v_x^c, v_y^c, \lambda^c, \hat{F}_x^c, \hat{F}_y^c$
Parameters in Restitution	$v_x^r, v_y^r, \lambda^r, \hat{F}_x^r, \hat{F}_y^r$
Post-impact Dynamic Quantities	$v_x', v_y', \lambda', \hat{F}_x', \hat{F}_y'$

Table 2.3: Parameters used in a single impact simulation

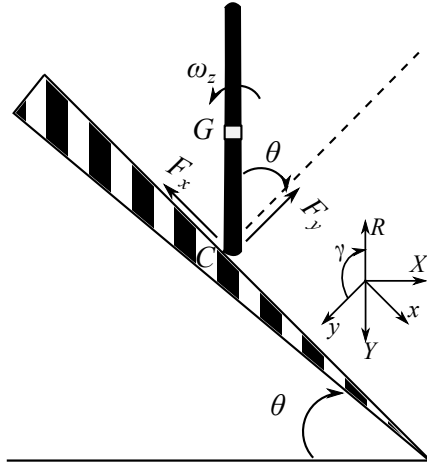


Figure 2.6: Falling rod colliding with ground

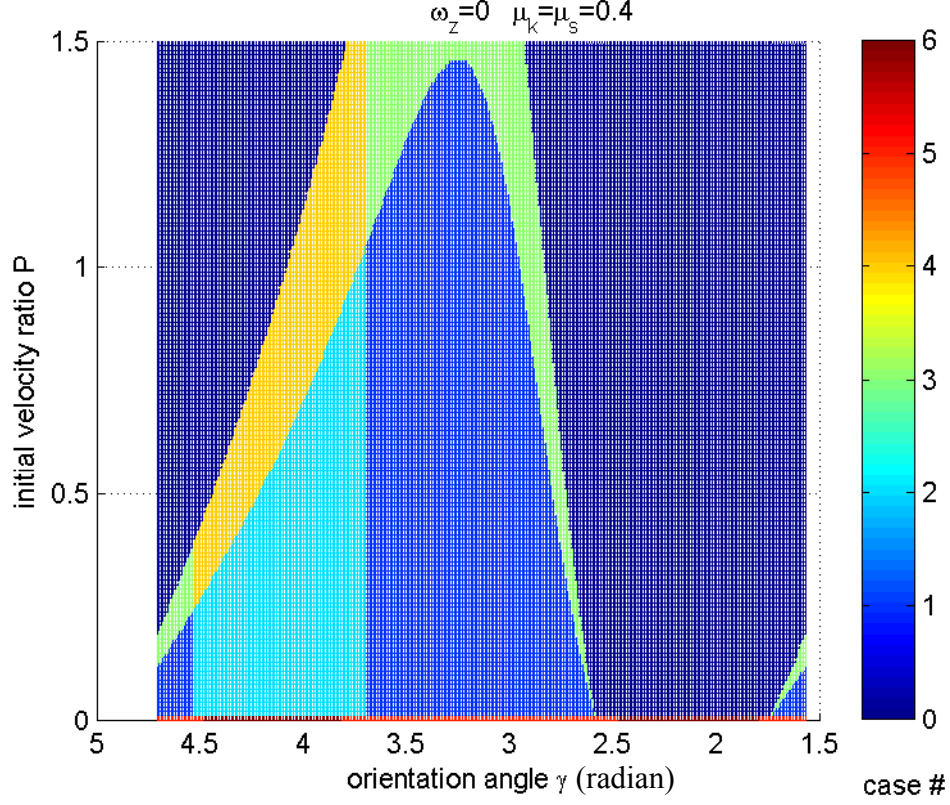


Figure 2.7: Seven cases variation with initial parameters γ and p

colors represent different cases described in Table (2.2). For example, color code 0 is sliding and color code 1 represents sticking and color code 2 represents reverse sliding. Note that both initial parameters γ and p affect the modes of sliding. For example, as we change the orientation angle γ from π to $\frac{3\pi}{2}$, same configuration as Figure (2.6), the mode changes from sticking to reverse sliding. As decreasing orientation angle γ from π to $\frac{\pi}{2}$, the mode changes from sticking to sliding and then finally goes back to sticking because the rod is almost parallel to the ground. Also increasing the initial velocity ratio p , which means increasing horizontal velocity v_x , will result in changing mode from sticking or reverse sliding into sliding.

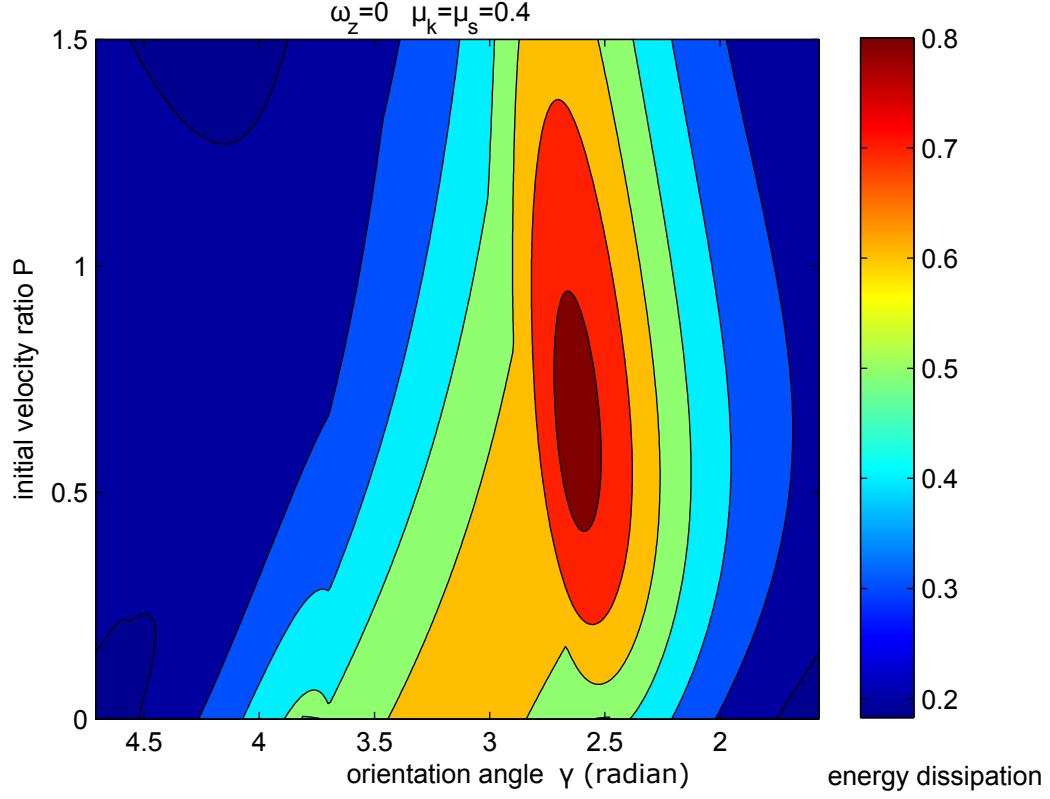


Figure 2.8: Influence of initial parameters γ and p on the energy loss contour

2.8.2 Energy Dissipation Study

We next investigate the energy lost in different regimes according to the initial parameters and different cases. Figure (2.8) indicates that the minimum energy dissipation occurs in the regime orientation angle γ ranging from 1.5 to 1.7 and 4.5 to 4.7 rad/s, with initial velocity ratio p ranging from 0 to 0.25. From Table (2.2), this region belongs to the sticking mode. Lower energy dissipation in the sticking mode rather than sliding mode proves that friction force doesn't do work during sticking. On the other hand, the maximum energy dissipation occurs in the region where orientation angle γ ranging from 2.5 to 2.7 rad/s and initial velocity ratio p ranging from 0.4 to 0.8. This region belongs to the sliding mode. We can conclude that energy loss becomes larger as the object changes from sticking to sliding or to reverse sliding. Impulsive friction forces do work only through sliding or reverse sliding.

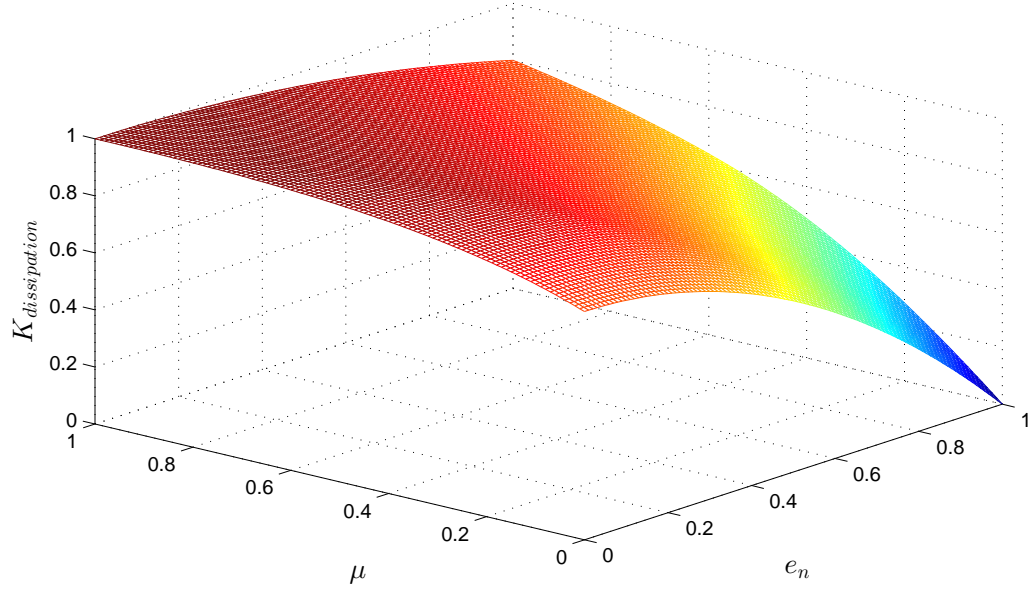


Figure 2.9: Influence of e_n and μ on the energy loss with $\gamma = \frac{5\pi}{4}$; reverse sliding; axisymmetric body

2.8.3 Special Values of μ and e_n on the Energy Loss

It is known that there is no energy loss when $\mu = 0$ and $e_n = 0$. In contrast, the most energy dissipation occurs when $\mu = 1$ and $e_n = 1$. These phenomena can be observed in Figures (2.9) and (2.10). Also, in reverse sliding mode, e_n has a larger influence on energy loss than μ . On the other hand, in sliding mode, μ effects energy loss more than e_n does.

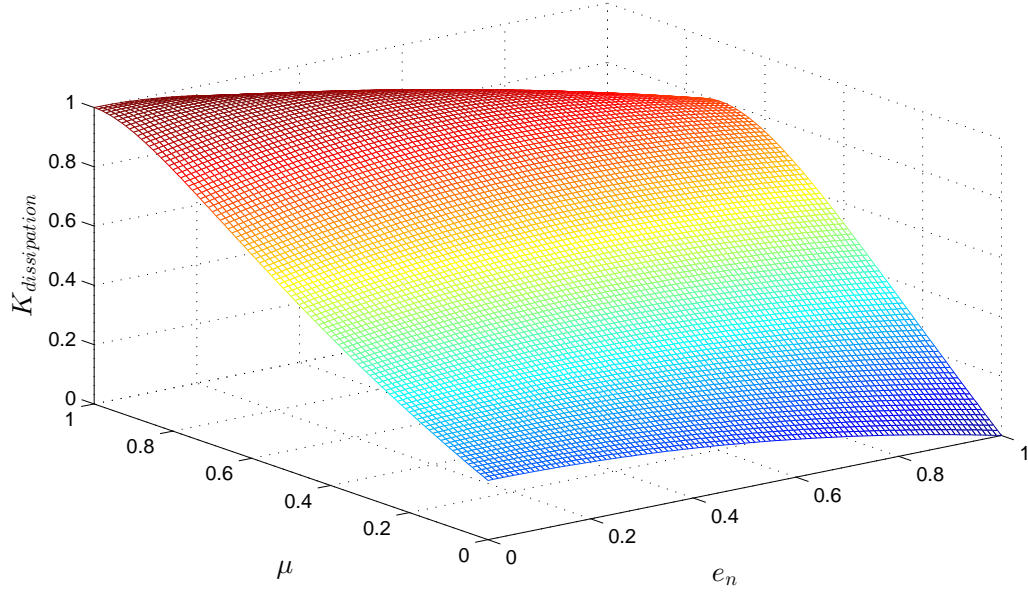


Figure 2.10: Influence of e_n and μ on the energy loss with $\gamma = \frac{3\pi}{4}$; sliding; axisymmetric body

2.8.4 Comparison for Different Friction Coefficient Models (μ_k and μ_s)

As mentioned earlier, instead of using only kinetic coefficient of friction μ_k , static coefficient of friction μ_s can be another important factor affecting impact. Consider the case when μ_k changes to μ_s . This occurs while the object is in the transition sticking mode while turning from sliding to reverse sliding, or from initially sticking to reverse sliding mode, we investigate the cases and energy dissipation comparison.

Cases Comparison

Figure (2.11) shows the variation of cases while we using different Coefficient of Friction Models (μ_k and μ_s) based on same initial condition γ and p . The μ_k model is on left hand side and μ_s model is on right hand side. From the comparison, sliding region remains the same in both models but sticking region is larger in μ_s model than μ_k model while sticking region is smaller in μ_s model than μ_k model. This is due to the fact that static friction coefficient μ_s is larger than μ_k which makes it more difficult to

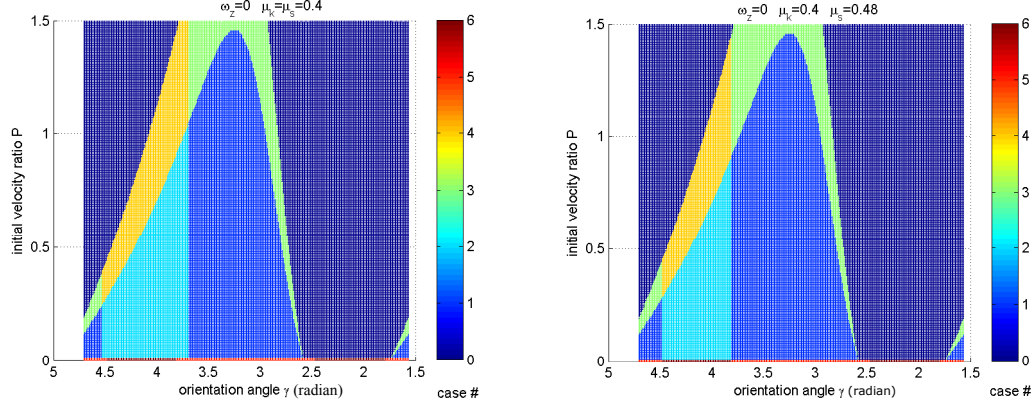


Figure 2.11: Influence of initial parameters γ and p on cases contour with $\omega_z = 0$, $\mu_k = 0.4, \mu_s = 0.48$; with μ_s and μ_k models

change object into reverse sliding.

Energy Dissipation Comparison

Figure (2.12) shows the variation of energy loss while we using different coefficient of friction models (μ_k and μ_s) based on same initial condition γ and p . The μ_k model is on left hand side and μ_s model is on right hand side. From the comparison, sliding region still remains the same in both models. There is a discontinuity of energy loss in μ_s model. This region belongs to the transition that sliding turns into reverse sliding. We conclude that velocity in this transition is discontinuous, as well. To investigate this phenomenon and figure out which model has a better approximation of 'real world' behavior, we will conduct experiments when we discuss 3D impact in the next section and more details can be revealed in Chapter 4.

2.8.5 Discussion on choosing e_n among Newton's, Poisson's and Stronge's hypothesis

Three COR hypotheses have been introduced in the previous section. To choose the one that best fits our model, we examine the energy dissipation in extremely rare cases, in which $e_n = 1$ and $\mu = 0$. Figures (2.13,2.14,2.15) show that how the energy dissipation varies while the friction coefficient μ changes from 0 to 1. In the extreme case $e_n = 1$, we notice that Newton's and Poisson's hypotheses will lead to negative energy dissipation.

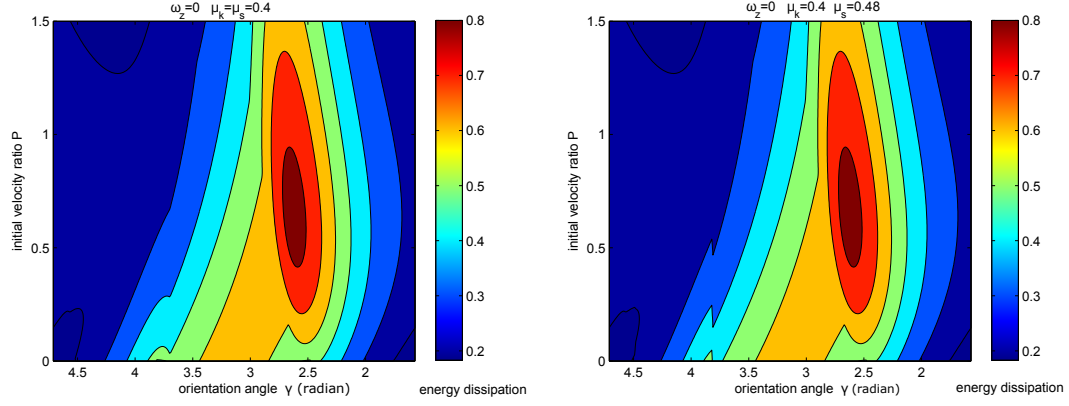


Figure 2.12: Influence of initial parameters γ and p on the energy loss contour with $\omega_z = 0$, $\mu_k = 0.4, \mu_s = 0.48$; with μ_s and μ_k models

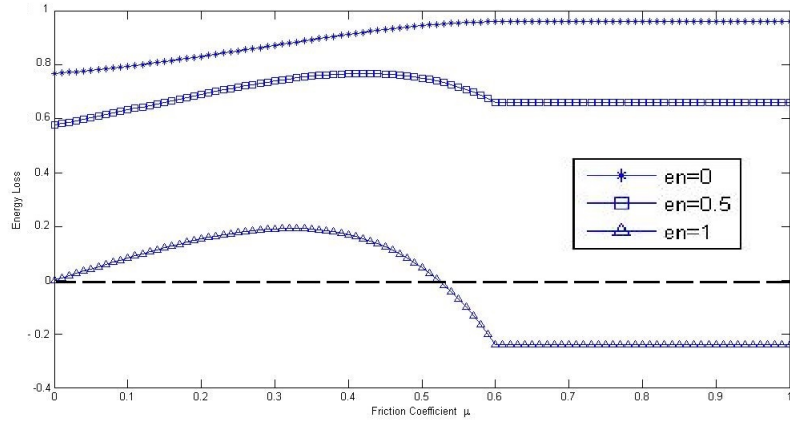


Figure 2.13: Newton's COR hypothesis

In other word, Newtonian and Poisson's approaches can result in an increase of energy in some configurations of a perfectly elastic impact. It shows that Stronge's hypothesis of restitution is the better of three theories.

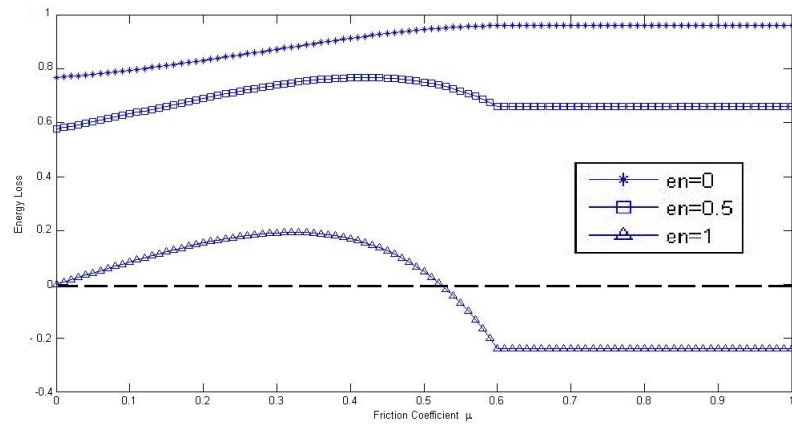


Figure 2.14: Poisson's COR hypothesis

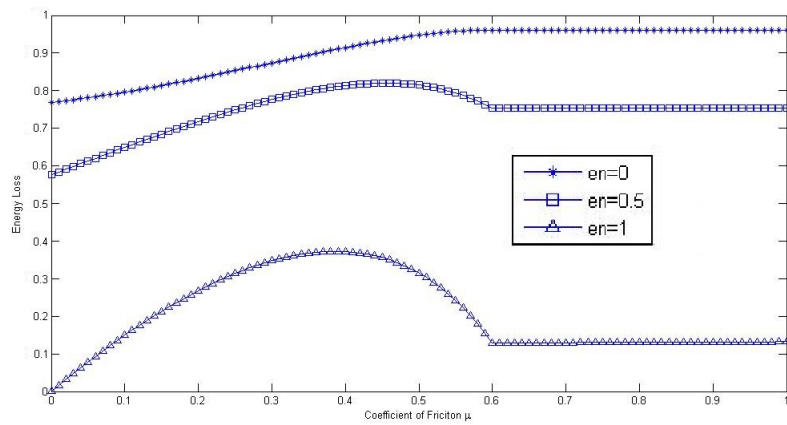


Figure 2.15: Stronge's COR hypothesis

2.9 Experimental Validation

In this section, we validate the use of the numerical impact model by comparing it to experimental results. The model is applied in a manner that requires the input of the coefficient of restitution, which is determined through experiments. The quantitative comparison is the energy dissipation percentage, which is defined as the ratio of the initial and final kinetic energies.

We conduct an experiment, shown schematically in Figure (2.16), for validation of the impact analysis with friction. The motion of the system is recorded using high speed video camera, capable of 120 frames per second with resolution 800×450 pixels. The elapsed time and the displacements of all vertex points of moving bodies between those frames can be obtained. Thus, the pre-impact and the post-impact velocities and angular velocities can be calculated using the data. More details on experimental setup will be discussed in chapter 4, when we describe 3D experiment.

The experimental set-up, as shown in Figure (2.17), includes the following main components:

1. Moving object: A rod in Figure (2.18) is painted black to obtain contrast during image processing. Three reflective tape markers, one at the center and the other two located at the top and bottom of rod, are used to capture the kinematic data.

2. The dropping device: The dropping device is designed to meet the requirement that the pre-collision velocities and orientations of the rod should be independently adjustable while maintaining the same impact point. Two adjustments are incorporated:

- i) the initial tangential and vertical velocity of the center of mass of the rod v_x and v_y .

- ii) the orientation angle of the contact surface $\theta = \pi - \gamma$.

3. The data acquisition system: A high speed camera (Samsung S4 with a maximum capture rate of 120 frames/sec) is used to acquire the kinematic data. Video images of each experiment are transferred to the computer and the the center locations of the three markers on the rod are computed. The position data is then used to calculate the inclination angle of the rod at the instant of collision and pre and post impact velocities.

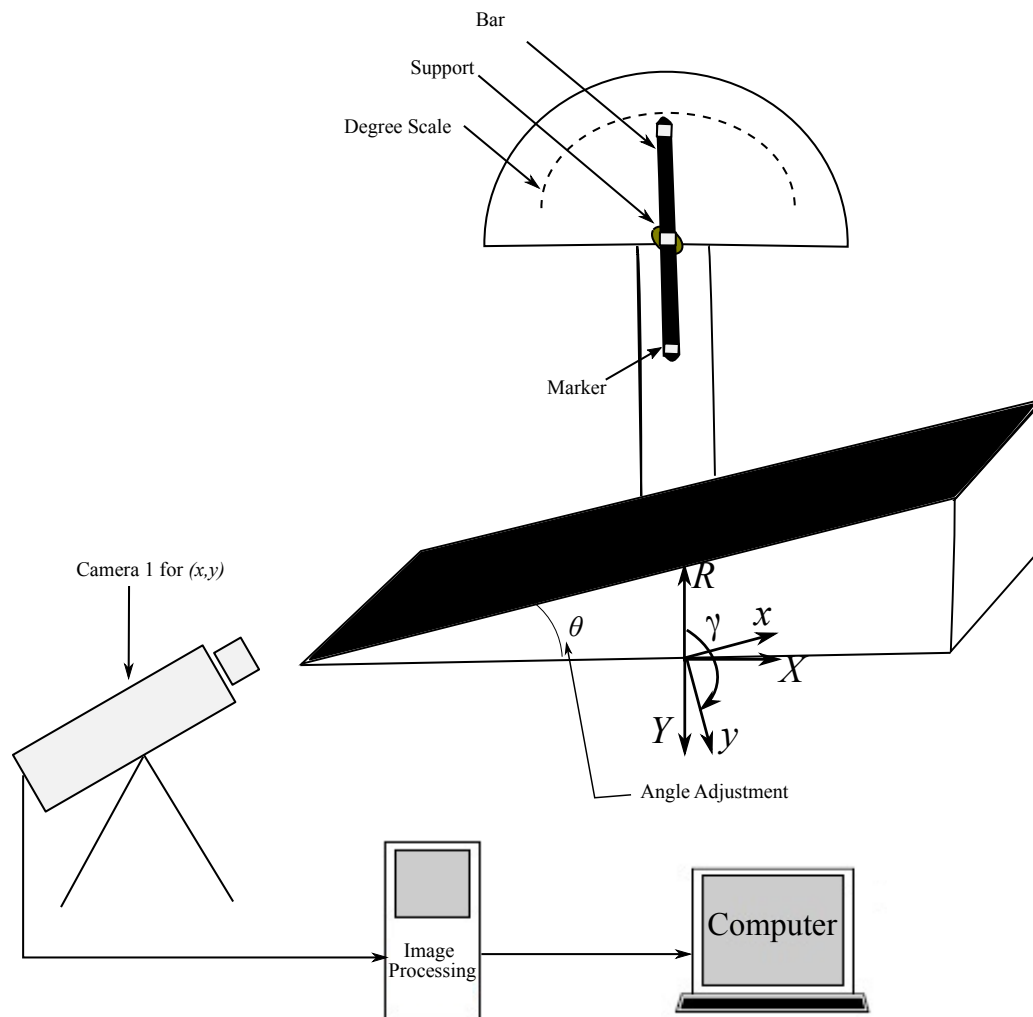


Figure 2.16: Schematic diagram of 2D Experiment platform

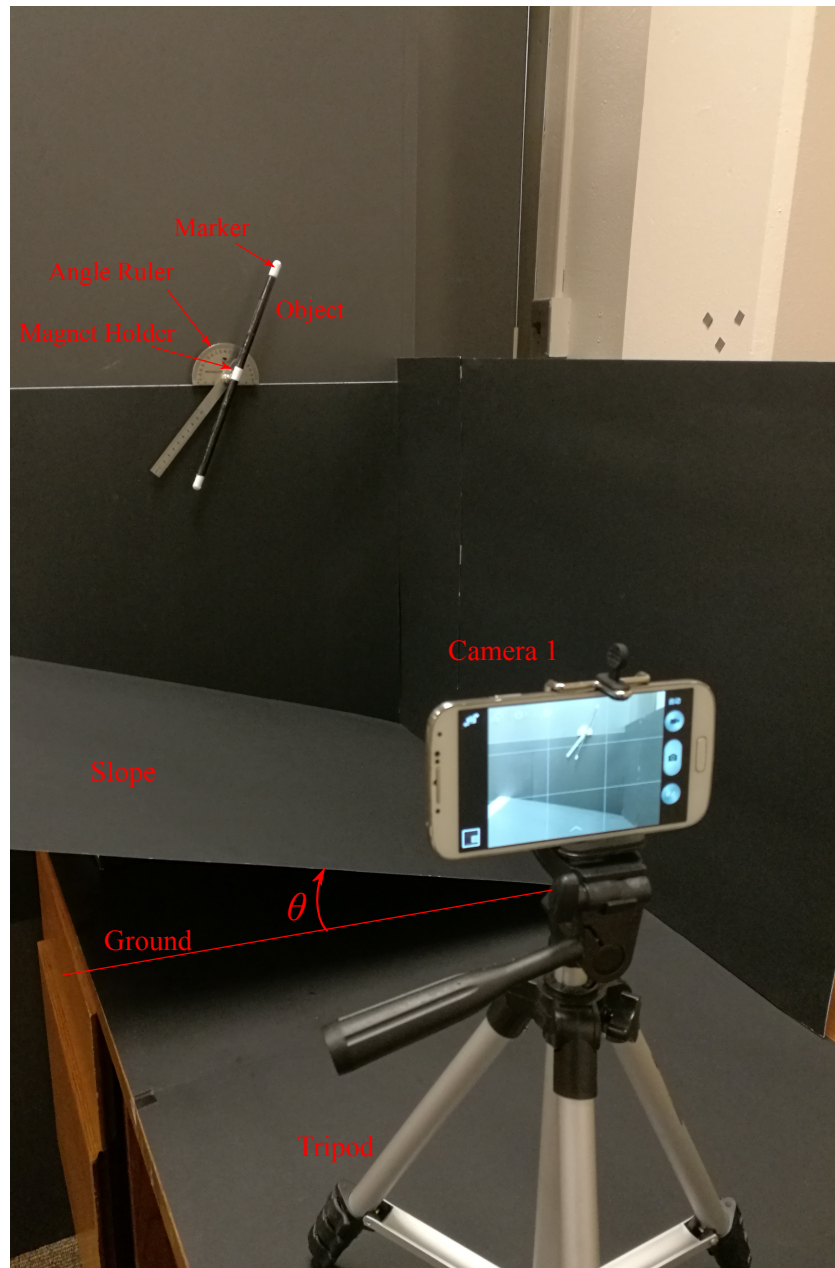


Figure 2.17: Experiment set-up



Figure 2.18: The rod

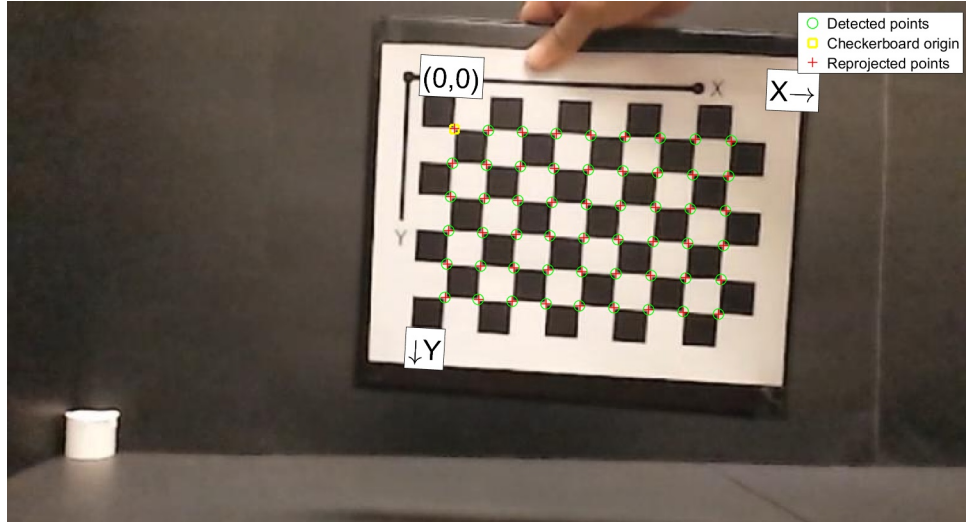


Figure 2.19: Image with identifications and green circles to indicate detected points

Single Camera Calibration

Camera Calibration is one of the most important parts in a data acquisition system. Images taken from a camera can be used to determine displacement in three dimensions of any object whose background has had a contrasting speckle pattern applied to it [57]. This non-contact optical technique can take measurements at multi-points of an object in a single snapshot. The calibration procedure listed below estimates the parameters of the camera.

1. Prepare images, camera, and calibration pattern.
2. Calibrate the camera.

Figure (2.19) displays image with IDs. The image displays the checkerboard image pair with green circles to indicate detected points. The yellow square indicates the $(0,0)$ origin. And X and Y arrows indicate the checkerboard axes orientation. After all sets of position information from images were collected and calibrated. Camera 1 and pattern positions were calculated in world coordinate as shown in Figure (2.20). In the Figure, Camera 1 was set to be the origin as $(X_C, Y_C, Z_C) = (0, 0, 0)$.

3. Evaluate calibration accuracy.

Calibration accuracy needs to be evaluated by examining the reprojection errors, the camera extrinsics, and by viewing the undistorted image (Figure (2.22)). The bar graph

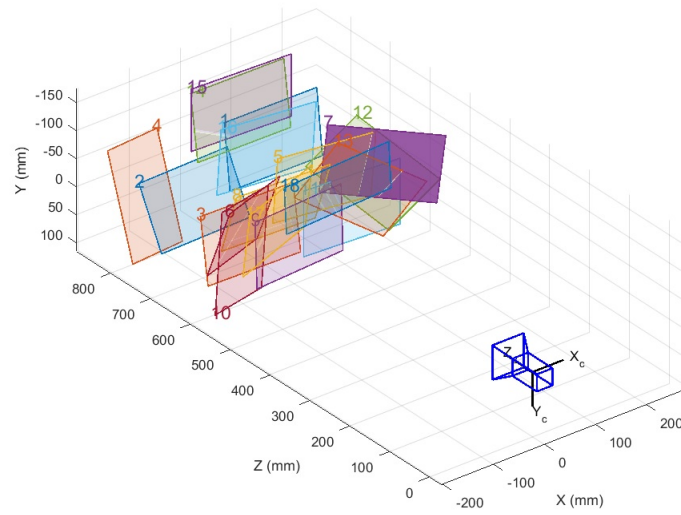


Figure 2.20: Camera 1 and pattern positions calculated in world coordinate

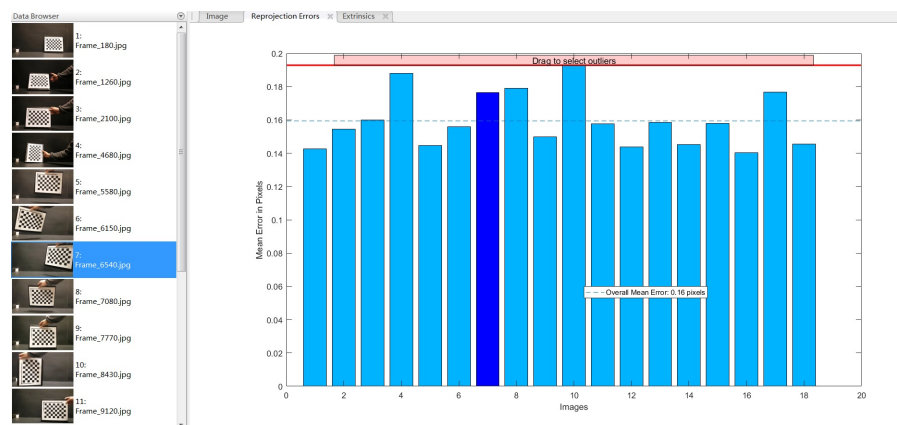


Figure 2.21: The bar graph of reprojection errors images

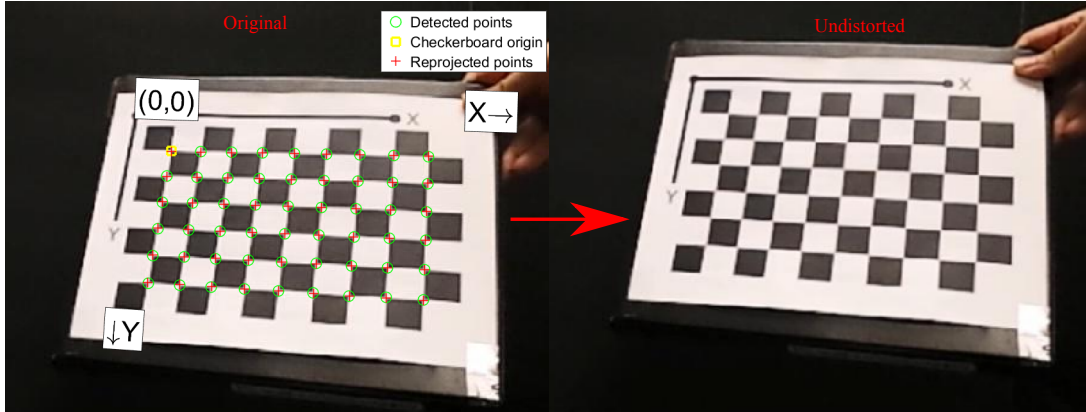


Figure 2.22: Comparison of original and undistorted images

Name	Intrinsic K	Extrinsic $[R]$	Distortion Coefficient	Mean Errors
Camera 1	$\begin{bmatrix} 741 & 0 & 0 \\ 0 & 738 & 0 \\ 398 & 239 & 1 \end{bmatrix}$	$\begin{bmatrix} 0.996 & 0.060 & -0.066 \\ -0.058 & 0.998 & 0.0355 \\ 0.068 & -0.0316 & 0.997 \end{bmatrix}$	$[0.157 - 0.405]$	0.16 pixels

Table 2.4: Parameters of camera 1

in Figure (2.21) displays the mean reprojection error per image, along with the overall mean error. The reprojection errors are the distances in pixels between the detected and the reprojected points. It calculates reprojection errors by projecting the checkerboard points from world coordinates, defined by the checkerboard, into image coordinates. Then it compares the reprojected points to the corresponding detected points. As a general rule, reprojection errors of less than one pixel are acceptable. The bar labels correspond to the image pair identifications. The highlighted pair of bars corresponds to the selected image pair.

4. Export the parameters object.

Finally, the intrinsic and extrinsic parameters of the camera, and the distortion coefficients are listed in Table (2.4) below.

Intrinsic parameters and lens distortion parameters of cameras

The intrinsic 3 by 3 matrix K shown in Eqn (4.1), contains five intrinsic parameters. These parameters are the focal length, image sensor format, and principal point. The

parameters $\alpha_x = f \cdot m_x$ and $\alpha_y = f \cdot m_y$ represent focal length in terms of pixels, where m_x and m_y are the scale factors relating pixels to distance and f is the focal length in terms of distance [57]. γ represents the skew coefficient between the x and the y axis, and is often 0. u_0 and v_0 represent the principal point, which would be ideally in the center of the image.

$$K = \begin{bmatrix} \alpha_x & \gamma & u_0 \\ 0 & \alpha_y & v_0 \\ 0 & 0 & 1 \end{bmatrix} \quad (2.84)$$

$$C[x, y, 1] = [X, Y, Z, 1] \begin{bmatrix} R \\ t \end{bmatrix} K \quad (2.85)$$

R is a 3 by 3 matrix. (X, Y, Z) are world coordinates of a point. (x, y) are coordinates of the corresponding image point. C is dimensional scale factor.

Extrinsic parameters of cameras

3 by 3 matrix R , 1 by 3 matrix T are the extrinsic parameters which denote the coordinate system transformations from 3D world coordinates to 3D camera coordinates. Equivalently, the extrinsic parameters define the position of the camera center and the camera's heading in world coordinates. T is the position of the origin of the world coordinate system expressed in coordinates of the camera-centered coordinate system. T is often mistakenly considered the position of the camera. The position, C , of the camera expressed in world coordinates is

$$C = -R^{-1}T = -R^T T$$

where R is a rotation matrix.

Processing of the kinematic data

The high speed video camera records the white markers on a black background. For each experiment, 15 frames before and 15 frames after collision were used to estimate the kinematics of the rod. The images were transferred to the computer to be processed by a Matlab program named 'MovingObjectTracking' based on Kalman filter method (developed for the motion capture) in order to digitize the position of the markers with respect to the global reference frame $x - y$. Then, the data was divided into pre- and post-collision parts. We developed an algorithm based on the free motion of the rod in the gravitational field to interpolate both pre and post position data. The angle of the rod at the contact point γ , the angular velocities of the rod immediately before and after collision $(\dot{\gamma}^-, \dot{\gamma}^+)$, and the center of mass velocities (\dot{x}^-, \dot{y}^-) , (\dot{x}^+, \dot{y}^+) were estimated from the interpolated data.

We should note that during the collision the position of the rod changes while the rod deforms. These deformations are in the scale of micrometers and so small that they could not be detected on the video images. Therefore, the experimentally obtained kinematic data only reflects the general rigid body motion of the rod. It is assumed that static friction coefficient is equal to the sliding friction coefficient during the impact.

Three examples of two-body impact are presented in Figure (2.23). For a quantitative comparison, three frames are selected in each event. Two frames come from before and after an impact, and the other frame comes from the instant of impact. The time interval between each frame is $\frac{1}{120}$ second. Experiment A shows the sticking mode in frictional impact and reveals the value of the restitution coefficient. Experiment B shows the sliding mode and reveals the value of the friction coefficient during the impact. Experiment C shows the reverse sliding mode in frictional impact. For all cases, the moving rod initially has only a vertical pre-impact velocity and no angular velocity.

In Experiment A, the rod is dropped from a height h vertically and the ground has the slope angle of 15° . In Experiment B, the rod is dropped from a certain height h vertically and the slope angle of the ground is 45° . Throughout the experiment, the friction coefficient during impact was evaluated as 0.195 and it can be verified by Eqn.

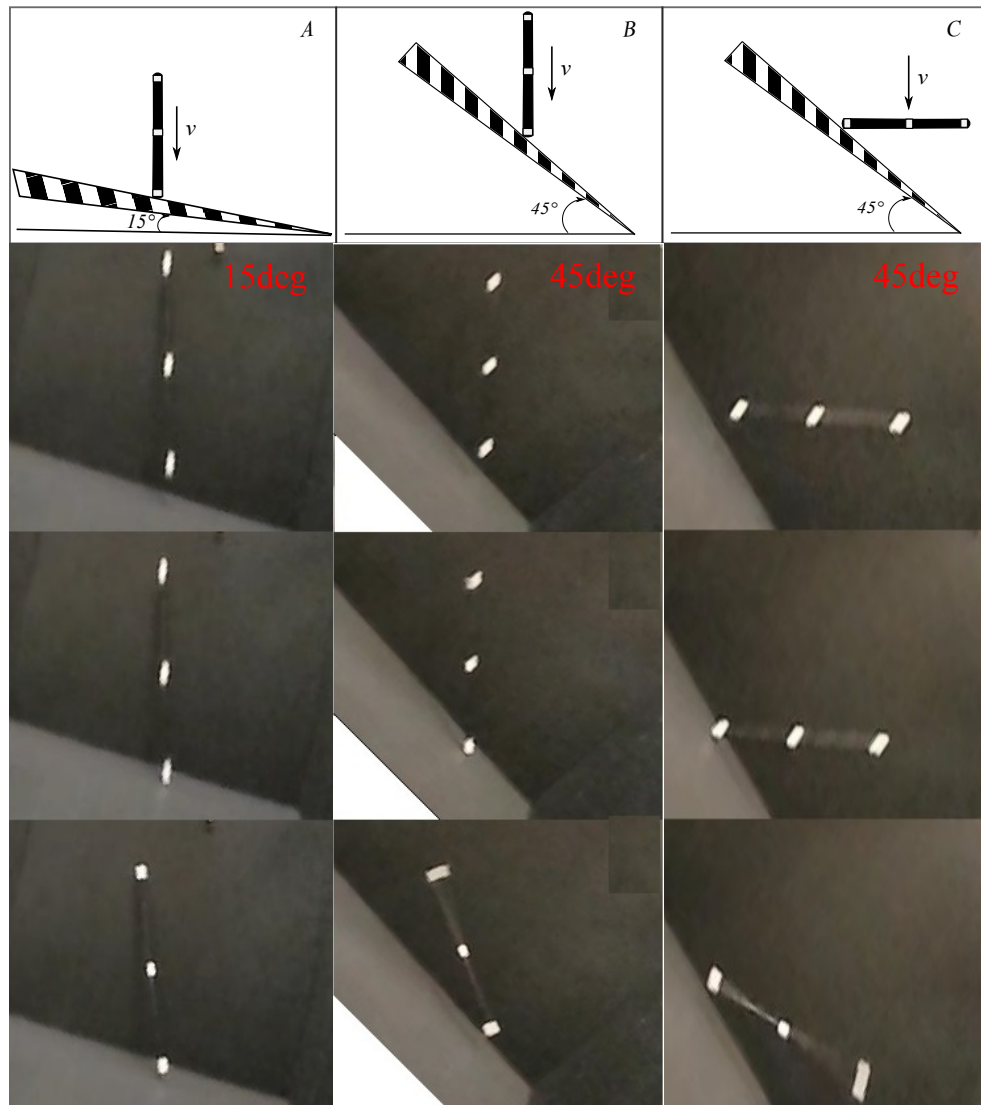


Figure 2.23: Experiments A, B & C

Experiments	$p = \frac{v_x}{v_y}$	γ	e_n	Case	Comparison	Energy Dissipation
EX. A	0.258	$\frac{7\pi}{12}$	0.395	case #3 (Sticking)	Experiment	55.6%
					Newton's	52.3%
					Stronge's	52.3%
					Poisson's	52.3%
EX.B	1	$\frac{3\pi}{4}$	0.395	case #0 (Sliding)	Experiment	66.5%
					Newton's	64.3%
					Stronge's	65.9%
					Poisson's	64.3%
EX.C	1	$\frac{5\pi}{4}$	0.264	case #2 (Reverse Sliding)	Experiment	75.4%
					Newton's	69.8%
					Stronge's	77.2%
					Poisson's	68.6%

Table 2.5: Quantitative comparison for two-body impact: $\mu = 0.195$

(2.33). In Experiment C, the rod is dropped from a height h vertically and the slope angle of the gate changes to 45° . Since the slope angle is 15° instead of 45° , the COR value e_n is evaluated to be 0.264 by the ratio of rebound height and the initial release height h . Note that the difference in COR between experiments is due to change in the slope angle, similar but different set-ups, gates, and parts. All these experimental results were compared to analytical results assuming different cases of impact. From Table (2.5), the simulation results agree very well with our experimental results. Moreover, between these three hypothesis models, simulation based on Stronge's hypothesis has the most accurate and closest results. Also, experimental and analytical results vary the most in reverse sliding which is expected as the physics of the impact is more complicated in reverse sliding.

2.10 Discussion and Conclusion

In this chapter, we have systematically analyzed the planar rigid body impact model using different coefficient of restitution hypothesis such as Newton's, Stronge's and Poisson's models. During impact, two stages, compression and restitution, can be identified, because different modes of impact occur at different stages throughout the impact. The possible modes are concluded and applied to the general system impact response analysis. It can be shown, analytically and experimentally, that seven cases of impact, such as sliding in compression and reverse sliding in restitution, exist. All these cases of impact are characterized and formulated into a general computational strategy. Parameter evaluation is also discussed for practicality in this chapter. Among these four initial parameters, velocity p , orientation angle γ , the coefficient of restitution e_n and coefficient of friction μ , γ has the greatest influence on energy dissipation when $0.2 < \mu < 0.6$ and $0.2 < e_n < 0.8$. Since variation of orientation angle γ causes different modes while sliding or reverse sliding leads to more energy dissipation than sticking. Different models of friction coefficient (μ_k and μ_s) lead to different results in the transition area between sticking and reverse sliding. The larger differences between μ_k and μ_s values, the bigger transition area and difference of energy dissipation. And this difference results in a discontinuity of velocity.

Based on the comparison of our simulation and experimental data, simulation results agree very well with the experimental results. From Table (2.5), the energy dissipation is always positive. In sticking mode, energy dissipation holds the same value of energy dissipation in both COR models. In sliding and reverse sliding modes, Poisson's and Stronge's models dissipate more energy than Newton's model, and the largest difference between the models exists in the reverse sliding mode. The reason is, as we discussed COR models in chapter 1, Newton's and Poisson's models are inconsistent when $e_n = 1$ and they can produce non-zero energy dissipation in the normal direction. The error varies from 0.91% to 9.02% in different cases, and we have the minimum error, which varies from 0.91% to 5.94%, by using simulation based on Stronge's hypothesis. Overall, it appears that Stronge's hypothesis of restitution is the better of three theories so we

will continue to use Stronge's coefficient of restitution model as our e_n in the next chapter when we discuss three-dimensional rigid body impact.

Chapter 3

Three Dimensional Rigid Body Impact Mechanics

We have thus far, presented a complete analysis and solution of a planar rigid body impact, and have considered a special case which is the impact of a falling rod to the ground. In this chapter, we extend the formulation to three dimensional impact. The primary difference is that we will be dealing with three components of impulsive force, three components of velocity, and three components of angular velocity. This brings the total number of unknowns to nine instead of five, therefore we will require at least that many governing equations to close the system.

3.1 Description of Three Dimensional Rigid Body Impact Model

For consistency, let us define a coordinate system which is identical to what was used for the planar analysis. The (x, z) plane is the plane of impact. The position vector between the center of mass and the contact point will now be a three dimensional vector, whose orientation will be defined by the angles of this vector with respect to the coordinate axes. These direction angles from the x -axis, y -axis, and z -axis are β , γ , and δ , respectively, as shown in Fig (3.1).

The magnitude of the position vector from the contact point to the center of mass will be defined as \vec{R} and assumed to remain constant. We can now express the position vector in terms of its components.

$$\vec{R} = R_x \vec{i} + R_y \vec{j} + R_z \vec{k} \tag{3.1}$$

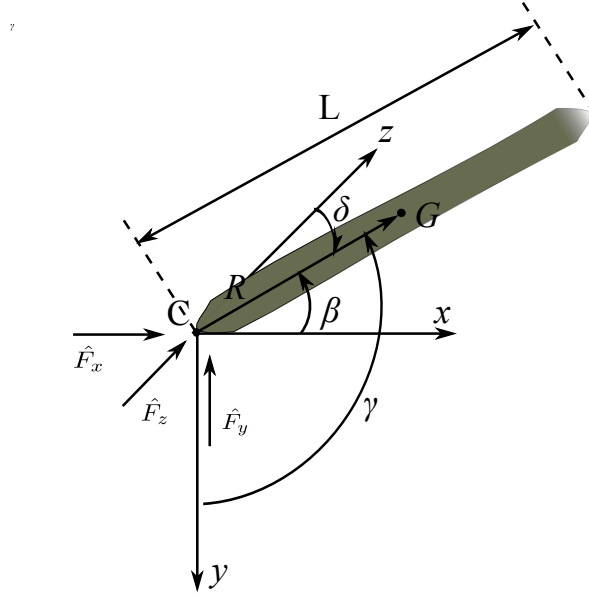


Figure 3.1: Falling rod colliding with ground in three dimension

$$R_x = R \cos(\beta) \quad R_y = R \cos(\gamma) \quad R_z = R \cos(\delta) \quad (3.2)$$

Parallel to the formulation for planar impact in Chapter 2 we express the initial velocity and angular velocity of the center of mass in terms of their components as follows.

$$\vec{V} = V_x \vec{i} + V_y \vec{j} + V_z \vec{k} \quad (3.3)$$

$$\vec{\omega} = \omega_x \vec{i} + \omega_y \vec{j} + \omega_z \vec{k} \quad (3.4)$$

The contact point velocity \vec{V}^C at the beginning of impact becomes

$$\vec{V}^C = \vec{V} + \vec{\omega} \times \vec{R} \quad (3.5)$$

$$\vec{V}^C = (V_x + \omega_y R_z - \omega_z R_y)\vec{i} + (V_y + \omega_z R_x - \omega_x R_z)\vec{j} + (V_z + \omega_x R_y - \omega_y R_x)\vec{k} \quad (3.6)$$

Similarly, we can define the velocity, angular velocity, and contact point velocity immediately after impact by

$$\vec{V}' = V'_x \vec{i} + V'_y \vec{j} + V'_z \vec{k} \quad (3.7)$$

$$\vec{\omega}' = \omega'_x \vec{i} + \omega'_y \vec{j} + \omega'_z \vec{k} \quad (3.8)$$

$$\vec{V}'^C = (V'_x + \omega'_y R_z - \omega'_z R_y)\vec{i} + (V'_y + \omega'_z R_x - \omega'_x R_z)\vec{j} + (V'_z + \omega'_x R_y - \omega'_y R_x)\vec{k} \quad (3.9)$$

Figure (3.1) illustrates the impulsive forces acting at the contact point during impact. Note that the selected direction of the tangential impact forces, \hat{F}_x and \hat{F}_z , is somewhat arbitrary since they both depend on the direction of the contact point velocity. Using the general principle of linear momentum conservation we write the following equations

$$mv_x + \hat{F}_x = mv'_x \quad (3.10)$$

$$mv_y + \hat{F}_y = mv'_y \quad (3.11)$$

$$mv_z + \hat{F}_z = mv'_z \quad (3.12)$$

The general expression for the angular momentum for three dimensional motion is

$$\frac{d}{dt}\vec{H}_G = \vec{M}_G = \vec{R} \times \vec{F} \quad (3.13)$$

where \vec{F} is the impact force. We can also express the conservation of angular momentum as follows:

$$\vec{H}_G - \vec{H}'_G = \int_{t_1}^{t_2} (\vec{R} \times \vec{F}) dt = \vec{R} \times \hat{\vec{F}} \quad (3.14)$$

Let us first consider the $\vec{R} \times \hat{\vec{F}}$ term, which can be explained as

$$\vec{R} \times \hat{\vec{F}} = (R_x \vec{i} + R_y \vec{j} + R_z \vec{k}) \times (\vec{F}_x \vec{i} + \vec{F}_y \vec{j} + \vec{F}_z \vec{k}) \quad (3.15)$$

$$\vec{R} \times \hat{\vec{F}} = (R_y \vec{F}_z - R_z \vec{F}_y) \vec{i} + (R_z \vec{F}_x - R_x \vec{F}_z) \vec{j} + (R_x \vec{F}_y - R_y \vec{F}_x) \vec{k} \quad (3.16)$$

The initial angular momentum of a rigid body in general three dimensional motion can be shown to be

$$\vec{H}_G = (I_{xx}\omega_x - I_{xy}\omega_y - I_{xz}\omega_z) \vec{i} + (-I_{yx}\omega_x + I_{yy}\omega_y - I_{yz}\omega_z) \vec{j} + (-I_{zx}\omega_x - I_{zy}\omega_y + I_{zz}\omega_z) \vec{k} \quad (3.17)$$

$$\vec{H}'_G = (I_{xx}\omega'_x - I_{xy}\omega'_y - I_{xz}\omega'_z) \vec{i} + (-I_{yx}\omega'_x + I_{yy}\omega'_y - I_{yz}\omega'_z) \vec{j} + (-I_{zx}\omega'_x - I_{zy}\omega'_y + I_{zz}\omega'_z) \vec{k} \quad (3.18)$$

where I_{pq} for $p, q = x, y, z$ defines the inertia matrix for the body. Equating components for xyz axis in Eqns. (3.16,3.17) and (3.18) and separating known and unknown quantities, we get:

$$(I_{xx}\omega'_x - I_{xy}\omega'_y - I_{xz}\omega'_z) + (R_y \vec{F}_z - R_z \vec{F}_y) = (I_{xx}\omega_x - I_{xy}\omega_y - I_{xz}\omega_z) \quad (3.19)$$

$$(-I_{yx}\omega'_x + I_{yy}\omega'_y - I_{yz}\omega'_z) + (R_z\vec{F}_x - R_x\vec{F}_z) = (-I_{yx}\omega'_x + I_{yy}\omega'_y - I_{yz}\omega'_z) \quad (3.20)$$

$$(-I_{zx}\omega'_x - I_{zy}\omega'_y + I_{zz}\omega'_z) + (R_x\vec{F}_y - R_y\vec{F}_x) = (-I_{zx}\omega_x - I_{zy}\omega_y + I_{zz}\omega_z) \quad (3.21)$$

Using the basic concepts of rigid body dynamics we have derived six equations (3.10,3.11,3.12) and (3.19,3.20,3.21). There are nine unknowns: $v'_x, v'_y, v'_z, \omega'_x, \omega'_y, \omega'_z$ and $\hat{F}'_x, \hat{F}'_y, \hat{F}'_z$. Therefore we need three more equations. These equations will come from considering restitution and friction. They will be derived in the following sections.

3.2 Compression and Restitution stages conditions in Three Dimensions

As we discussed in the previous chapter, the impact can be divided into two stages, compression and restitution. The end of compression stage condition can be expressed as

$$\vec{V}^C \cdot \vec{j} = 0 \quad (3.22)$$

Substituting Eqn. (3.9) into Eqn. (3.22), we get

$$(V'_y + \omega'_z R_x - \omega'_x R_z) = 0 \quad (3.23)$$

As discussed in the conclusion of Chapter 2, Stronge's hypothesis is the best coefficient of restitution model since it has the best simulation results among three hypotheses and Newton's and Poission's hypotheses lead to negative energy dissipation in several reverse sliding cases. Therefore, the end of restitution stage condition using Stronge's hypothesis can be stated as

$$e_n^2 = \frac{W_r}{-W_c} \quad (3.24)$$

Once again, W_c and W_r are the work done by the normal contact force during the compression and the restitution stages, respectively.

3.3 Calculation of rotated inertia matrix $[I_G^{xyz}]$

Euler angles are a means of representing the spatial orientation of any reference frame (coordinate system or basis) as a composition of three elemental rotations starting from a known standard orientation, represented by another frame (sometimes referred to as the original or fixed reference frame, or standard basis). The reference orientation can be an initial orientation from which the frame virtually rotates to reach its actual orientation. In the following, the axes of the original and reference frame are denoted by x, y, z and the axes of the body frame are denoted as X, Y, Z . In geometry and physics, the rotated coordinate system is often imagined to be attached to the rigid body. In this case, XYZ is referred to a "local" coordinate system, and it is meant to represent both the position and the orientation of the body. The geometrical definition (referred sometimes as static) of the Euler angles is based on the axes of the above-mentioned (original and rotated) reference frames and an additional axis called the line of nodes. The line of nodes (N) is defined as the intersection of the $x - z$ and the $X - Z$ planes as shown in Figure (3.2). In other words, it is a line passing through the common origin of both frames, and perpendicular to the $y - Y$ plane, on which both y and Y lie. In general, an Euler angle transformation can be accomplished in 12 different ways. We are considering one of them here. The three Euler angles are defined as follows:

1. θ_1 is the angle between the z axis and the N axis.
2. θ_2 is the angle between the y axis and the Y axis.
3. θ_3 is the angle between the N axis and the Z axis.

This definition implies that:

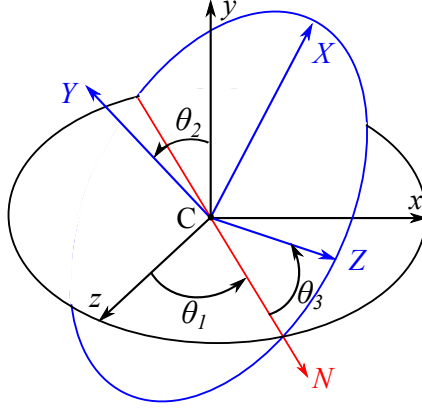


Figure 3.2: Rotations from xyz to XYZ coordinate

1. θ_1 represents a rotation around the y axis,
2. θ_2 represents a rotation around the N axis,
3. θ_3 represents a rotation around the Y axis.

This rotation sequence is a commonly used Euler angle sequence [9], often used to describe rotating rigid bodies. If θ_2 is zero, there is no rotation about N . As a consequence, Y coincides with y , θ_1 and θ_3 represent rotations about the same axis y , and the final orientation can be obtained with a single rotation about y , by an angle equal to $\theta_1 + \theta_3$.

It is easier to get the position/motion information from a reference frame rather than a body attached frame, we focus on how to get the rotated inertia matrix in reference frame rather than body attached frame. We use a rotation matrix $[Q]$ to represent the rotation matrix from the reference frame xyz coordinate to a body frame XYZ coordinate as the object hits the ground at contact point C . To calculate the rotated inertia matrix, we need to define the rotation matrix first. It can be stated as

$$[Q]^T = [R(\theta_3)][R(\theta_2)][R(\theta_1)] \quad (3.25)$$

The inertia matrix in its principal XYZ coordinate is

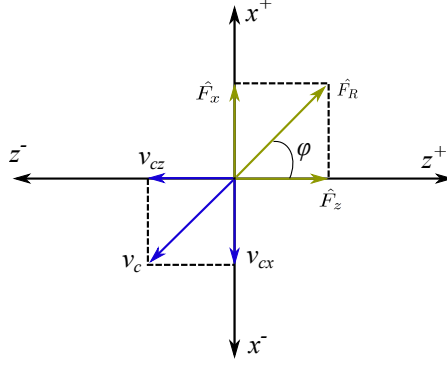


Figure 3.3: Tangential impulses in $x - z$ plane (the impact plane)

$$[I_G^{XYZ}] = \begin{bmatrix} I_{XX} & -I_{XY} & -I_{XZ} \\ -I_{YX} & I_{YY} & -I_{YZ} \\ -I_{ZX} & -I_{ZY} & I_{ZZ} \end{bmatrix} \quad (3.26)$$

The rotated inertia matrix in reference frame is calculated by

$$[I_G^{xyz}] = [Q]^T [I_G^{XYZ}] [Q] \quad (3.27)$$

Substitute Eqn. (4.17) (3.26) into Eqn. (3.27), we will get the rotated inertia matrix $[I_G^{xyz}]$ in reference frame xyz .

3.4 Tribology of Impact in Three Dimensions

We will consider contact surfaces which can be defined by a single, constant-valued, coefficient of friction μ . For this problem, sliding will occur if the maximum tangential impulse \hat{F}_R is large enough to overcome friction, which is defined by its components \hat{F}_x and \hat{F}_z .

From Figure (3.3) we can show that the components, magnitude, and orientation of the maximum tangential force impulse are

$$\hat{\vec{F}}_R = \hat{F}_R(\sin(\phi)\hat{i} + \cos(\phi)\hat{k}) = \hat{F}_x\hat{i} + \hat{F}_z\hat{k} \quad (3.28)$$

$$\hat{F}_R = \sqrt{\hat{F}_x^2 + \hat{F}_z^2} \quad (3.29)$$

So if the object slides, the ratio of the maximum tangential force impulse to the vertical impulse is equal to the coefficient of friction μ .

$$\mu = \left| \frac{\hat{F}_R}{\hat{F}_y} \right| = \frac{\mu_x}{\sin(\phi)} = \frac{\mu_z}{\cos(\phi)} \quad (3.30)$$

$$\hat{F}_R = \frac{\hat{F}_x}{\sin(\phi)} = \frac{\hat{F}_z}{\cos(\phi)} \quad (3.31)$$

where the angle ϕ has a range of $0 \leq \phi \leq 2\pi$.

3.4.1 Sticking Mode in Three Dimensions

As discussed in previous sections, if the impacting body does not slide during impact, the final velocity components of the contact point, tangential to the impact surface, will be zero. For the three-dimensional case this can be stated as

$$\vec{V}^{\prime C} \cdot \vec{i} = 0 \quad (3.32)$$

$$\vec{V}^{\prime C} \cdot \vec{k} = 0 \quad (3.33)$$

Substituting Eqn. (3.9) into Eqn. (3.32,3.33)

$$(V'_x + \omega'_y R_z - \omega'_z R_y) = 0 \quad (3.34)$$

$$(V'_z + \omega'_x R_y - \omega'_y R_x) = 0 \quad (3.35)$$

3.4.2 Sliding Mode in Three Dimensions

Let us consider impact when the object slides. Using the Coulomb Law of friction, separating the tangential impulsive force \hat{F}_R into each coordinate direction, \hat{F}_x and \hat{F}_z , and assuming the coefficient of friction μ is uniform along the tangential plane, we get the following equations

$$\mu_x = \left| \frac{\hat{F}_R}{\hat{F}_y} \right| = \frac{\hat{F}_x}{\hat{F}_y \cdot \sin(\phi)} \cdot \text{sgn}(-\vec{V}^C \cdot \vec{i}) \quad (3.36)$$

$$\mu_z = \left| \frac{\hat{F}_R}{\hat{F}_y} \right| = \frac{\hat{F}_z}{\hat{F}_y \cdot \cos(\phi)} \cdot \text{sgn}(-\vec{V}^C \cdot \vec{k}) \quad (3.37)$$

$$\mu = \frac{\mu_x}{\sin(\phi)} = \frac{\mu_z}{\cos(\phi)} \quad (3.38)$$

$$S_x = -\text{sign}(\vec{V}^C \cdot \vec{i}) \quad S_z = -\text{sign}(\vec{V}^C \cdot \vec{k}) \quad (3.39)$$

Substituting Eqn. (3.6) into Eqns. (3.36,3.37) we obtain

$$\mu_x = \frac{\hat{F}_x}{\hat{F}_y \cdot \sin(\phi)} \cdot \text{sign}(-(V_x + \omega_y R_z - \omega_z R_y)) = \frac{\hat{F}_x}{\hat{F}_y \cdot \sin(\phi)} \cdot S_x \quad (3.40)$$

$$\mu_z = \frac{\hat{F}_z}{\hat{F}_y \cdot \cos(\phi)} \cdot \text{sign}(-(V_z + \omega_x R_y - \omega_y R_x)) = \frac{\hat{F}_z}{\hat{F}_y \cdot \cos(\phi)} \cdot S_z \quad (3.41)$$

We have now developed the systems of equations required to analyze both the sliding, reverse sliding and sticking cases. But we must once again determine when to use which set of equations. As was stated earlier, if a single valued coefficient of friction μ can be used, the sliding region will be initiated by the maximum tangential force impulse. The sliding condition becomes

$$\mu < \frac{\sqrt{\hat{F}_x^2 + \hat{F}_z^2}}{\hat{F}_y} \quad (3.42)$$

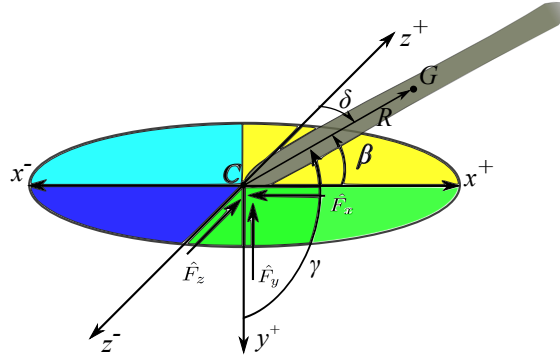


Figure 3.4: Reverse Sliding in (x, z) plane

3.4.3 Reverse Sliding Mode in Three Dimensions

In general, the governing equations for reverse sliding mode are the same as sliding mode except the sign of impulsive forces \hat{F}_x and \hat{F}_z . However, in Figure (3.4) we notice that there are three possibilities of the reverse sliding mode. If the object is sliding in (x^+, z^+) region at the beginning of impact, it can reverse slide in either (x^+, z^-) , (x^-, z^+) or (x^-, z^-) region. In order to determine the region of reverse sliding, we set up the following criterions:

1. If $0 \leq \delta \leq \frac{\pi}{2}$ and $0 \leq \beta \leq \frac{\pi}{2}$, reverse sliding occurs in (x^-, z^-) region.
2. If $0 \leq \delta \leq \frac{\pi}{2}$ and $\frac{\pi}{2} < \beta < \pi$, reverse sliding occurs in (x^-, z^+) region.
3. If $\frac{\pi}{2} < \delta < \pi$ and $0 \leq \beta \leq \frac{\pi}{2}$, reverse sliding occurs in (x^+, z^+) region.

We need to consider these three possibilities during compression and restitution, as well.

The object will slide or reverse slide if the force ratio exceeds the value of the presented coefficient of friction μ on both tangential direction x and z .

3.5 Cases of Impact

As discussed in Chapter 2, impact can be separated into two stages: compression and restitution. Any of modes discussed, sliding, sticking, reverse sliding, can happen during these two stages. We recall that once the motion changes from sliding mode to sticking or reverse sliding modes, there is no other impulsive force which can change the modes back to original mode again. As a result, we identify 11 possible cases, 0, 1, 2a, 2b, 2c, 3, 4a, 4b, 4c, 5, and 6, which are listed in Table (3.1). Since three possible motions could take place in a friction plane, there are three possibilities in both reverse sliding cases #2 and #4 as reverse sliding can also take place in three different ways. The system finishes one impact at the end of restitution. Note that, the last two cases take place only when both horizontal velocities (x, z) of the contact point C are zero when impact begins. Figures (3.5) and (3.6) are flow charts for the three-dimensional impact system that expands Table (3.1).

3.6 Summary of the Procedure

We have set up all equations and assumptions for different cases in three dimensional impact. Now we can formulate the general procedure of solving a three dimensional impact problem. Assuming the object always has an initial velocity and sliding at the beginning of impact and the object's orientation and physical parameters are given, we can begin the analysis by determining the inertia matrix I_G^{xyz} in the xyz coordinate system. In the general case, two or three rotations may be needed to perform this rotation. The components of the position vector can be calculated by using six Eqns. (3.10,3.11,3.12), (3.19,3.20,3.21) and three equations based on different modes and compression or restitution conditions. All of these parameters as well as the initial velocities and rotations are then substituted into matrix form. Once the solution is obtained, the horizontal contact point velocity v_{cx} and v_{cz} need to be bigger than zero. Otherwise, we must resolve the problem using the equations for the sticking then reverse sliding mode. In the sticking mode, the components of the impact impulses should be substituted into Eqn. (3.40,3.41) in order to check the validity of the no sliding assumption. If








Case #	Color Code	Value	Initial Condition	Compression Stage	Restitution Stage
0		0	$v_{cx} \neq 0$ or $v_{cz} \neq 0$	Sliding	Sliding
1		1	$v_{cx} \neq 0$ or $v_{cz} \neq 0$	Sliding ends, Sticking begins	Sticking
2		2	$v_{cx} \neq 0$ or $v_{cz} \neq 0$	Sliding ends, Reverse Sliding begins	Reverse Sliding
2(a)		2.25	$v_{cx} > 0$ and $v_{cz} < 0$	(x^+, z^-)	(x^+, z^-)
2(b)		2.5	$v_{cx} < 0$ and $v_{cz} > 0$	(x^-, z^+)	(x^-, z^+)
2(c)		2.75	$v_{cx} < 0$ and $v_{cz} < 0$	(x^-, z^-)	(x^-, z^-)
3		3	$v_{cx} \neq 0$ or $v_{cz} \neq 0$	Sliding	Sliding ends, Sticking begins
4		4	$v_{cx} \neq 0$ or $v_{cz} \neq 0$	Sliding	Sliding ends, Reverse Sliding begins
4(a)		4.25	$v_{cx} > 0$ and $v_{cz} > 0$	(x^+, z^+)	(x^+, z^-)
4(b)		4.5	$v_{cx} > 0$ and $v_{cz} > 0$	(x^+, z^+)	(x^-, z^+)
4(c)		4.75	$v_{cx} > 0$ and $v_{cz} > 0$	(x^+, z^+)	(x^-, z^-)
5		5	$v_{cx} = 0$ and $v_{cz} = 0$	Sticking	Sticking
6		6	$v_{cx} = 0$ and $v_{cz} = 0$	Sticking ends, Reverse Sliding begins	Reverse Sliding

Table 3.1: Cases for three-dimensional impact

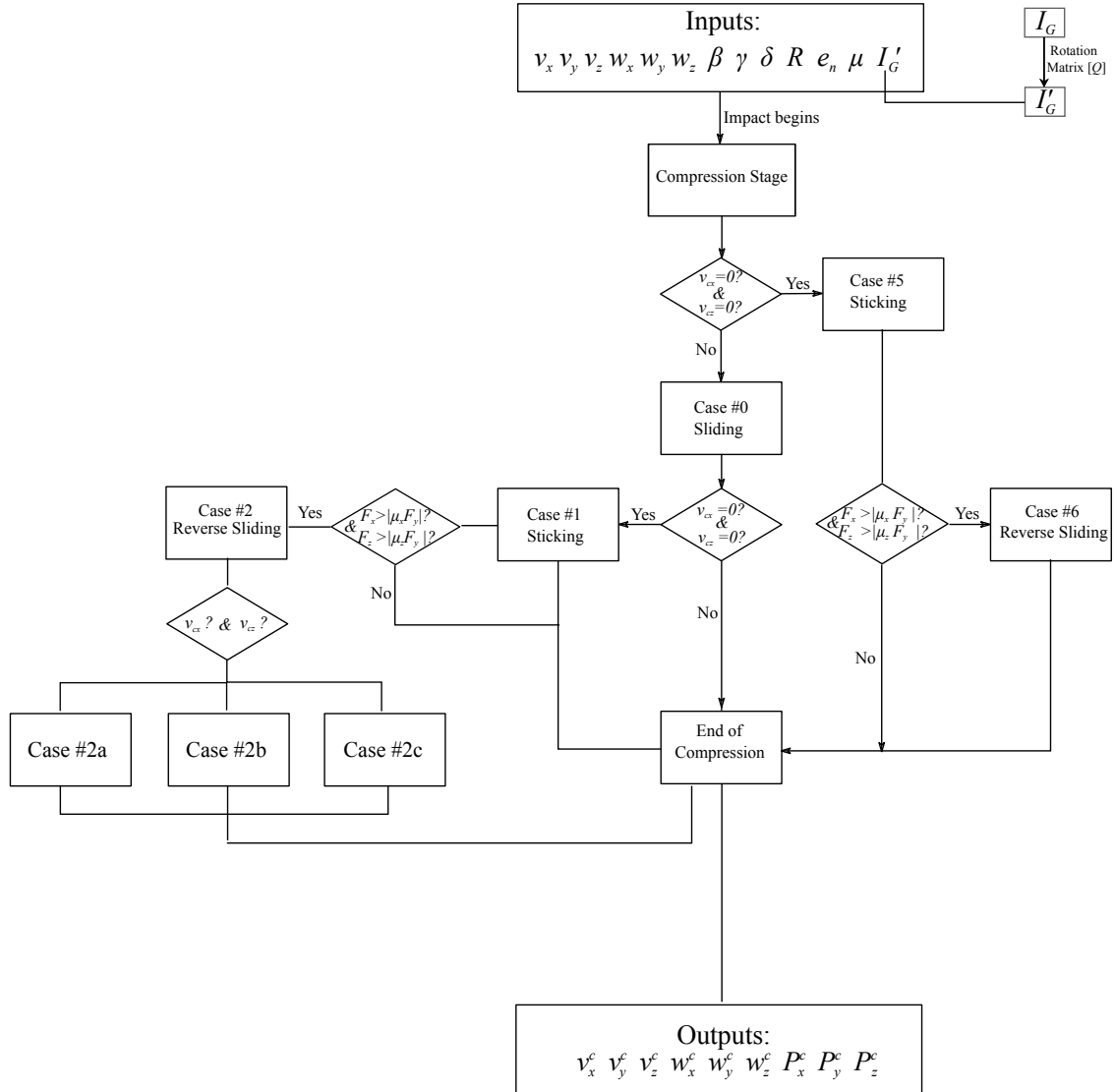


Figure 3.5: 3D Flow chart for compression impulse computation

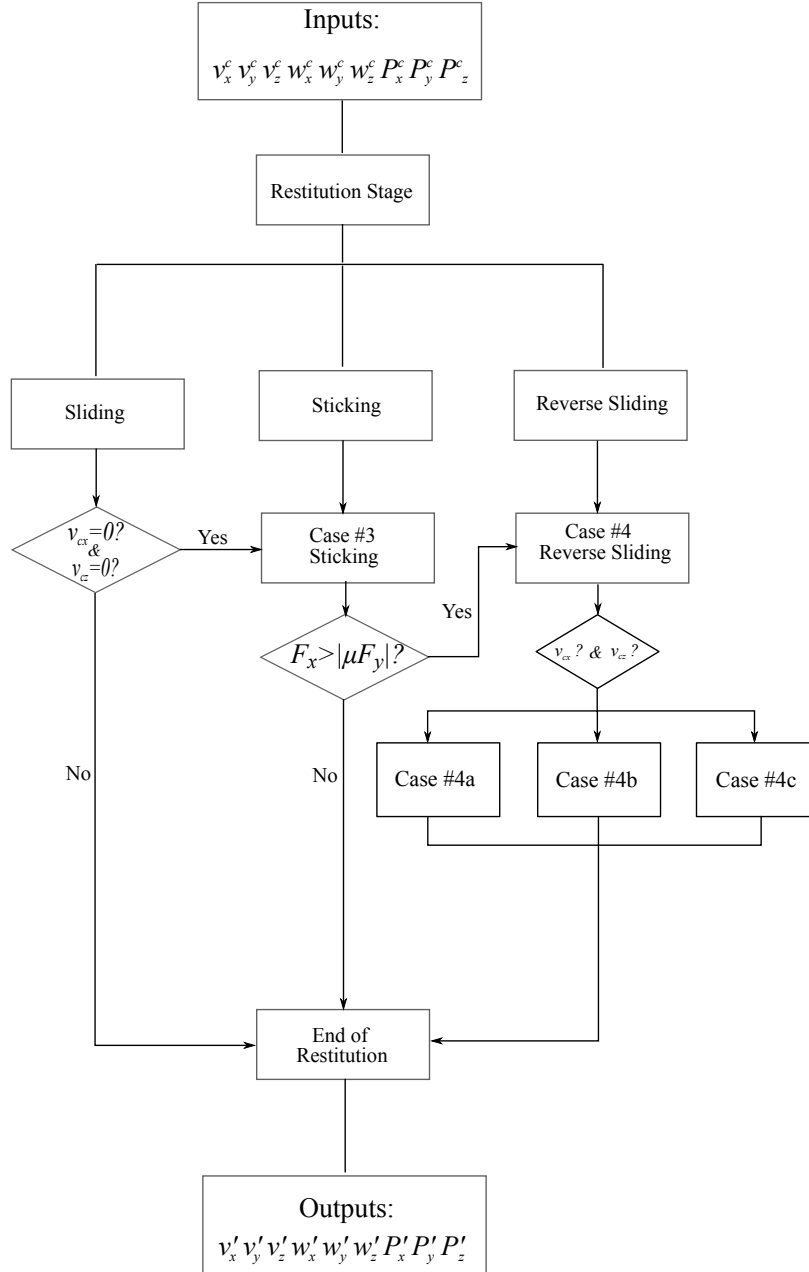


Figure 3.6: 3D Flow chart for restitution impulse computation

this criterion is satisfied the solution is valid. If not, we need to update the directional of impulsive friction force. This can be done by determining the direction of orientation angles δ and β and substituting these values again into matrix. Each of the stage affiliated with sliding, sticking or reverse sliding leads to a different set of 9 equations.

3.7 Numerical Examples

This section applies the impact model with tangential compliance to three kinds of objects colliding with the ground: a spherical ball, a rod and a rectangular bar. A study on the spherical ball provides us a simplest example in 3D impact simulation study. For the rod example, when its cap radius $r\frac{1}{20}L$ which L is the total length, the mass moment of inertia along its length is negligible and we can focus on analyzing its velocity and two directions angular velocity. The rectangular bar is the most complicated among these three examples. It has six dynamic quantities, $v_x, v_y, v_z, \omega_x, \omega_y, \omega_z$ that need to be analyzed.

Running a single impact simulation according to the summary of the procedure in section 3.6 and the flow chart in section 3.5, we obtain the post-impact dynamic quantities with initial inputs.

In matrix notation, the impulse relations can be expressed as

$$\begin{matrix} [A] & [V'] \\ 9 \times 9 & 9 \times 1 \end{matrix} = \begin{matrix} [V] \\ 9 \times 1 \end{matrix} \quad (3.43)$$

where the coefficient matrices $[A]$ is a 9×9 matrix and the column matrices $[V]$ and $[V']$ contain the final and initial quantities, respectively. Therefore the solution can be expressed as

$$\begin{matrix} [V'] \\ 9 \times 1 \end{matrix} = \begin{matrix} [A]^{-1} & [V] \\ 9 \times 9 & 9 \times 1 \end{matrix} \quad (3.44)$$

We choose different conditions in different stages using Eqn. (3.10), (3.11), (3.12), (3.19), (3.20), (3.21) and either (3.34), (3.35), (3.24) or (3.34), (3.35), (3.24). A list of the parameters used and calculated is shown in Table (3.2).

Note that, μ is replaced by μ_s when a two-coefficient representation of friction (μ_s, μ_k) is used.

Initial Parameters	$v_x, v_y, v_z, w_x, w_y, w_z, \gamma, \beta, \delta, \mu, R, I_G, e_n$
Parameters in Compression	$V_x^c V_y^c V_z^c \omega_x^c \omega_y^c \omega_z^c \hat{F}_x^c \hat{F}_y^c \hat{F}_z^c$
Parameters in Restitution	$V_x^r V_y^r V_z^r \omega_x^r \omega_y^r \omega_z^r \hat{F}_x^r \hat{F}_y^r \hat{F}_z^r$
Post-impact Dynamic Quantities	$V_x' V_y' V_z' \omega_x' \omega_y' \omega_z' \hat{F}_x' \hat{F}_y' \hat{F}_z'$

Table 3.2: Parameters used in a single impact simulation

3.7.1 Impact of a Falling Ball with the Ground

Cross [42] investigated frictional impact of a ball on a cart, modeling tangential compliance by allowing the cart, attached to a vertical wall via a spring at one end, to translate horizontally. His analysis was performed in time-space in a way similar to Stronge's [18] with simulation results showing a range of spins of the rebounding ball. Han [44] investigated frictional impact of a ball on a table using the introduced compliance model. His analysis extends Stronge's spring-based planar contact structure to three dimensions by modeling the contact point as a massless particle able to move tangentially on one body while connected to an infinitesimal region on the other body via three orthogonal springs.

Here we treat a ball-ground impact in impulse space using our model in Section 3.4.1. As shown in Figure (3.7), a ball with initial velocity V_0 and angular velocity ω_0 strikes the ground. Let R be the ball's radius and m is its mass. Its mass moment of inertia(in every direction) is $\frac{2}{5}mR^2$. Denote by the tangential impulse forces \hat{F}_X and \hat{F}_Y exerted by the ground on the ball during the impact. We place the origin at the contact point. The (X, Y, Z) frame is identical to the (x, y, z) contact frame for tangential impulse forces.

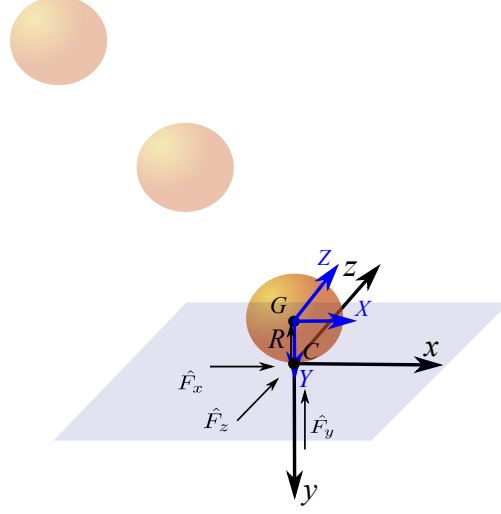


Figure 3.7: A bounce of a ball colliding with ground in three dimensions

In all simulations in this section, we consider $R = 1$, $m = 1$, and set the coefficient of friction, the coefficient of restitution, and the moment of inertia as follows:

$$\mu = 0.4 \quad e_n = 0.6 \quad I_G^{xyz} = \alpha m R^2 = \frac{2}{5} m R^2 \quad (3.45)$$

The initial velocity, angular velocity and direction angles settings are as follows:

$$-1 \leq v_x \leq 1 \quad v_y = 1 \quad v_z = 0 \quad (3.46)$$

$$-1 \leq \omega_x \leq 1 \quad \omega_y = 0 \quad \omega_z = 0 \quad (3.47)$$

Since the reference frame xyz and the body attached frame XYZ coincide with each other, the orientation angles can be defined as follows:

$$\beta = \gamma = \delta = 0 \quad (3.48)$$

Also, the Euler angles $\theta_1 = \theta_2 = \theta_3 = 0$.

Sticking condition

The system of equations for three dimensional impacts in sticking mode are: Eqns. (3.10,3.11,3.12,3.19,3.20,3.21) and (3.34,3.35,3.24). We can put these equations in matrix form in different stages. In the compression stage we have

$$\begin{bmatrix} m & 0 & 0 & 0 & 0 & 0 & 1 & 0 & 0 \\ 0 & m & 0 & 0 & 0 & 0 & 0 & 1 & 0 \\ 0 & 0 & m & 0 & 0 & 0 & 0 & 0 & 1 \\ 0 & 0 & 0 & I_{xx} & -I_{xy} & -I_{xz} & 0 & -R_z & R_y \\ 0 & 0 & 0 & -I_{yx} & I_{yy} & -I_{yz} & R_z & 0 & -R_x \\ 0 & 0 & 0 & -I_{zx} & -I_{zy} & I_{zz} & -R_y & R_x & 0 \\ 1 & 0 & 0 & 0 & R_z & -R_y & 0 & 0 & 0 \\ 0 & 1 & 0 & -R_z & 0 & R_x & 0 & 0 & 0 \\ 0 & 0 & 1 & R_y & -R_x & 0 & 0 & 0 & 0 \end{bmatrix} \begin{bmatrix} V_x^c \\ V_y^c \\ V_z^c \\ \omega_x^c \\ \omega_y^c \\ \omega_z^c \\ \hat{F}_x^c \\ \hat{F}_y^c \\ \hat{F}_z^c \end{bmatrix} = \begin{bmatrix} mV_x \\ mV_y \\ mV_z \\ (I_{xx}\omega_x - I_{xy}\omega_y - I_{xz}\omega_z) \\ (-I_{yx}\omega_x + I_{yy}\omega_y - I_{yz}\omega_z) \\ (-I_{zx}\omega_x - I_{zy}\omega_y + I_{zz}\omega_z) \\ 0 \\ 0 \\ 0 \end{bmatrix} \quad (3.49)$$

The impulse relations in the restitution stage can be expressed as

$$\begin{bmatrix} m & 0 & 0 & 0 & 0 & 0 & 1 & 0 & 0 \\ 0 & m & 0 & 0 & 0 & 0 & 0 & 1 & 0 \\ 0 & 0 & m & 0 & 0 & 0 & 0 & 0 & 1 \\ 0 & 0 & 0 & I_{xx} & -I_{xy} & -I_{xz} & 0 & -R_z & R_y \\ 0 & 0 & 0 & -I_{yx} & I_{yy} & -I_{yz} & R_z & 0 & -R_x \\ 0 & 0 & 0 & -I_{zx} & -I_{zy} & I_{zz} & -R_y & R_x & 0 \\ 1 & 0 & 0 & 0 & R_z & -R_y & 0 & 0 & 0 \\ 0 & 0 & 0 & 0 & 0 & 0 & 0 & 1 & 0 \\ 0 & 0 & 1 & R_y & -R_x & 0 & 0 & 0 & 0 \end{bmatrix} \begin{bmatrix} V_x' \\ V_y' \\ V_z' \\ \omega_x' \\ \omega_y' \\ \omega_z' \\ \hat{F}_x' \\ \hat{F}_y' \\ \hat{F}_z' \end{bmatrix} = \begin{bmatrix} mV_x^c \\ mV_y^c \\ mV_z^c \\ (I_{xx}\omega_x^c - I_{xy}\omega_y^c - I_{xz}\omega_z^c) \\ (-I_{yx}\omega_x^c + I_{yy}\omega_y^c - I_{yz}\omega_z^c) \\ (-I_{zx}\omega_x^c - I_{zy}\omega_y^c + I_{zz}\omega_z^c) \\ 0 \\ \sqrt{2m \cdot e_n^2 \cdot (-W^c)} \\ 0 \end{bmatrix} \quad (3.50)$$

Sliding condition

The system of equations for three dimensional impacts in sliding mode are: Eqns. (3.10,3.11,3.12,3.19,3.20,3.21) and (3.40,3.41,3.24). We can put these equations in matrix form, too. In the compression stage we have

$$\begin{bmatrix} m & 0 & 0 & 0 & 0 & 0 & 1 & 0 & 0 \\ 0 & m & 0 & 0 & 0 & 0 & 0 & 1 & 0 \\ 0 & 0 & m & 0 & 0 & 0 & 0 & 0 & 1 \\ 0 & 0 & 0 & I_{xx} & -I_{xy} & -I_{xz} & 0 & -R_z & R_y \\ 0 & 0 & 0 & -I_{yx} & I_{yy} & -I_{yz} & R_z & 0 & -R_x \\ 0 & 0 & 0 & -I_{zx} & -I_{zy} & I_{zz} & -R_y & R_x & 0 \\ 0 & 0 & 0 & 0 & 0 & 0 & S_x & -\mu \cdot \sin(\phi) & 0 \\ 0 & 1 & 0 & -R_z & 0 & R_x & 0 & 0 & 0 \\ 0 & 0 & 0 & 0 & 0 & 0 & 0 & -\mu \cdot \cos(\phi) & S_z \end{bmatrix} \begin{bmatrix} V_x^c \\ V_y^c \\ V_z^c \\ \omega_x^c \\ \omega_y^c \\ \omega_z^c \\ \hat{F}_x^c \\ \hat{F}_y^c \\ \hat{F}_z^c \end{bmatrix} = \begin{bmatrix} mV_x \\ mV_y \\ mV_z \\ (I_{xx}\omega_x - I_{xy}\omega_y - I_{xz}\omega_z) \\ (-I_{yx}\omega_x + I_{yy}\omega_y - I_{yz}\omega_z) \\ (-I_{zx}\omega_x - I_{zy}\omega_y + I_{zz}\omega_z) \\ 0 \\ 0 \\ 0 \end{bmatrix} \quad (3.51)$$

In the restitution stage, the impulse equations are

$$\begin{bmatrix} m & 0 & 0 & 0 & 0 & 0 & 1 & 0 & 0 \\ 0 & m & 0 & 0 & 0 & 0 & 0 & 1 & 0 \\ 0 & 0 & m & 0 & 0 & 0 & 0 & 0 & 1 \\ 0 & 0 & 0 & I_{xx} & -I_{xy} & -I_{xz} & 0 & -R_z & R_y \\ 0 & 0 & 0 & -I_{yx} & I_{yy} & -I_{yz} & R_z & 0 & -R_x \\ 0 & 0 & 0 & -I_{zx} & -I_{zy} & I_{zz} & -R_y & R_x & 0 \\ 0 & 0 & 0 & 0 & 0 & 0 & S_x & -\mu \cdot \sin(\phi) & 0 \\ 0 & 0 & 0 & 0 & 0 & 0 & 0 & 1 & 0 \\ 0 & 0 & 0 & 0 & 0 & 0 & 0 & -\mu \cdot \cos(\phi) & S_z \end{bmatrix} \begin{bmatrix} V_x' \\ V_y' \\ V_z' \\ \omega_x' \\ \omega_y' \\ \omega_z' \\ \hat{F}_x' \\ \hat{F}_y' \\ \hat{F}_z' \end{bmatrix} = \begin{bmatrix} mV_x^c \\ mV_y^c \\ mV_z^c \\ (I_{xx}\omega_x^c - I_{xy}\omega_y^c - I_{xz}\omega_z^c) \\ (-I_{yx}\omega_x^c + I_{yy}\omega_y^c - I_{yz}\omega_z^c) \\ (-I_{zx}\omega_x^c - I_{zy}\omega_y^c + I_{zz}\omega_z^c) \\ 0 \\ \sqrt{2m \cdot e_n^2 \cdot (-W^c)} \\ 0 \end{bmatrix} \quad (3.52)$$

where

$$\mu = \frac{\mu_x}{\sin(\phi)} = \frac{\mu_z}{\cos(\phi)} \quad S_x = -\text{sign}(\vec{V}^C \cdot \vec{i}) \quad S_z = -\text{sign}(\vec{V}^C \cdot \vec{k}) \quad (3.53)$$

Numerical simulation results

Since a spherical ball is the simplest example in 3D simulation, only two modes, sliding and sticking, can happen during the impact as there is no reverse sliding for a 3-axis symmetric ball. These two modes can be developed into three cases #0, #1 and #3 based on Table (3.1) during impact.

As shown in Figure (3.8), the blue region belongs to sliding mode which means friction can not prevent the ball from sliding. The red region belongs to sliding in compression stage and sticking in restitution stage which means friction can stop the ball from sliding in the last stage. The light blue region belongs to sticking in both stages which means friction takes less time to stop the ball from sliding.

Energy dissipation is also a good quantity to investigate. As shown in Figure (3.9), the maximum energy dissipation happens when the ball travels along x direction with angular velocity $\omega_x = 0$. Also, sliding region has more energy dissipation than sticking region. This is the same conclusion we found in Chapter 2 two dimensional rigid-body impact.

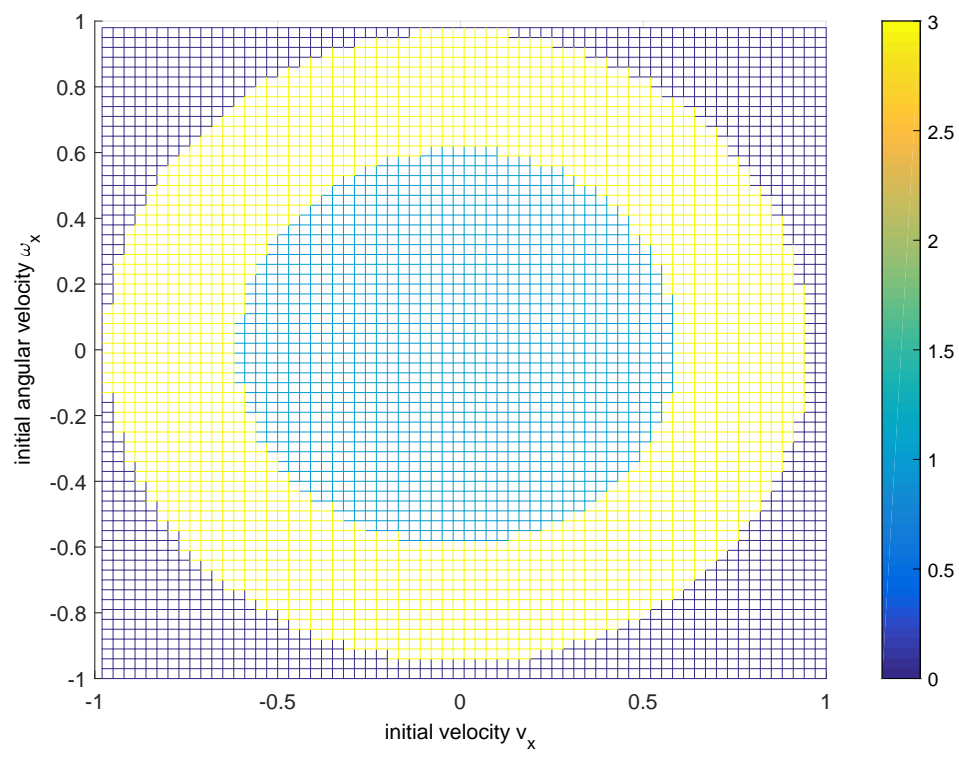


Figure 3.8: Three cases variation with initial parameters v_x , ω_x , μ and e_n

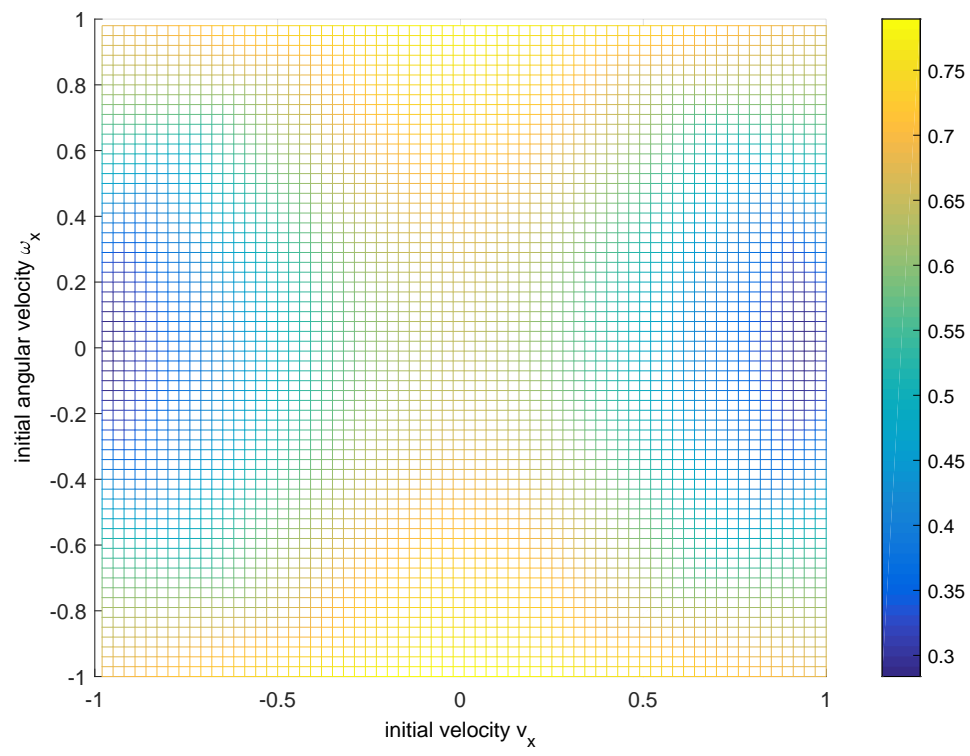


Figure 3.9: Energy dissipation with initial parameters v_x , ω_x , μ and e_n

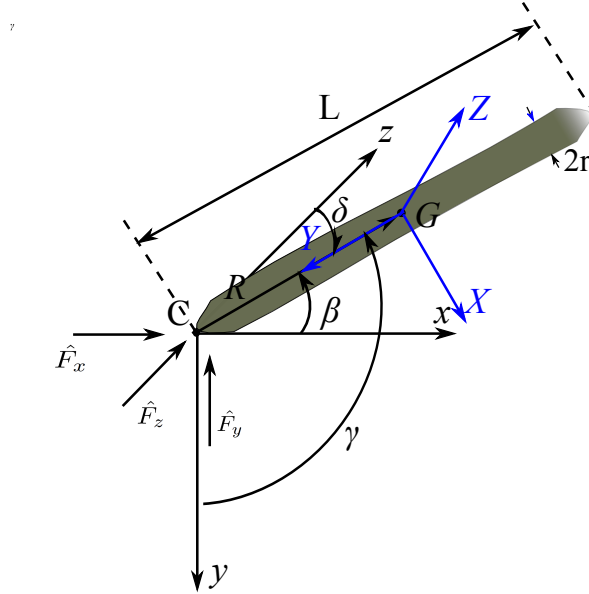


Figure 3.10: Falling rod colliding with ground in three dimensions

3.7.2 Impact of a Rod with the Ground

As an example of three-dimensional impact, we present the problem of a cylindrical rod in Figure (3.10). Both ends of the rod will be assumed to be spherical in order to model impact as point-to-line. Also, it is assumed the radius R between the contact point and the center of mass remain constant during impact.

Note that in the figure, the XYZ coordinate system is attached to the rod and the xyz coordinate system is inertial at the contact point C . This distinction will be required in calculating the inertia matrix from I_G to I'_G . The simulation problem becomes to determine the post-impact quantities $(v'_x, v'_y, v'_z, w'_x, w'_y, w'_z, P'_x, P'_y, P'_z)$. Let's start by assuming that the rod's mass m , length L , radius R and cap radius r are

$$m = 1 \quad L = 1 \quad R \approx \frac{L}{2} \quad r \approx \frac{L}{30} \quad (3.54)$$

and the angles between rod and xyz axes, initial velocity, and angular velocity are

$$0 \leq \beta \leq \pi \quad -\frac{\pi}{2} \leq \gamma \leq \frac{\pi}{2} \quad 0 \leq \delta \leq \pi \quad (3.55)$$

Also the coefficient of restitution and the friction coefficient μ which is assumed to be uniform along $x - z$ plane are

$$e_n = 0.3 \quad \mu = \frac{\mu_x}{\sin(\phi)} = \frac{\mu_z}{\cos(\phi)} = 0.5 \quad (3.56)$$

in which ϕ , mentioned in section 3.4, is the angle between frictional forces F_x and F_z .

The position vector between the contact point C and the center of mass G become

$$R_x = R \cos(\beta) \quad R_y = R \cos(\gamma) \quad R_z = R \cos(\delta) \quad (3.57)$$

The inertia matrix $[I_G]$ for a $x - y - z$ axis symmetric cylindrical rod on body attached frame is

$$[I_G^{XYZ}] = \begin{bmatrix} I_{XX} & 0 & 0 \\ 0 & I_{YY} & 0 \\ 0 & 0 & I_{ZZ} \end{bmatrix} \quad (3.58)$$

Substituting Eqn. (3.54) into Eqn. (3.58), we get

$$[I_G^{XYZ}] = \begin{bmatrix} \frac{1}{4}r^2 + \frac{1}{12}L^2 & 0 & 0 \\ 0 & \frac{1}{2}r^2 & 0 \\ 0 & 0 & \frac{1}{4}r^2 + \frac{1}{12}L^2 \end{bmatrix} \quad (3.59)$$

In figure (3.10), Since the spherical caps on the ends of the rod are relatively small, we are neglect their contribution to the inertia properties of the rod. Recall section 3.3, a inertia matrix on any frame can be attained by 3 rotations followed by three Euler angles $\theta_1 - \theta_2 - \theta_3$. Using Eqns. (3.27) and (4.17), the rotation matrix on reference

xyz frame is therefore

$$[I_G^{xyz}] = [Q]^T [I_G^{XYZ}] [Q] \quad (3.60)$$

$$[I_G^{xyz}] = [Q]^T \begin{bmatrix} \frac{1}{4}r^2 + \frac{1}{12}L^2 & 0 & 0 \\ 0 & \frac{1}{2}r^2 & 0 \\ 0 & 0 & \frac{1}{4}r^2 + \frac{1}{12}L^2 \end{bmatrix} [Q] = \begin{bmatrix} I_{xx} & -I_{xy} & -I_{xz} \\ -I_{yx} & I_{yy} & -I_{yz} \\ -I_{zx} & -I_{zy} & I_{zz} \end{bmatrix} \quad (3.61)$$

As deriving equations in matrix form for a ball, all different modes have the same six equations (3.10,3.11,3.12,3.19,3.20,3.21). Last three equations are conditions depended on different modes.

Sticking Mode

Conditions in compression stage are

$$V_{cx}^c = V_x^c + R_z \omega_y^c - R_y \omega_z^c = 0 \quad (3.62)$$

$$V_{cy}^c = V_y^c - R_z \omega_x^c + R_x \omega_z^c = 0 \quad (3.63)$$

$$V_{cz}^c = V_z^c + R_y \omega_x^c - R_x \omega_y^c = 0 \quad (3.64)$$

And conditions in restitution stage can be expressed as

$$V_{cx}' = V_x' + R_z \omega_y' - R_y \omega_z' = 0 \quad (3.65)$$

$$\hat{F}_y' = \sqrt{2m \cdot e_n^2 \cdot (-W^c)} \quad (3.66)$$

$$V'_{cz} = V'_z + R_y \omega'_x - R_x \omega'_y = 0 \quad (3.67)$$

Sliding Mode

Conditions in compression stage are

$$S_x \hat{F}_x^c - \mu \hat{F}_y^c \cdot \sin(\phi) = 0 \quad (3.68)$$

$$V_{cy}^c = V_y^c - R_z \omega_x^c + R_x \omega_z^c = 0 \quad (3.69)$$

$$S_z \hat{F}_z^c - \mu \hat{F}_y^c \cdot \cos(\phi) = 0 \quad (3.70)$$

And conditions in restitution stage can be expressed as

$$S_x \hat{F}_x' - \mu \hat{F}_y' \cdot \sin(\phi) = 0 \quad (3.71)$$

$$\hat{F}_y' = \sqrt{2m \cdot e_n^2 \cdot (-W^c)} \quad (3.72)$$

$$S_z \hat{F}_z' - \mu \hat{F}_y' \cdot \cos(\phi) = 0 \quad (3.73)$$

where

$$\mu = \frac{\mu_x}{\sin(\phi)} = \frac{\mu_z}{\cos(\phi)} \quad S_x = -\text{sign}(V_{cx}) \quad S_z = -\text{sign}(V_{cz}) \quad (3.74)$$

Reverse Sliding Mode

As we assume that the cylindrical rod begins with sliding, it may change to reverse sliding in compression or restitution stage. Let's assume that the rod goes to reverse sliding mode in compression stage as an example. The second condition depends on

the initial conditions of v_{cx} and v_{cz} . If $v_{cx} > v_{cz}$, we will use Eqn. (3.34) as last equation. Otherwise, we will use Eqn. (3.35) as our last equation. For instance, we assume $v_{cx} > v_{cz}$ and the conditions in compression stage for sliding at the beginning are

$$S_x \hat{F}_x^{c1} - \mu \hat{F}_y^{c1} \cdot \sin(\phi) = 0 \quad (3.75)$$

$$V_{cx}^{c1} = V_x^{c1} + R_z \omega_y^{c1} - R_y \omega_z^{c1} = 0 \quad (3.76)$$

$$S_z \hat{F}_z^{c1} - \mu \hat{F}_y^{c1} \cdot \cos(\phi) = 0 \quad (3.77)$$

where

$$\mu = \frac{\mu_x}{\sin(\phi)} = \frac{\mu_z}{\cos(\phi)} \quad S_x = -\text{sign}(\vec{V}_{cx}) \quad S_z = -\text{sign}(\vec{V}_{cz}) \quad (3.78)$$

During the transition, the sliding mode changes to reverse sliding and the impulsive force direction changes. This situation can lead to three possibilities 2(a), 2(b) and 2(c) shown in Table (3.1). Each possibility can result in direction change of the impulsive force. Figure (3.11) shows a procedure of determining whether sliding or reverse sliding occurs. With the updated sign of impulsive force in friction plane, the reverse sliding matrix is

$$S_x \hat{F}_x^{c2} - \mu \hat{F}_y^{c2} \cdot \sin(\phi) = 0 \quad (3.79)$$

$$V_{cy}^{c2} = V_y^{c2} - R_z \omega_x^{c2} + R_x \omega_z^{c2} = 0 \quad (3.80)$$

$$S_z \hat{F}_z^{c2} - \mu \hat{F}_y^{c2} \cdot \cos(\phi) = 0 \quad (3.81)$$

where

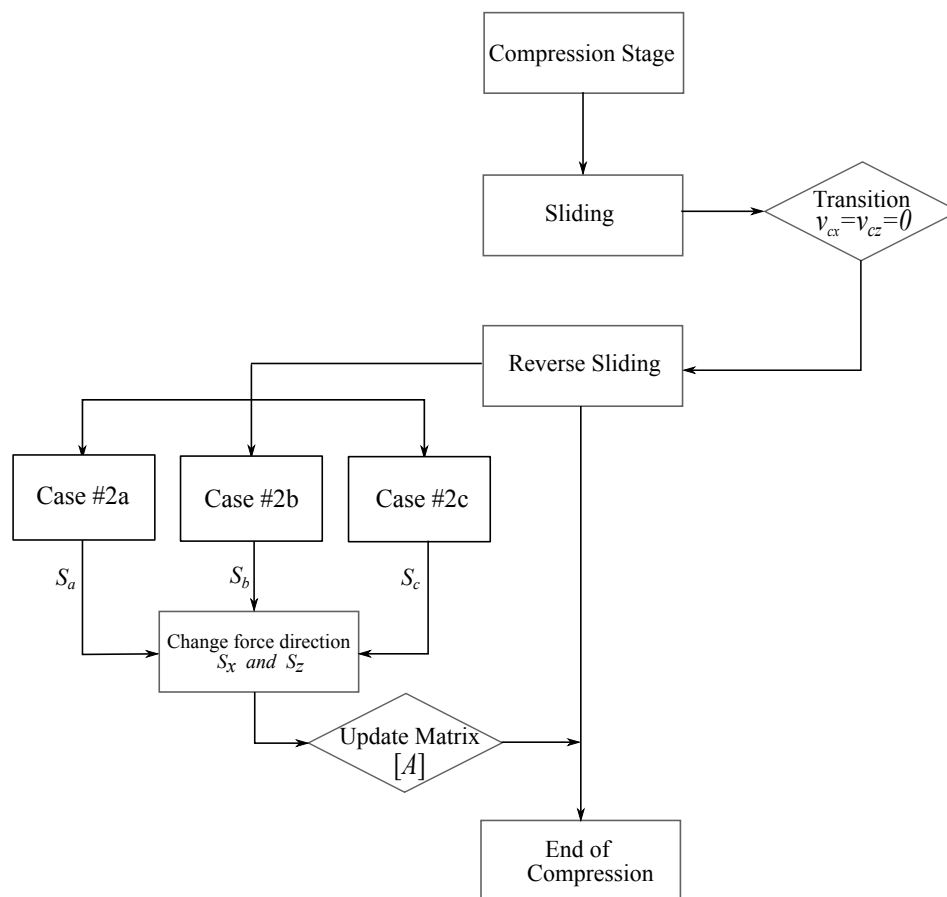


Figure 3.11: Flow Chart for Reverse Sliding in Compression

$$\mu = \frac{\mu_x}{\sin(\phi)} = \frac{\mu_z}{\cos(\phi)} \quad S_x = -S_x \quad S_z = -S_z \quad (3.82)$$

In the restitution stage, the object remains in reverse sliding mode and conditions can be expressed as

$$S_x \hat{F}_x^r - \mu \hat{F}_y^r \cdot \sin(\phi) = 0 \quad (3.83)$$

$$\hat{F}_y' = \sqrt{2m \cdot e_n^2 \cdot (-W^c)} \quad (3.84)$$

$$S_z \hat{F}_z^r - \mu \hat{F}_y^r \cdot \cos(\phi) = 0 \quad (3.85)$$

Numerical Simulation Results

Since three modes, sliding, sticking and reverse sliding, could happen in the compression or restitution stage during the impact depending on the initial conditions. There are 11 cases in Table (3.1).

Influence of μ and e_n on cases and the energy dissipation $K_{dissipation}$ It is known that there is no energy loss when $\mu = 0$ and $e_n = 0$. In contrast, the most energy dissipates when $\mu = 1$ and $e_n = 1$.

Example 1 shown in Fig (3.12) indicates that if there is no frictional force, the angular impulse-momentum change the rod from sliding to reverse sliding in different stages. As v_x increases from -2 to -1.5 , case of motion 0 indicates that the rod remains in sliding mode during impact changes from sliding to sticking in different stages. As v_x increases from -1.5 to -0.7 , the case of motion is $4b$ indicating that the rod turns into reverse sliding mode in restitution stage. When v_x increases from -0.7 to -0.05 , case of motion is $2b$ indicating that the rod turns to reverse sliding mode in an earlier stage, compression stage. When v_x equals to 0, the rod starts with reverse sliding mode at the beginning of compression stage. The initial conditions are

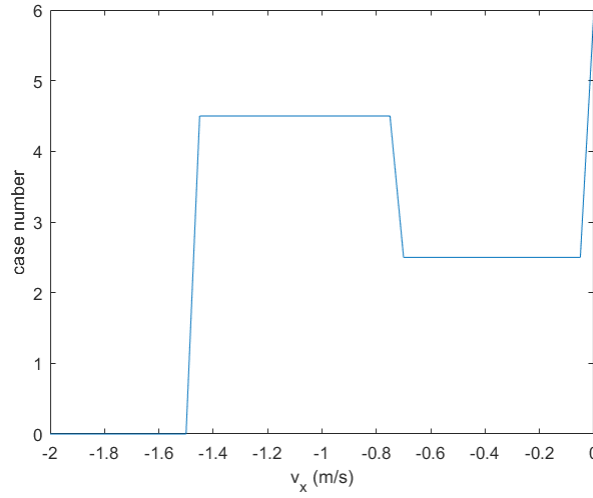


Figure 3.12: Example 1: Influence of initial velocity v_x on cases of impact with $\mu = 0$, $e_n = 1$, $v_x = -2 : 0.05 : 0$

$$\beta = \frac{2\pi}{3} \quad \gamma = \frac{5\pi}{6} \quad \delta = \frac{\pi}{2} \quad (3.86)$$

$$\theta_1 = \theta_2 = 0 \quad \theta_3 = \frac{\pi}{6} \quad (3.87)$$

$$\mu = 0 \quad e_n = 1 \quad (3.88)$$

$$\omega_x = \omega_y = \omega_z = 0 \quad (3.89)$$

$$v_x = -2 : 0.05 : 0 \quad v_y = 1 \quad v_z = 0 \quad (3.90)$$

Example 2 shown in Fig (3.13) indicates that in the presence of a frictional force, the motion of the tip of the rod changes from sliding to sticking in different stages. As v_x increases from -2 to -1.55 , the motion is case 3 indicating that the rod changes from sliding to sticking mode in the restitution stage. When v_x increases from -1.55 to -0.05 , case 1 motion indicates that the rod changes from sliding to sticking mode in

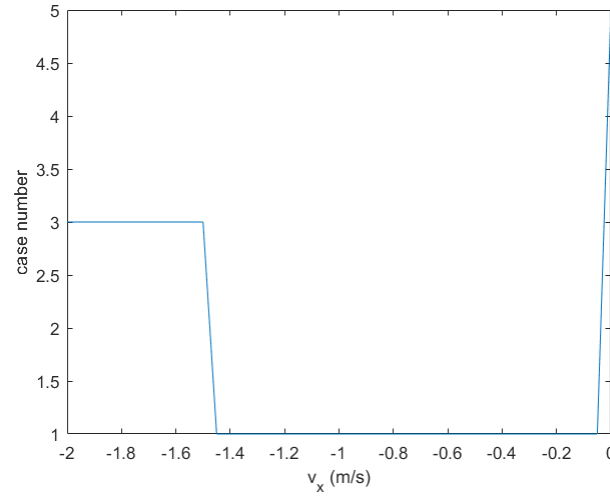


Figure 3.13: Example 2: Influence of initial velocity v_x on cases of impact with $\mu = 1$, $e_n = 1$, $v_x = -2 : 0.05 : 0$

restitution in an earlier stage, compression stage. When v_x equals to 0, the rod starts with sticking mode at the beginning of the compression stage. The initial conditions are

$$\beta = \frac{\pi}{3} \quad \gamma = \frac{7\pi}{6} \quad \delta = \frac{\pi}{2} \quad (3.91)$$

$$\theta_1 = \theta_2 = 0 \quad \theta_3 = -\frac{\pi}{6} \quad (3.92)$$

$$\mu = 1 \quad e_n = 1 \quad (3.93)$$

$$\omega_x = \omega_y = \omega_z = 0 \quad (3.94)$$

$$v_x = -2 : 0.05 : 0 \quad v_y = 1 \quad v_z = 0 \quad (3.95)$$

Examples 3A, 3B and 3C, shown in Fig (3.14), show the influence of μ and e_n on cases, energy dissipation $K_{dissipation}$ and post-impact velocity v'_x . In examples 3A and

3C, $K_{dissipation}$ and v'_x have the same trend while μ and e_n change from 0 to 1. In example 3A and 3B, as μ increases from 0 to 1, the case of motion changes from 1 (sticking in compression) to 2b (reverse sliding in compression) and 2b to 4b (reverse sliding in restitution) and 4b back to 0 (sliding in both stages). However, the energy doesn't dissipate much. As e_n increases from 0 to 1, the case describing the motion doesn't change, but the energy dissipation has a greater variation from 0 to 0.3 and becomes 0 when $\mu = 0$ and $e_n = 1$. The initial conditions are

$$\beta = \frac{2\pi}{3} \quad \gamma = \frac{5\pi}{6} \quad \delta = \frac{\pi}{2} \quad (3.96)$$

$$\theta_1 = \theta_2 = 0 \quad \theta_3 = -\frac{\pi}{6} \quad (3.97)$$

$$\mu = 0 : 0.025 : 1 \quad e_n = 0 : 0.025 : 1 \quad (3.98)$$

$$\omega_x = \omega_y = \omega_z = 0 \quad (3.99)$$

$$v_x = -1 \quad v_y = 1 \quad v_z = 0 \quad (3.100)$$

Examples 4A, 4B and 4C, shown in Fig (3.15), show the influence of μ and e_n on the different cases, energy dissipation $K_{dissipation}$, and post-impact velocity v'_x , while initial velocity v_x is in opposite direction to examples 3A, 3B and 3C. In examples 4A and 4C, $K_{dissipation}$ and v'_x have the opposite trend while μ and e_n change from 0 to 1. In example 4A and 4B, as μ increases from 0 to 1, the case of motion changes from 1 (sticking in compression) to 3 (sticking in restitution) and 3 to 0 (sliding in both stages), and the energy dissipation varies a lot. As e_n increases from 0 to 1, case of motion doesn't change, and the energy dissipation varies a little. Energy dissipation becomes 0 when $\mu = 0$ and $e_n = 1$. The initial conditions are

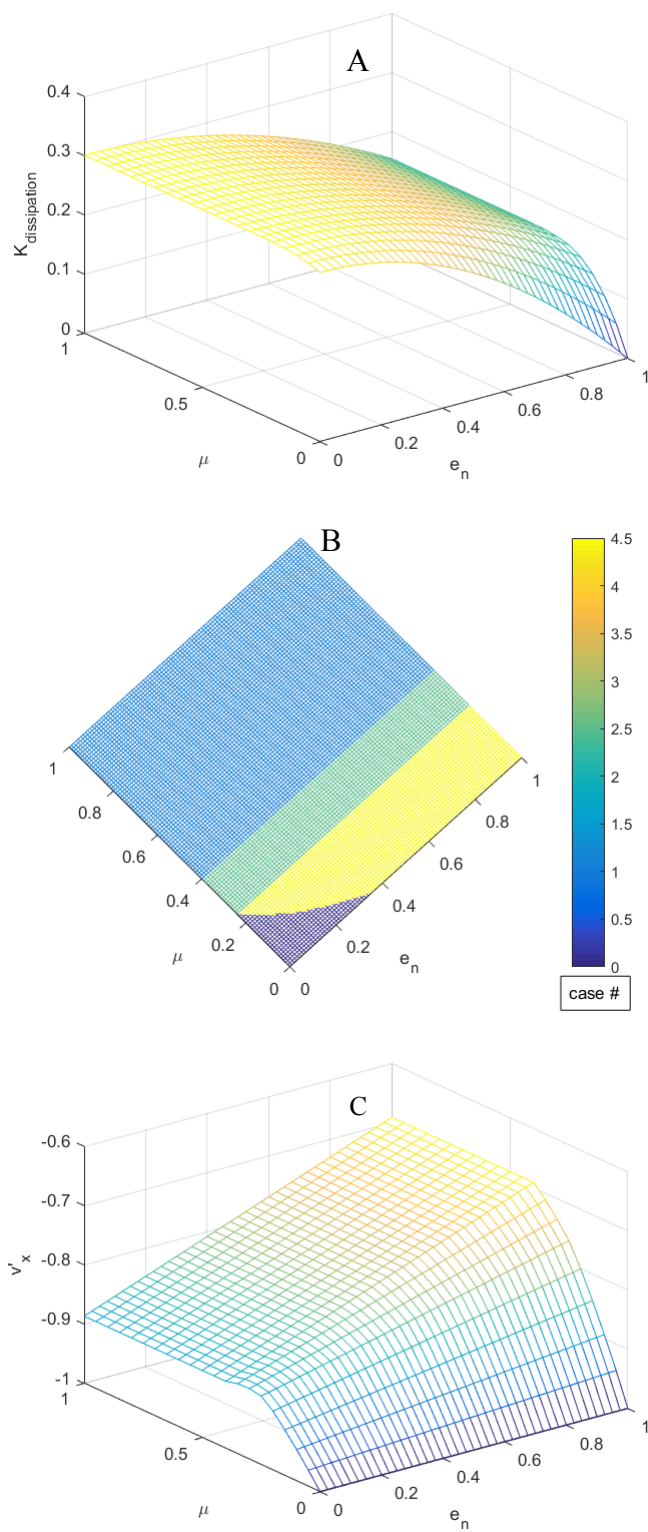


Figure 3.14: Examples 3: Influence of μ and e_n on (A) cases of impact, (B) energy dissipation $K_{dissipation}$, (C) post-impact velocity v'_x

$$\beta = \frac{2\pi}{3} \quad \gamma = \frac{5\pi}{6} \quad \delta = \frac{\pi}{2} \quad (3.101)$$

$$\theta_1 = \theta_2 = 0 \quad \theta_3 = -\frac{\pi}{6} \quad (3.102)$$

$$\mu = 0 : 0.025 : 1 \quad e_n = 0 : 0.025 : 1 \quad (3.103)$$

$$\omega_x = \omega_y = \omega_z = 0 \quad (3.104)$$

$$v_x = 1 \quad v_y = 1 \quad v_z = 0 \quad (3.105)$$

These examples show that e_n has a larger effect than μ on energy loss in reverse sliding mode, while μ influences energy loss more than e_n does in a sliding mode. This is the same as the conclusion we reached in two-dimensional impact modeling.

Influence of orientation angles β and γ on cases and the energy dissipation $K_{dissipation}$ When the rod's position is kept in the $x - y$ plane and rotated from 0 to π , the influence of orientation angles β and γ on cases study and energy dissipation $K_{dissipation}$ is shown in Fig (3.16). As β increases from 0 to 0.7 *radians*, the case of motion changes from 0 (sliding during both stages) to 4c (reverse sliding in restitution). As β increases from 0.7 to 0.95, the case of motion changes from 4c to 2c (reverse sliding in compression). As β increases from 0.95 to 1.04, the case of motion changes from 2c to 1 (sticking in compression). As β increases from 1.04 to 1.79, the case of motion changes from 1 to 3 (sticking in restitution). As β increases from 1.79 to 1.87, the case of motion changes from 3 back to 0. From the figure of β vs $K_{dissipation}$, the most energy dissipation is 0.7119 when β is equal to 1.95 and the rod is in sliding regime. This is the same as the conclusion we had in two-dimensional modeling. The initial conditions are

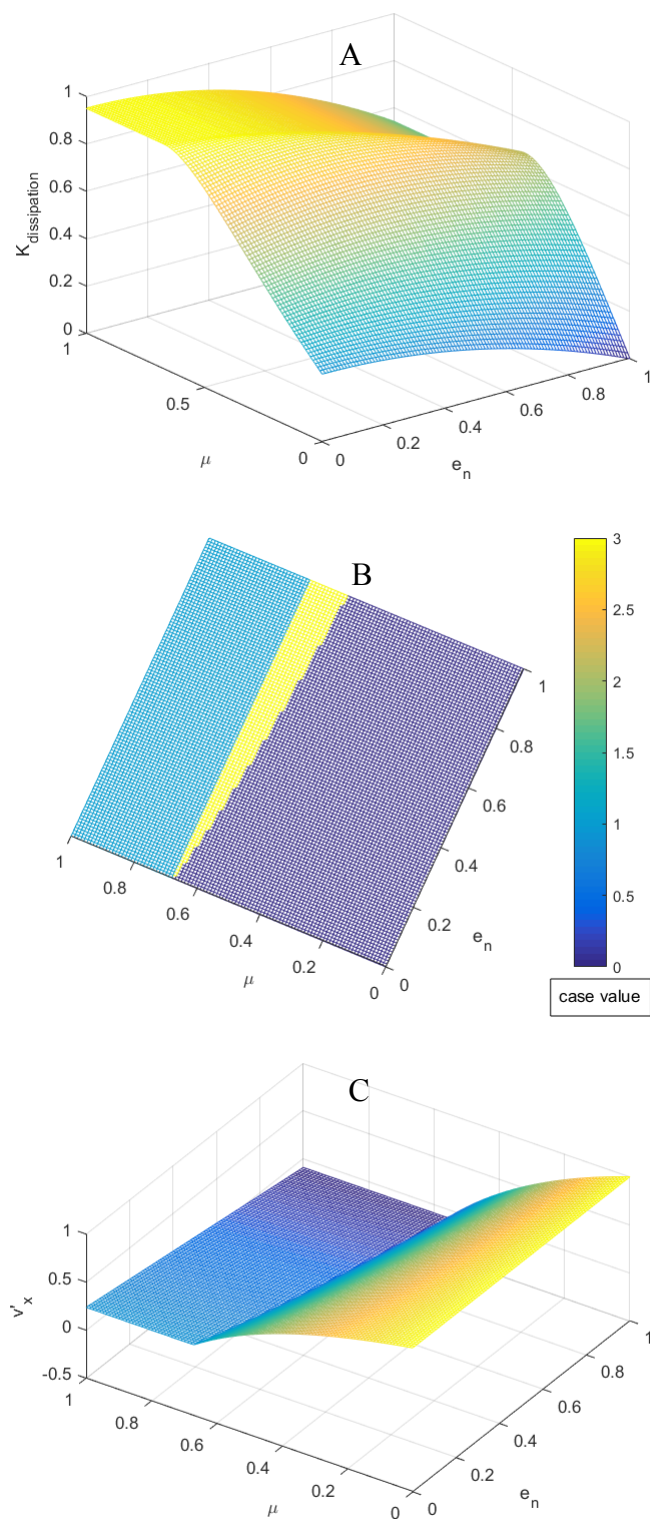


Figure 3.15: Examples 4: Influence of μ and e_n on (A) cases of impact, (B) energy dissipation $K_{dissipation}$, (C) post-impact velocity v'_x

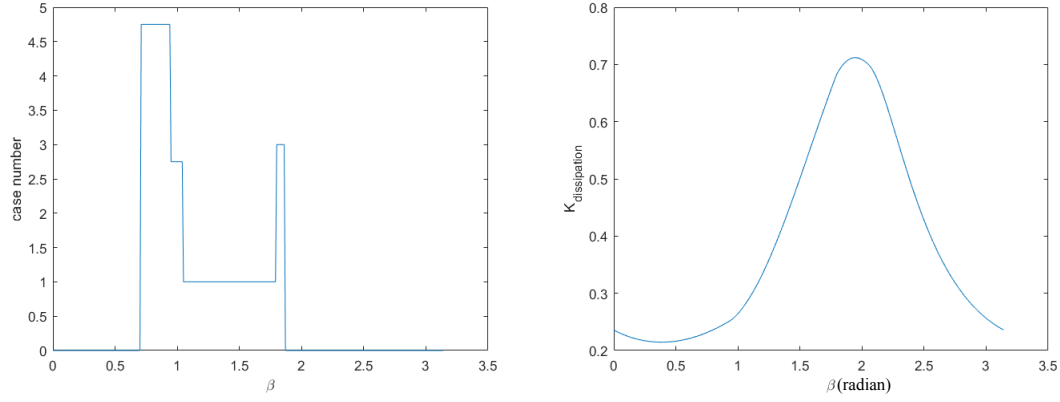


Figure 3.16: Influence of orientation angle β on energy dissipation $K_{dissipation}$ and cases of impact with $\mu = 0.4$, $e_n = 0.4$

$$\beta = 0 : 0.01 : \pi \quad \gamma = \frac{3\pi}{2} - \beta \quad \delta = \frac{\pi}{2} \quad (3.106)$$

$$\theta_1 = \theta_2 = 0 \quad \theta_3 = \frac{\pi}{2} - \beta \quad (3.107)$$

$$\mu = 0.4 \quad e_n = 0.4 \quad (3.108)$$

$$\omega_x = \omega_y = \omega_z = 0 \quad (3.109)$$

$$v_x = 1 \quad v_y = 1 \quad v_z = 0 \quad (3.110)$$

Influence of β and μ on cases and the energy dissipation $K_{dissipation}$

The influence of orientation angles β and coefficient of friction μ on cases study and energy dissipation $K_{dissipation}$ is shown in Fig (3.17). As β and μ vary, the rod changes between sliding, sticking and reverse sliding modes during both stages. Along the y (μ) axis direction, sliding or reverse sliding trends to change to sticking mode as μ increases. Along the x (β) axis direction, there are reverse sliding regimes when β is less than $\frac{\pi}{2}$ since the angular impulse-momentum in x direction component is opposite to frictional

impulsive force. More sliding regimes exist when β is larger than $\frac{\pi}{2}$ since the angular impulse-momentum in x direction component and frictional impulsive force are in the same direction.

From the energy dissipation figure on Fig (3.17), β has more influence on $K_{dissipation}$ than μ does. The largest amount energy dissipation occurs in the regime between reverse sliding and sliding when $\mu = 0.95$ and $\beta = 2.42 \text{ radians}$. The initial conditions are

$$\beta = 0 : 0.01 : \pi \quad \gamma = \frac{3\pi}{2} - \beta \quad \delta = \frac{\pi}{2} \quad (3.111)$$

$$\theta_1 = \theta_2 = 0 \quad \theta_3 = \frac{\pi}{2} - \beta \quad (3.112)$$

$$\mu = 0 : 0.01 : 1 \quad e_n = 0.4 \quad (3.113)$$

$$\omega_x = \omega_y = \omega_z = 0 \quad (3.114)$$

$$v_x = 1 \quad v_y = 1 \quad v_z = 0 \quad (3.115)$$

Influence of β and e_n on cases and the engergy dissipation $K_{dissipation}$

The influence of orientation angles β and coefficient of restitution e_n on cases study and engergy dissipation $K_{dissipation}$ is shown in Fig (3.18). As β decreases from 2.5 to 2.2 *radians*, the case of motion changes from 0 (sliding during both stages) to 4b (reverse sliding in restitution). As β decreases from 2.2 to 1.8, the case of motion changes from 4c to 3 (sticking in restitution). As β decreases from 1.8 to 0.9, the case of motion changes from 3 to 1 (sticking in compression). As β decreases from 0.9 to 0, the case of motion changes from 1 back to 0. The largest amount energy dissipation occurs in the regime between sticking and sliding when β is between 2.2 and 1.8 and e_n is between 0 and 0.4. and the rod is in sliding regime. Along the x (e_n) axis direction, the influence of e_n on modes is very small. Cases of motions 1 and 3 stay the same as e_n increases

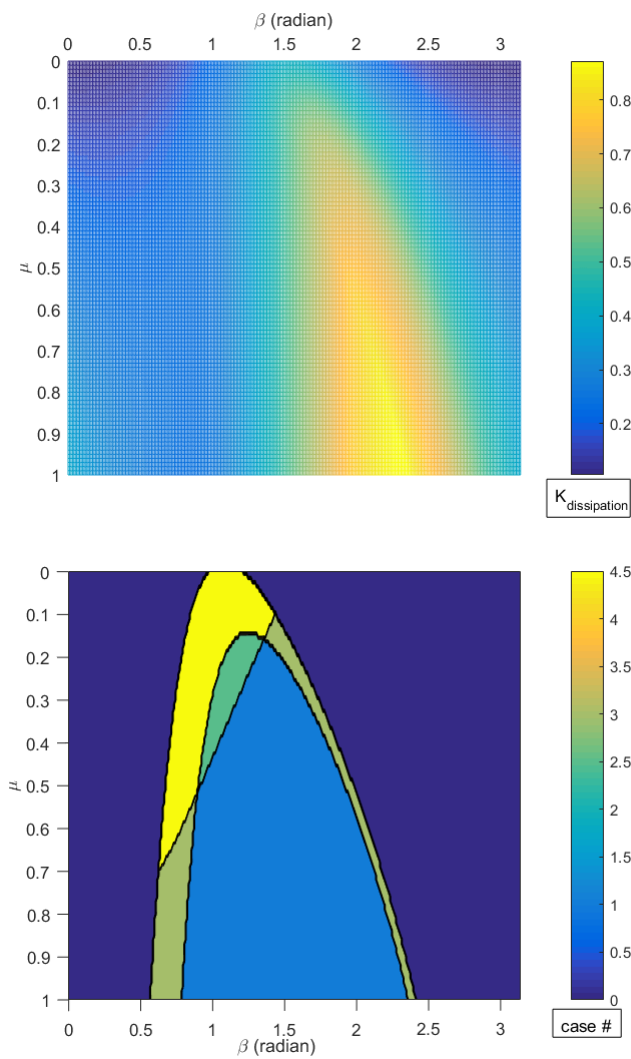


Figure 3.17: Influence of orientation angle β and coefficient of friction μ on energy dissipation $K_{dissipation}$ and cases of impact with $e_n = 0.4$

from 0 to 1. So β has more influence on cases than e_n does.

From the energy dissipation figure on Fig (3.18), the energy dissipation changes greatly along the x (e_n) axis direction compare to the y (β) axis direction. The largest amount energy dissipation occurs in the regime between sticking and sliding when β is between 2.2 and 1.8 and e_n is between 0 and 0.4. Overall, e_n has more influence on $K_{dissipation}$ than β does. The initial conditions are

$$\beta = 0 : 0.01 : \pi \quad \gamma = \frac{3\pi}{2} - \beta \quad \delta = \frac{\pi}{2} \quad (3.116)$$

$$\theta_1 = \theta_2 = 0 \quad \theta_3 = \frac{\pi}{2} - \beta \quad (3.117)$$

$$\mu = 0.4 \quad e_n = 0 : 0.01 : 1 \quad (3.118)$$

$$\omega_x = \omega_y = \omega_z = 0 \quad (3.119)$$

$$v_x = 1 \quad v_y = 1 \quad v_z = 0 \quad (3.120)$$

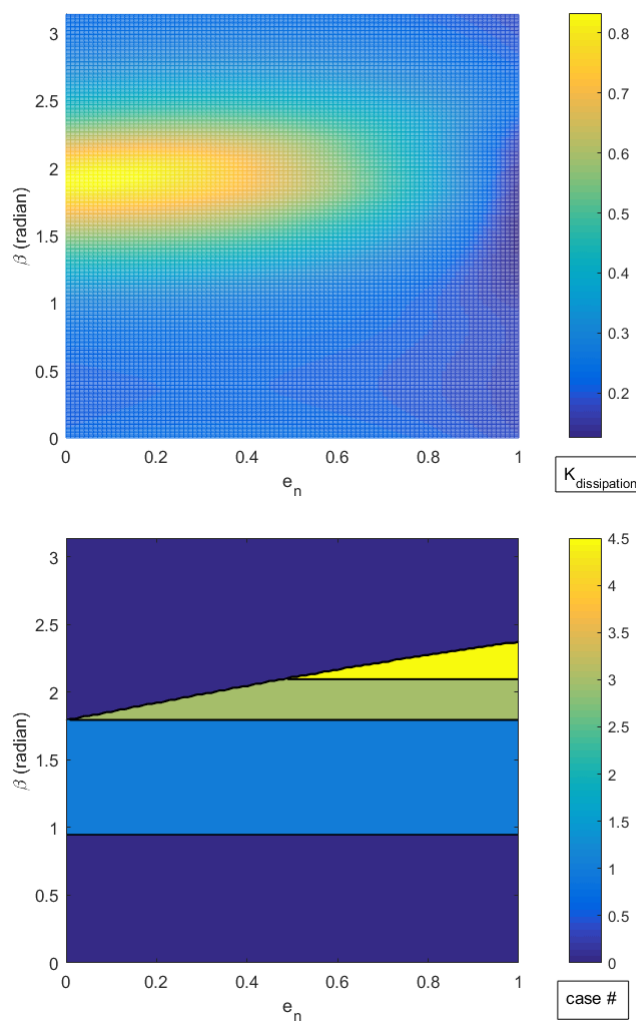


Figure 3.18: Influence of orientation angle β and coefficient of restitution e_n on energy dissipation $K_{dissipation}$ and cases of impact with $\mu = 0.4$

Comparison of Different Friction Coefficient Models (μ_k and μ_s) The previous simulation results are based on the assumption that kinetic coefficient of friction μ_k and static coefficient of friction μ_s have the same value. Different values of μ_k and μ_s can be another factor affecting the results. Considering that μ_k changes to μ_s while the object is in the transition sticking mode while turning from sliding to reverse sliding, or from initially sticking to reverse sliding mode discussed in chapter 2, cases and energy dissipation can be different.

Fig (3.19) shows the comparison of $\mu_s = 1.2 * \mu_k$ (on the top) and $\mu_s = \mu_k$ (on the bottom) models on cases study, post-impact velocity and engergy dissipation $K_{dissipation}$. The $\mu_s = 1.2 * \mu_k$ model has a larger sticking regime than $\mu_s = \mu_k$ model does. This difference results in different post-impact velocities. It turns out that there is no obvious difference in energy dissipation.

The initial conditions are

$$\beta = 0 : 0.01 : \pi \quad \gamma = \frac{3\pi}{2} - \beta \quad \delta = \frac{\pi}{2} \quad (3.121)$$

$$\theta_1 = \theta_2 = 0 \quad \theta_3 = \frac{\pi}{2} - \beta \quad (3.122)$$

$$\mu_k = \frac{\mu_s}{1.2} = 0 : 0.01 : 1 \quad e_n = 0.4 \quad (3.123)$$

$$\omega_x = \omega_y = \omega_z = 0 \quad (3.124)$$

$$v_x = 1 \quad v_y = 1 \quad v_z = 0 \quad (3.125)$$

3.7.3 Impact of a Rectangular Bar with the Ground

For the rod example, the mass moment of inertia along its length is negligible and we only focus on analyzing its velocity and two directions angular velocity. In order to analysis a rigid-body impact motion with six dynamic quantities, v_x , v_y , v_z , ω_x ,

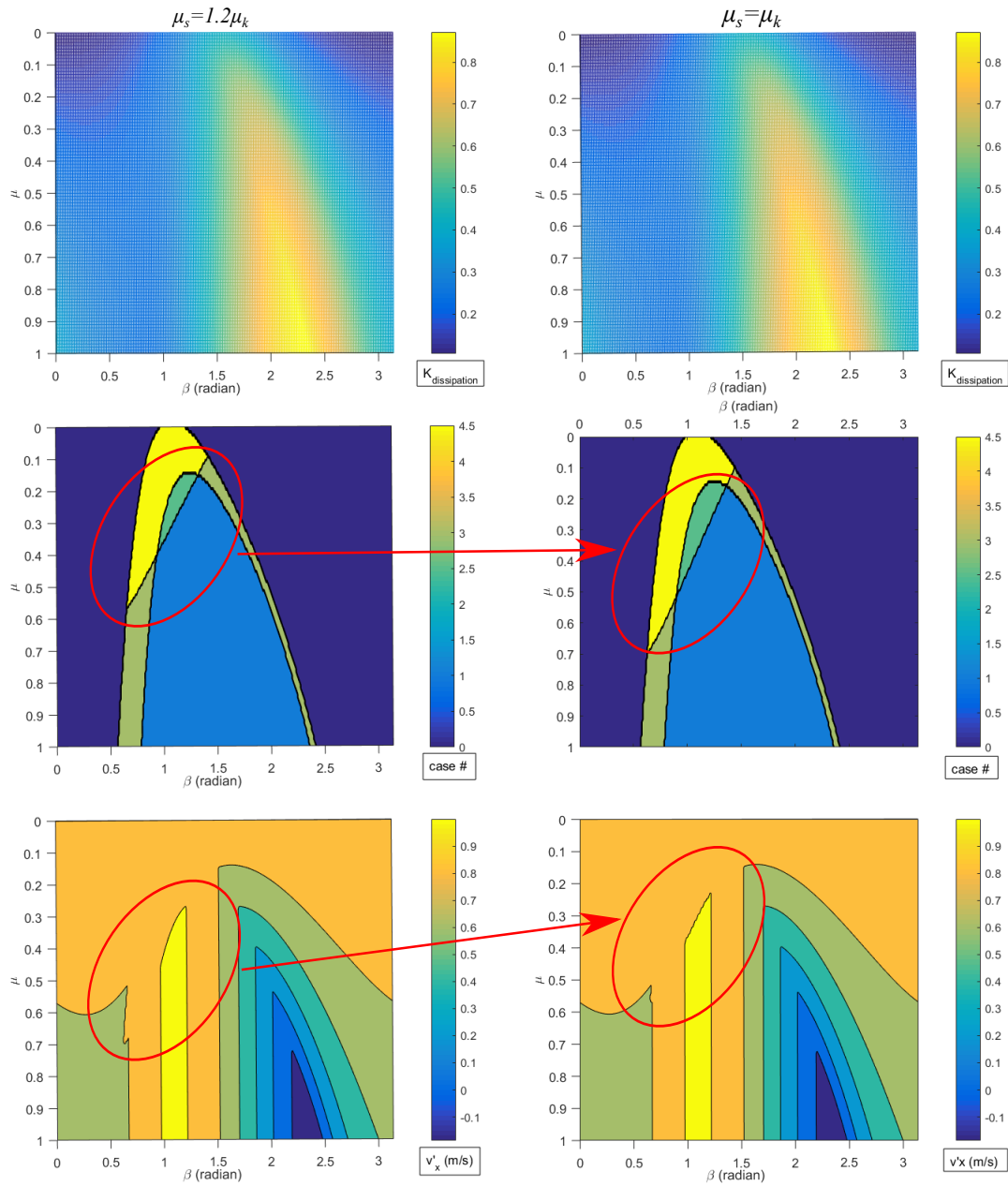


Figure 3.19: Comparison of μ_k and μ_s models on energy dissipation $K_{dissipation}$, post impact velocity v'_x and cases with $e_n = 0.4$

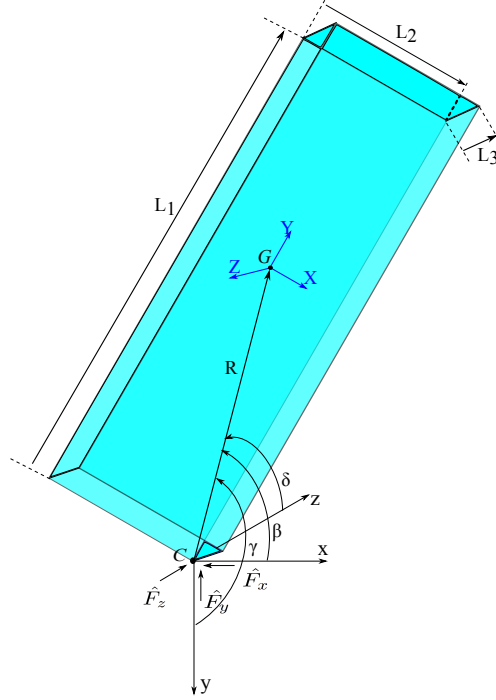


Figure 3.20: Falling bar colliding with ground in three dimensions

ω_y , ω_z and investigate the frictional force behavior on the friction plane, we analyze the three dimensional impact of a rectangular bar in this subsection. The bar will impact the surface with different initial velocities and angular velocities throughout our simulations. The solution will be obtained by following same procedure outlined in previous subsections.

We begin our analysis by defining the dimensions and orientation of the bar. The lengths of the bar along the (X, Y, Z) axis are (L_1, L_2, L_3) , respectively. Figure (3.20) shows the bar, where the XYZ coordinate system is attached to the bar and the xyz coordinate system, the reference coordinate, is at the contact point C such that the y axis is normal to the impact plane (x, z) .

The distance from the contact point to the center of gravity, R is

$$R = \frac{\sqrt{L_1^2 + L_2^2 + L_3^2}}{2} \quad (3.126)$$

And the components of \vec{R} can be easily attained from the orientation angles as

$$R_x = R \cos(\beta) \quad R_y = R \cos(\gamma) \quad R_z = R \cos(\delta) \quad (3.127)$$

The mass moment of inertia matrix for the bar in its principal XYZ coordinate is

$$[I_G] = \begin{bmatrix} I_{XX} & 0 & 0 \\ 0 & I_{YY} & 0 \\ 0 & 0 & I_{ZZ} \end{bmatrix} \quad (3.128)$$

where

$$I_{XX} = \frac{m}{12}(L_2^2 + L_3^2) \quad (3.129)$$

$$I_{YY} = \frac{m}{12}(L_1^2 + L_3^2) \quad (3.130)$$

$$I_{ZZ} = \frac{m}{12}(L_1^2 + L_2^2) \quad (3.131)$$

To express the inertia matrix in reference xyz coordinate, we make the coordinate transformation matrix $[Q]$ that relates the xyz and XYZ coordinates. Substituting Eqn. (3.128) into Eqn. (3.27), we get

$$[I_G^{xyz}] = [Q]^T \begin{bmatrix} \frac{m}{12}(L_2^2 + L_3^2) & 0 & 0 \\ 0 & \frac{m}{12}(L_1^2 + L_3^2) & 0 \\ 0 & 0 & \frac{m}{12}(L_1^2 + L_2^2) \end{bmatrix} [Q] \quad (3.132)$$

Sliding, sticking and reverse sliding modes

Since we have already developed different Eqns. (68-75) for different modes in the example of rod, we can use the same conditions for the bar.

Numerical simulation results

In the previous analysis of impact on a rod, conditions when frictional force and gravitational force along x direction component are in a same line were studied. In this section, a numerical simulation study on the influence of frictional force and the component of gravitational force on x -axis which are not in the same line but in a tangential $x - z$ plane is presented. The initial conditions are selected as

$$\beta = \frac{2\pi}{3} \quad \gamma = \frac{5\pi}{6} \quad \delta = \frac{\pi}{2} \quad (3.133)$$

$$\theta_1 = \theta_2 = 0 \quad \theta_3 = -\frac{\pi}{6} \quad (3.134)$$

$$\mu = 0.6 \quad e_n = 0.4 \quad (3.135)$$

$$\omega_x = \omega_y = \omega_z = 0 \quad (3.136)$$

$$v_x = -1 : 0.03 : 1 \quad v_y = 1 \quad v_z = -1 : 0.03 : 1 \quad (3.137)$$

Influence of initial velocity v_x and v_z on cases study and engergy dissipation $K_{dissipation}$ Fig (3.21) shows the influence of frictional force in tangential $x - z$ plane on cases and engergy dissipation $K_{dissipation}$. Cases of motion on the left of the figure indicates that the case of motion is symmetric between $v_z = -1$ to 0 and 1 to 0 along the x (v_z) axis due to the fact that only frictional force acting on this direction which only depends on the sign of v_z . However, the case of motion is asymmetric along the y (v_x) axis since frictional force and gravitational force are both acting on this axis with same direction between 1 to 0 and opposite direction between -1 to 0. As v_x decreases from 1 to 0 and v_z decreases from 0 to -1 or increases from 0 to 1, the case of the motion changes from 3 (sticking in restitution) or 1 (sticking in restitution) to 4b (reverse sliding in restitution) or 2b (reverse sliding in compression) and then 0 (sliding

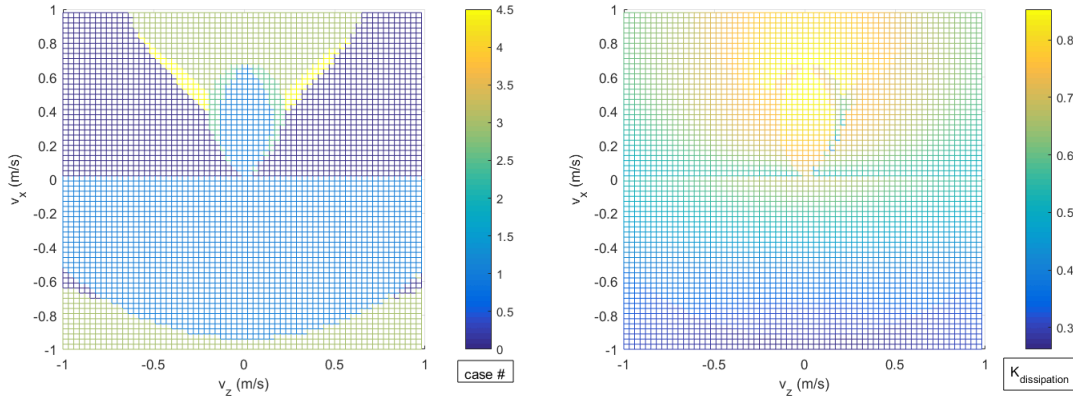


Figure 3.21: Influence of initial velocity v_x and v_z on cases study and energy dissipation $K_{dissipation}$

during both stages). When v_z equals to zero, as v_x decreases from 1 to -1 , the case of motion changes from 3 (sticking in restitution) to 1 (sticking in restitution) and finally back to 3.

Energy dissipation on the right side of the figure shows that the largest amount energy dissipation occurs in the region where initial velocities v_x ranging from 0 to 0.8 rad/s and v_z ranging from -0.3 to 0.3 . This region belongs to the transition between sliding to reverse sliding or sliding to sticking mode. The energy dissipation is symmetric between -1 to 0 and 1 to 0 along the x (v_z) axis due to the fact that only frictional force acting on this direction. However, the energy dissipation is asymmetric along the y (v_x) axis since frictional force and gravitational force are both acting on this axis with same direction between 1 to 0 and opposite direction between -1 to 0.

Influence of initial velocity v_x and v_z on post-impact dynamic quantities v'_x, v'_z and ω'_x, ω'_z Figure (3.22) shows the influence of initial velocity v_x and v_z on post-impact velocities. The figure on the left indicates that post-impact velocity v'_x is symmetric between -1 to 0 and 1 to 0 along the x (v_z) axis due to the fact that only frictional force acting on this direction which only depends on the sign of v_z . The figure on the right indicates that v'_z gradually change along v_z axis. Since the frictional force changes direction during this transition, there is discontinuity in regimes between transition of sliding to reverse sliding and sticking to reverse sliding. Fig (3.23) shows

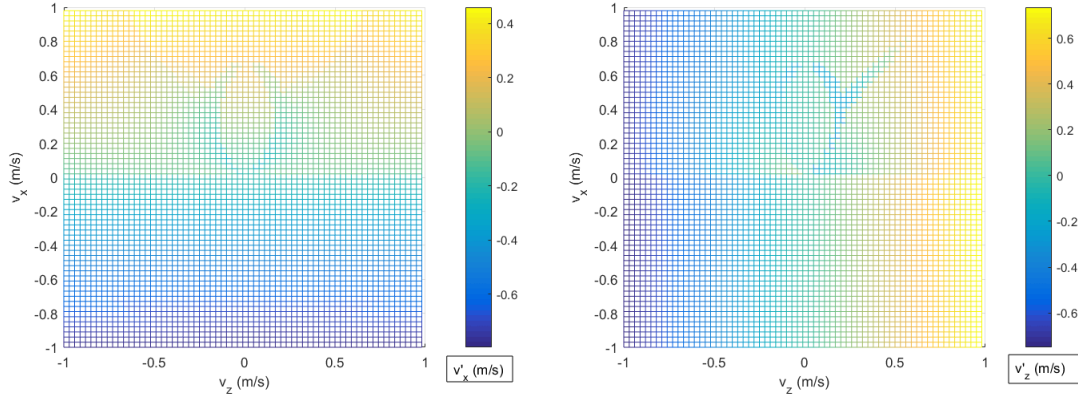


Figure 3.22: Influence of initial velocity v_x and v_z on post-impact velocities v'_x, v'_z

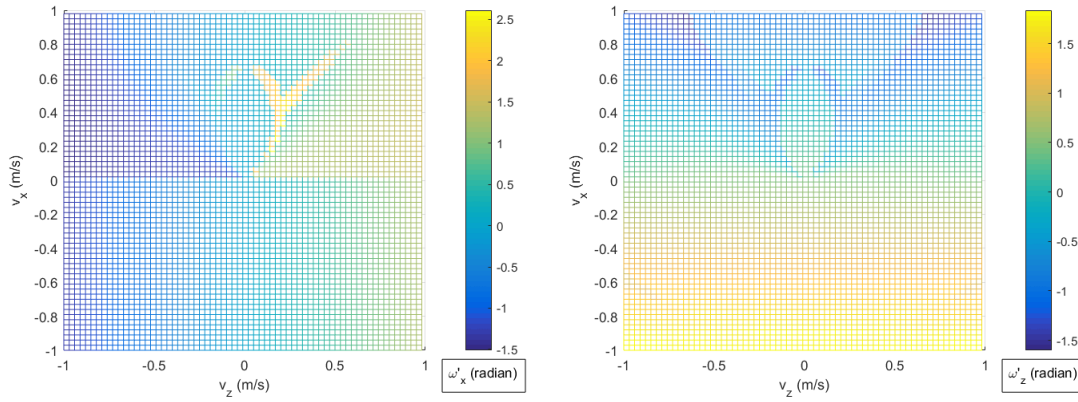


Figure 3.23: Influence of initial velocity v_x and v_z on post-impact angular velocities ω'_x, ω'_z

the influence of initial velocity v_x and v_z on post-impact angular velocities ω'_x, ω'_z . ω'_x has the same trend as v'_z and ω'_z has the same trend as v'_x . This can be proved by Eqn. (3.138), when expresses the velocity of the contact point after impact as

$$\vec{V}'^C = (V'_x + \omega'_y R_z - \omega'_z R_y) \vec{i} + (V'_y + \omega'_z R_x - \omega'_x R_z) \vec{j} + (V'_z + \omega'_x R_y - \omega'_y R_x) \vec{k} \quad (3.138)$$

When R_z is equal to zero, V'_x is only determined by V'_x and ω'_z . Also V'_z is only determined by V'_z and ω'_x .

3.8 Discussion and Conclusion

In this chapter, we have analyzed the three-dimensional rigid body impact model using Stronge's coefficient of restitution hypothesis.

1. The approach characterizes the possible modes and applies them to the general system impact response analysis. It is shown that there are eleven cases of impact, such as sliding in compression and reverse sliding in restitution stage. All these cases of impact are characterized and formulated into a general computational strategy.
2. Parameter evaluation is discussed for practicality in this chapter. Among these three initial parameters, orientation angles, the coefficient of restitution e_n and coefficient of friction μ , orientation angles have the greatest influence on energy dissipation since variation of orientation angle causes different modes while sliding or reverse sliding leads to more energy dissipation than sticking.
3. Using two parameter models of the friction coefficient (μ_k and μ_s) leads to different results in the transition area between sticking and reverse sliding. The larger the differences between μ_k and μ_s values, the bigger transition area and difference of energy dissipation. This difference results in discontinuity of velocity.

Overall, the conclusions reached in this chapter follow closely to the conclusion reached in chapter 2 when the orientation angle δ between the object and z axis equals $\frac{\pi}{2}$.

Chapter 4

Experimental Study for Three Dimensional Rigid Body Impact

In the previous chapter, we developed a numerical algorithm for three dimensional rigid body impact. The model is applied in a manner that requires the input of the coefficient of restitution, which is accurately determined through experiment. In order to verify our numerical simulation results and conclusions, an experiment, shown schematically in Figure (4.1), was set up to study the behavior of 3D rigid body impact with friction. The rigid body motion was captured using high speed video cameras. The elapsed time and the displacements of all marker points of moving bodies between those frames were obtained. The pre-impact and the post-impact velocities and angular velocities were calculated using the data, considering the gravitational effect.

4.1 Experimental Set-up

The experimental set-up, shown in Figure (4.2), includes the following apparatus:

1. Moving objects: Two different types of moving objects, a rod and rectangular bar were considered in this experiment. Reflective tape markers (silver) attached to these objects, one at the center and others located along the edges, were used to capture the kinematic data.

2. Dropping device: The dropping device was designed to meet the requirement that the pre-collision velocities and orientations of the objects should be independently adjustable while maintaining the same impact contact point. Two adjustments were incorporated:

- i) Initial release height and angles which determine the tangential velocities v_x , v_z and vertical v_y of the object.

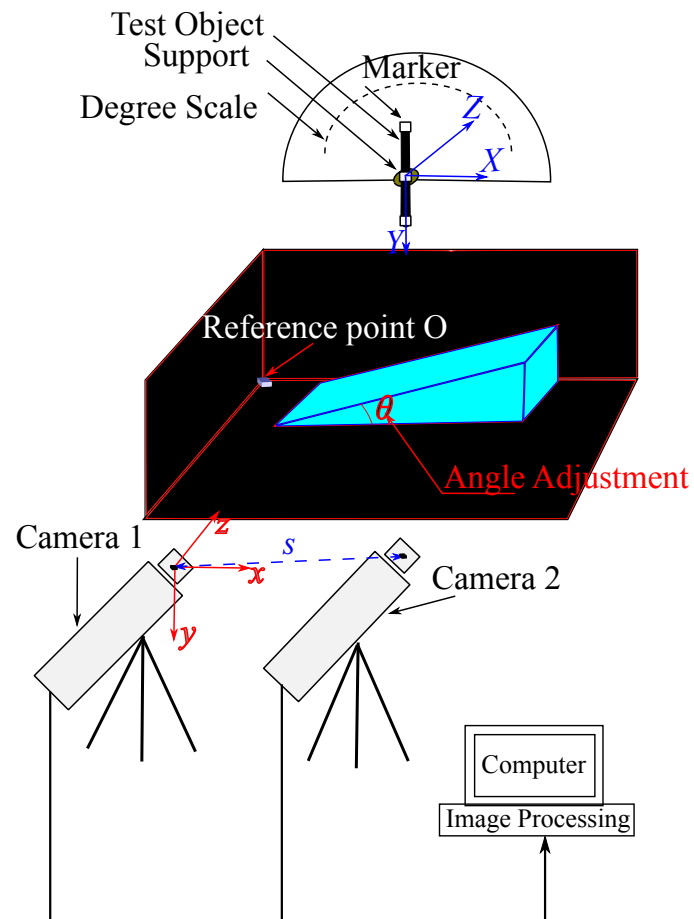


Figure 4.1: Schematic diagram of 3D Experiment platform

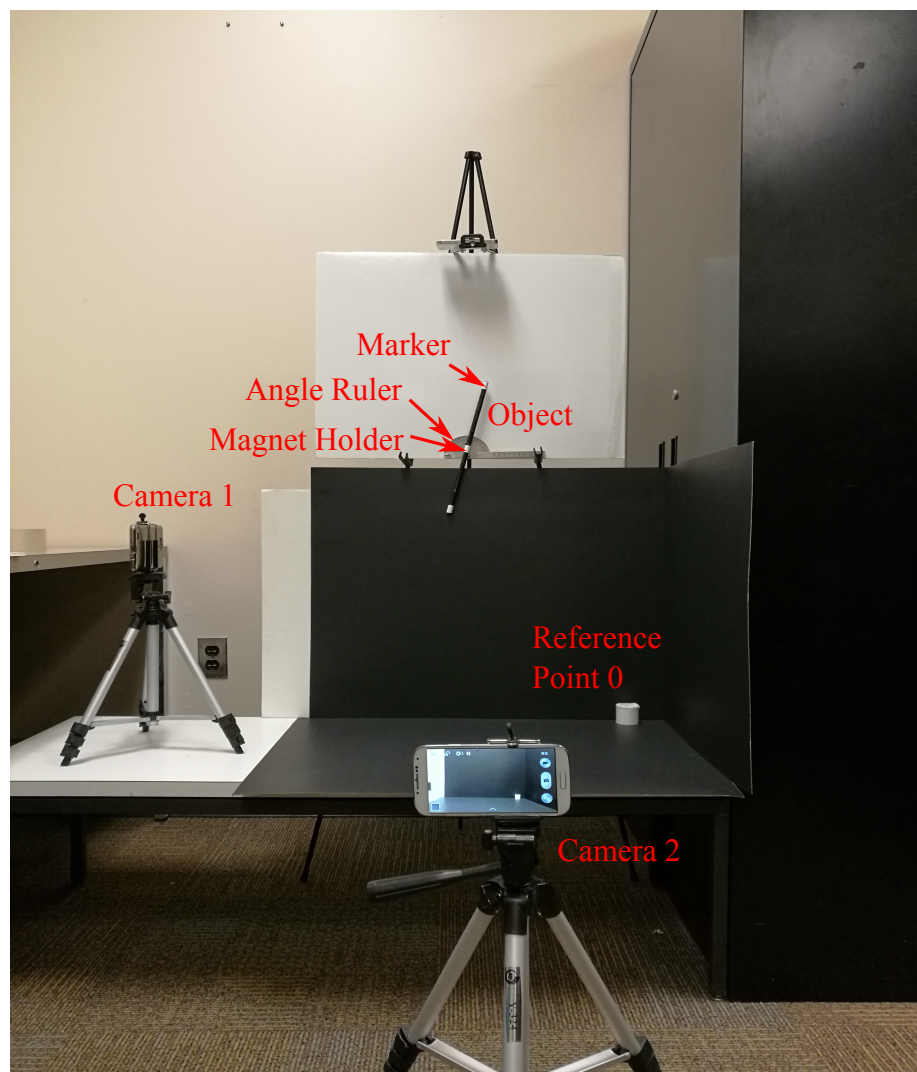


Figure 4.2: Experiment set-up

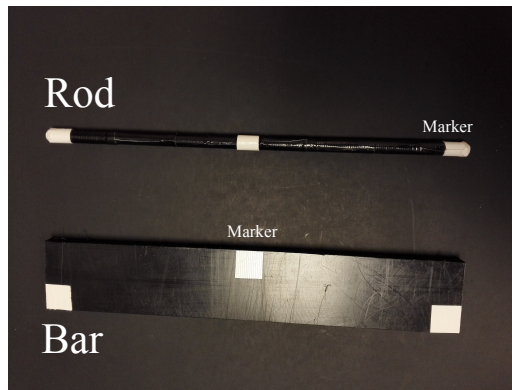


Figure 4.3: Moving objects

ii) Angle θ of the slope which determine the orientation angle.

3. Data acquisition system: Two high speed cameras (a max capture rate of 120 frames/sec) were used to acquire the kinematic data. After each impact test, videos saved in the cameras were transferred to a computer. It is possible for the marker to become invisible during impact because it may be blocked by the object body or other markers at some special angles. To make sure all markers can be tracked during impact, it is necessary to add more additional cameras in the future.

4. Image processing system: All video images of each experiment were collected and transmitted into a computer. A Matlab program based on Kalman Filter algorithm was used to turn videos into frames according to time length of each video and compute displacements of all markers on the object. The position data was then used to calculate the inclination angle of the bar at the instant of collision and pre and post impact dynamic quantities.

4.1.1 Moving Objects

The steel rod and UHMW (ultra high molecular weight) plastic rectangular bar, shown in Figure (4.3), were painted black and attached with silver reflective tape markers along their surfaces. This high contrast enhancement improves the perceptibility of the markers in the image by enhancing the brightness difference between the markers and their backgrounds. It can also sharpen object edges and remove much of the image blur.

The kinematic and dynamic parameters of the objects are given in Table (4.1).

Name	Mass (kg)	Mass moment of inertia ($kgmm^2$)	Dimensions (mm)
Steel Rod	0.169	$\begin{bmatrix} 1312 & 0 & 0 \\ 0 & 0.0038 & 0 \\ 0 & 0 & 1312 \end{bmatrix}$	$L = 304.8$ $R = 9.525$
Rectangular bar	0.185	$\begin{bmatrix} 43.30 & 0 & 0 \\ 0 & 1451 & 0 \\ 0 & 0 & 1489 \end{bmatrix}$	$L_1 = 306.5$ $L_2 = 51.5$ $L_3 = 12.5$

Table 4.1: Kinematic and dynamic parameters of the objects used in impact tests

4.1.2 Dropping Device

Figure (4.4) shows the set-up of the dropping device. It includes an object holder with adjustable height h , a laser level, and a stainless steel $0 - 180^\circ$ angle ruler. A cylinder, $h = 45\text{ mm}$ and $R = 45\text{ mm}$, is attached on the ground. It is treated as reference frame origin point O which is $(0, 0, 0)$ on (x, y, z) reference frame. This point is the first step of calibration for determining the relative three dimensional positions of object in the video.

4.1.3 Data Acquisition System

Camera Calibration

Camera calibration is one of the most important parts in a data acquisition system. Three-dimensional digital image correlation (DIC) techniques have significantly advanced from their counterparts in the 1980s. Images taken from a stereo pair of charge coupled device (CCD) cameras can be used to determine displacement in three dimensions of any object whose background has had a contrasting speckle pattern applied to it [57]. This non-contact optical technique can take measurements at several points of an object in a single snapshot.

In this experiment, a Huawei Honor 8 video camera, shown in Figure (4.5), is used for video recording. It can capture a maximum of 120 frames/sec with $1280 * 720$ pixels

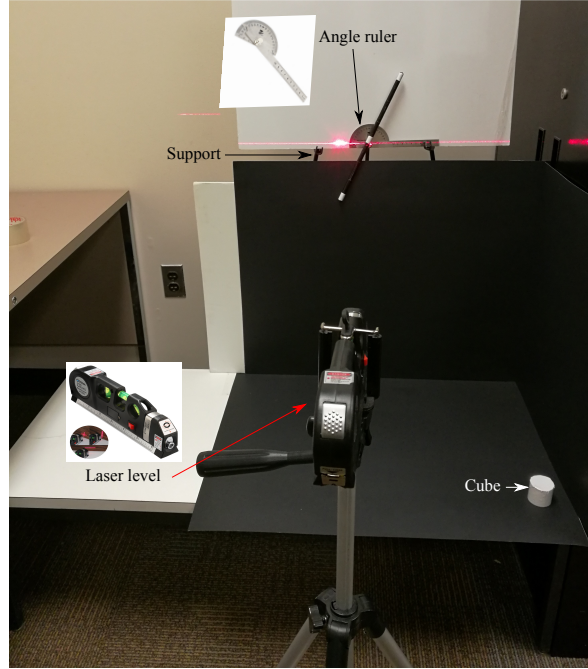


Figure 4.4: Dropping device

resolution. Camera calibration is used to estimate the values of the intrinsic parameters, the extrinsic parameters, and lens distortion parameters of the cameras.

Intrinsic parameters and lens distortion parameters of cameras The intrinsic 3 by 3 matrix, K , generated by the calibration scheme, given by

$$K = \begin{bmatrix} \alpha_x & \gamma & u_0 \\ 0 & \alpha_y & v_0 \\ 0 & 0 & 1 \end{bmatrix} \quad (4.1)$$

contains 5 intrinsic parameters. The parameters $\alpha_x = f \cdot m_x$ and $\alpha_y = f \cdot m_y$ represent focal length in terms of pixels, where m_x and m_y are the scale factors relating pixels to distance and f is the focal length in terms of distance [57]. The parameter γ represents the skew coefficient between the x and the y axis, and is often 0. u_0 and v_0 represent the principal point, which would be ideally in the center of the image.

$$C[x, y, 1] = [X, Y, Z, 1] \begin{bmatrix} R \\ t \end{bmatrix} K \quad (4.2)$$

The coordinate (X, Y, Z) are world coordinates of a point, while the coordinate (x, y) are coordinates of the corresponding image point. C is dimensional scale factor.

Nonlinear intrinsic parameters such as lens distortion are also important although they cannot be included in the linear camera model described by the intrinsic parameter matrix. Many modern camera calibration algorithms estimate these intrinsic parameters as well in form of non-linear optimization techniques. This is done in form of optimizing the camera and distortion parameters in from of what is generally known as bundle adjustment. [64]

Extrinsic parameters of cameras 3 by 3 matrix R , 1 by 3 matrix T constitute the extrinsic parameters which denote the coordinate system transformations from 3D world coordinates to 3D camera coordinates. Equivalently, the extrinsic parameters define the position of the camera center and the camera's heading in world coordinates. T is the position of the origin of the world coordinate system expressed in coordinates of the camera-centered coordinate system. T is often mistakenly considered the position of the camera. The position, C , of the camera expressed in world coordinates is $C = -R^{-1}T = -R^T T$ (since R is a rotation matrix).

There are two steps involved in camera calibration:

1. Solve for the intrinsics and extrinsics in closed form, assuming that lens distortion is zero [65].
2. Estimate all parameters simultaneously including the distortion coefficients using nonlinear least-squares minimization (Levenberg–Marquardt algorithm). Use the closed form solution from the preceding step as the initial estimate of the intrinsics and extrinsics. Then set the initial estimate of the distortion coefficients to zero [64].

Synchronizing Cameras

Since impact is almost instantaneous and time laspe is $1/120$ sec per frame, it is necessary to make sure that all cameras record synchronously. We accomplish this by



Figure 4.5: Huawei Honor 8 with tripod

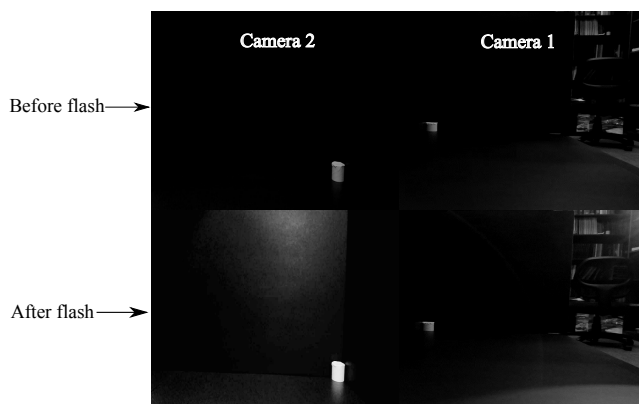


Figure 4.6: Images from 2 cameras before and after flash

generating a flash from the flashlight before object starts to fall down, as image frames from three cameras shown in Figure (4.6). A flash signal was triggered before the object was released. This signal helps to mark the same starting point of recording timeline in both cameras. Also, a voice control command is used to start all cameras' video recording at the same time.

4.1.4 Image Processing System

Once all videos are saved into the computer, we make use of a Matlab program based on Kalman Filter algorithm developed for motion capture to digitize the position of markers with respect to the global reference frame $x - y - z$.

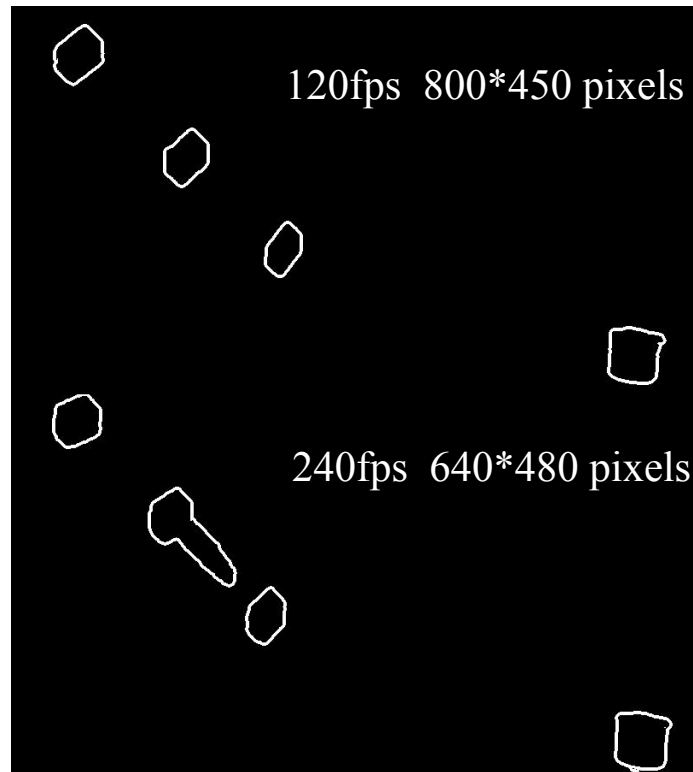


Figure 4.7: Comparison 120fps with high resolution (800*450 pixels) image to 240fps with high resolution (640*480 pixels) image

We should note that during the collision the position of the object changes while it deforms. These deformations which are in scale of micrometers, are so small that they could not be detected on the video images. Therefore, the experimentally obtained kinematic data only reflects the general rigid body motion of the object.

4.2 Video Recording and Image Processing

4.2.1 Setting and Synchronizing Cameras for Video Recording

Figure (4.7) shows images from 120 fps with high resolution and 240 fps with lower resolution. Although 240 fps can provide more detailed information, which is better to interpolate dynamic quantities in same amount of time, it produces a blur on the marker boundary. This disadvantage makes it more difficult to obtain the correct position of each marker. As a result, 120 fps with higher resolution was selected as the better choice for video setting. This property depends on the type of camera used.

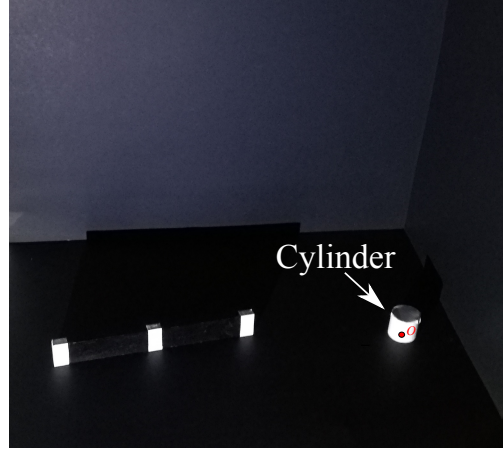


Figure 4.8: Reference point on ground

4.2.2 Setting Reference Point on the Ground and Camera Calibration

Reference Point

As shown in Figure (4.8), a white cylinder was attached on the ground. This cylinder was set as the focus point of the camera. Since the cylinder is still during impact, it can be used as reference point O on (x, y, z) world/reference frame and its position (x_0, y_0, z_0) is invariable in world frame. This invariable property can be used to estimate errors in later sections. With a dimension of $R = 45mm$ and $h = 45mm$, the cylinder can be seen from all cameras from different angles. This point O is used to set camera focus to a fix length.

Camera Calibration

A stereo system consists of two cameras: camera 1(left) and camera 2(right). As shown in Figure (4.9), camera 1 and camera 2 capture point X in a reference(world) frame into different images as point (x_1, y_1) and (x_2, y_2) . If camera 1 location is set to be $(0, 0, 0)$ in reference frame, camera 2 location can be calculated from the rotation matrix R and translation t that relates the camera locations to each other. The calibration procedure given below estimates the parameters of each of the two cameras.

1. Prepare images, camera, and calibration pattern.

A checkerboard pattern is used, as shown in Figure (4.10), in the calibration. A

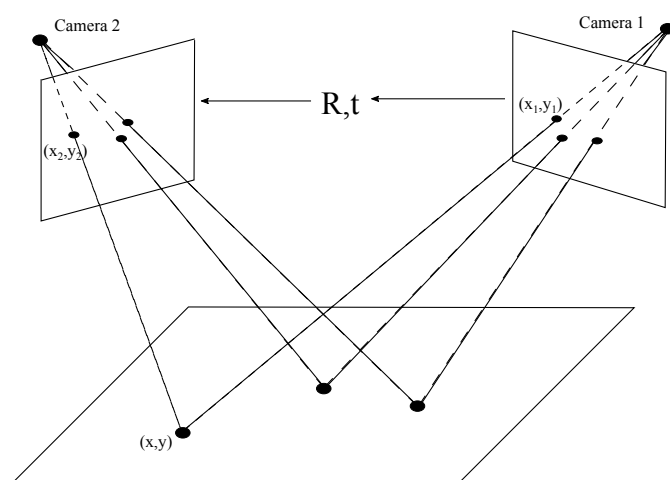


Figure 4.9: Projective transformation between two images from stereo camera (rear view shown)

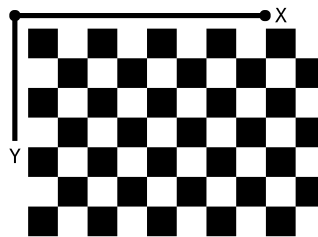


Figure 4.10: Checkerboard pattern

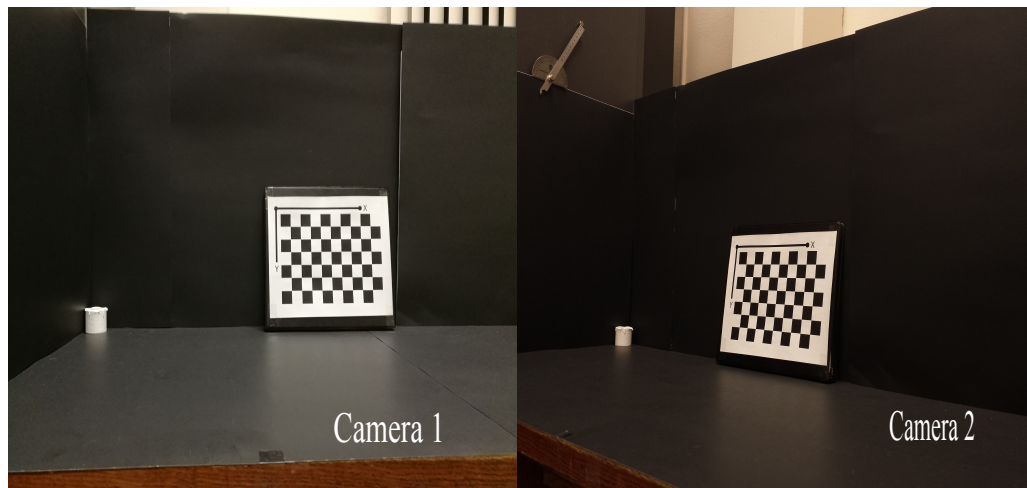


Figure 4.11: Example of checkerboard pattern placement

reference cylinder is set next to the pattern so that both of them are in focus. Since the closed form solution for parameters of camera needs at least 8 positions (image pairs), for best results, we used more than 10 image pairs of the calibration pattern. As shown in Figure (4.11), the pattern needs to be visible from both cameras. The actual length of one side of a square from the checkerboard pattern is measured as $23mm$.

2. Calibrate the stereo camera.

Figure (4.12) displays one image pair. This image pair displays the checkerboard image pair with green circles to indicate detected points. The yellow square indicates the $(0,0)$ origin. The X and Y arrows indicate the orientation of the checkerboard axes. After all sets of position information from the images were collected and calibrated, camera 1 & 2 and pattern positions were calculated in world coordinate from Eqn (4.3) and shown in Figure (4.13). In the Figure, Camera 1 was set to be the origin as $(X_C, Y_C, Z_C) = (0, 0, 0)$.

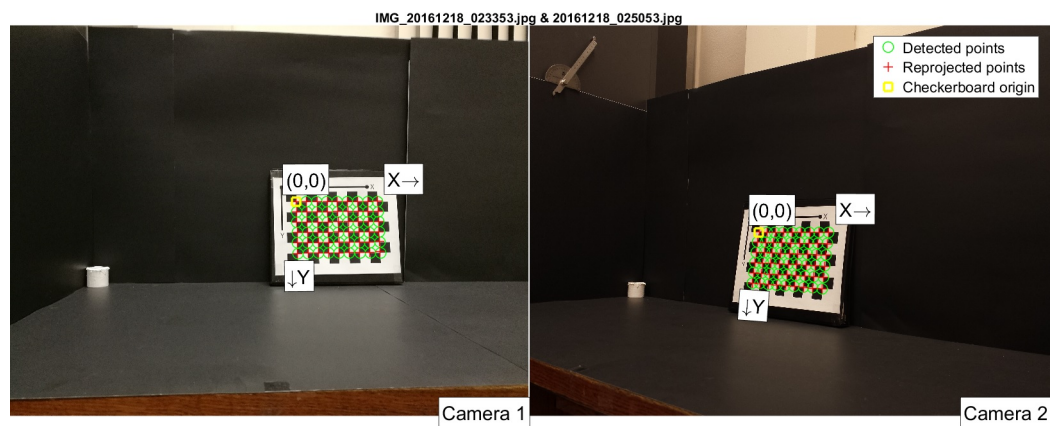


Figure 4.12: Checkerboard pattern detected from image

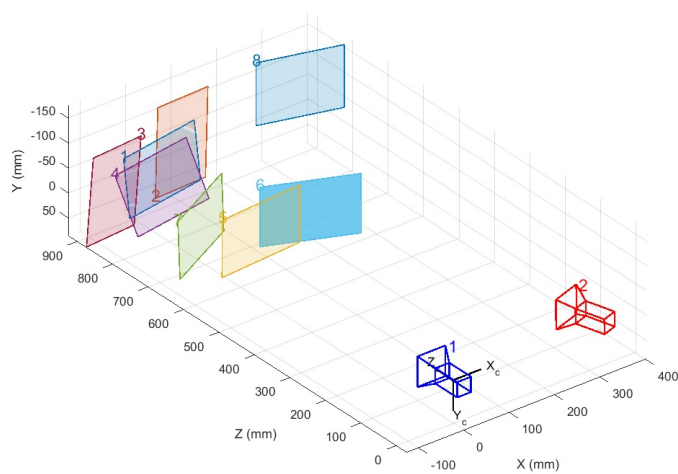


Figure 4.13: 3D view of cameras and pattern positions

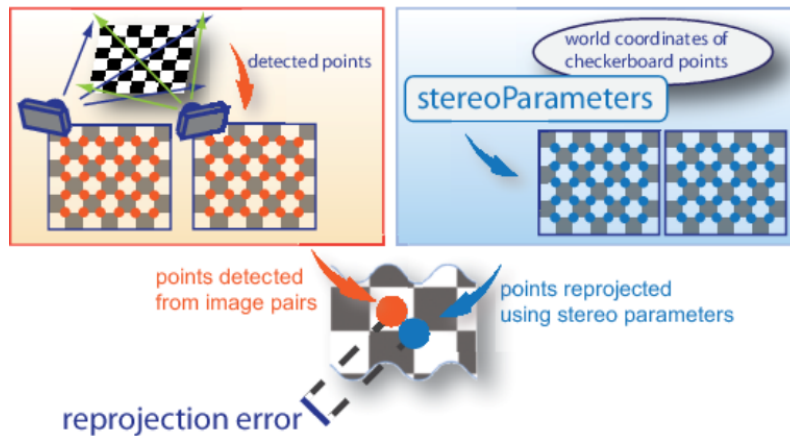


Figure 4.14: Reprojection errors illustration

3. Evaluate calibration accuracy.

Calibration accuracy needs to be evaluated by examining the reprojection errors, the camera extrinsics, and by viewing the undistorted image. Since the undistortion treatment has been mentioned in Chapter 2 experiment, it is not discussed here again. The reprojection errors, as shown in Fig (4.14), are the distances in pixels between the detected and the reprojected points. This measurement calculates reprojection errors by projecting the checkerboard points from world coordinates, defined by the checkerboard, into image coordinates. Then it compares the reprojected points to the corresponding detected points. As a general rule, reprojection errors of less than one pixel are acceptable. The bar graph in Figure (4.15) displays the mean reprojection error per image, along with the overall mean error. The bar labels correspond to the image pair IDs. The highlighted pair of bars corresponds to the selected image pair.

4. Export the parameters.

The intrinsic and extrinsic parameters of the camera, as well as the distortion coefficients, are listed in Tables (4.2) and (4.3).

4.2.3 Acquiring Displacement Information from Image Processing

The recorded videos are transferred into the computer. For each experiment, 60 frames, which span a time period of 0.5 sec, are used to estimate the kinematics of the object.

The image processing procedure can be divided into two parts:

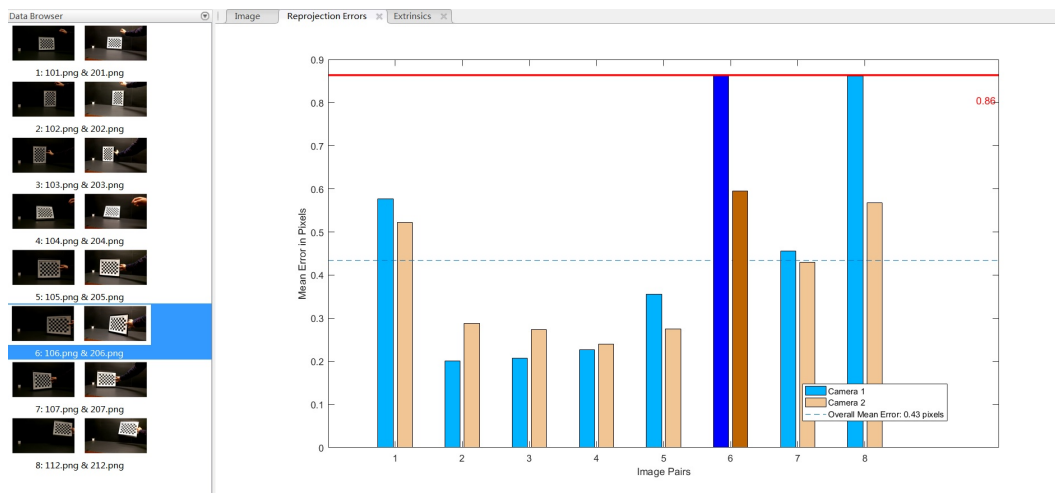


Figure 4.15: Reprojection errors in images

Name	Intrinsic Matrix K	Extrinsic Matrix	R t
Camera 1	$\begin{bmatrix} 1.06e+03 & 0 & 0 \\ 0 & 1.07e+03 & 0 \\ 0.733e+03 & 0.396e+03 & 1 \end{bmatrix}$	$\begin{bmatrix} 0.984 & 0.005 & 0.176 \\ 0.019 & 0.991 & -0.131 \\ -0.175 & 0.133 & 0.976 \\ -31.1 & -49.6 & 890 \end{bmatrix}$	
Camera 2	$\begin{bmatrix} 0.990e+03 & 0 & 0 \\ 0 & 0.989e+03 & 0 \\ 0.732e+03 & 0.380e+03 & 1 \end{bmatrix}$	$\begin{bmatrix} 0.992 & 0.040 & -0.117 \\ -0.0574 & 0.987 & -0.148 \\ 0.109 & 0.153 & 0.982 \\ -109 & -52.5 & 924.5 \end{bmatrix}$	

Table 4.2: Intrinsic and Extrinsic Matrix of camera 1 and 2

Name	Distortion Coefficient	Mean Errors	Relative Pose	$\begin{bmatrix} R \\ t \end{bmatrix}$
Camera 1	$[0.238, -0.597]$	0.4686pixels	$\begin{bmatrix} 1 & 0 & 0 \\ 0 & 1 & 0 \\ 0 & 0 & 1 \\ 0 & 0 & 0 \end{bmatrix}$	
Camera 2	$[0.131, -0.157]$	0.3992pixels	$\begin{bmatrix} 0.9566 & 0.0311 & -0.2897 \\ -0.0375 & 0.9992 & -0.0166 \\ 0.2889 & 0.0267 & 0.9570 \\ -338.8 & -25.82 & 62.57 \end{bmatrix}$	

Table 4.3: Parameters of camera 1 and 2

Image Enhancement

Each video is recorded into frames. The first frame with flash signal is treated as the starting point of the timeline if it is not the first frame of video. After that, 60 consecutive frames are selected before and after impact. As shown in Figure (4.16), The picture A in Figure (4.16) is the original frames. These color frames are turned into grayscale in picture B. Then they are turned into black and white pictures, shown in picture C. And finally all markers with boundaries are outlined in the frames as shown in picture D. The 60 new frames are constructed into a new video after the image enhancement process.

Object Tracking using Kalman Filter

Kalman filtering, also known as linear quadratic estimation (LQE), is an algorithm that uses a series of measurements observed over time, containing statistical noise and other inaccuracies, and produces estimates of unknown variables that tend to be more precise than those based on a single measurement alone, by using Bayesian inference and estimating a joint probability distribution over the variables for each timeframe. Since our motion capture rate in the test is 120 fps, every timeframe is $\frac{1}{120}$ sec. As shown in

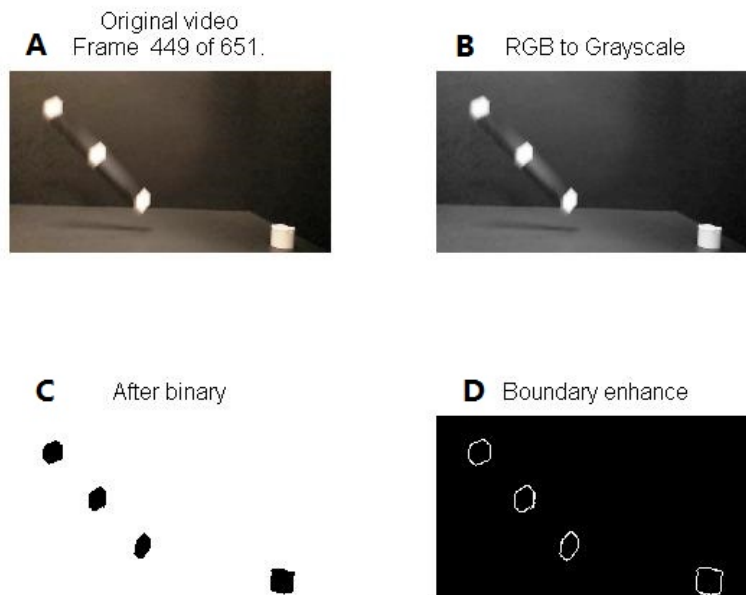


Figure 4.16: Image enhancement

Figure (4.17), every marker attached to the object is tagged and tracked through frames. The position information of every marker in each frame are stored in the database.

4.2.4 Converting Displacement Information into a 3D(x, y, z) Reference Frame

Because only two dimensional information can be attained through image processing from any camera video, the database stored sets of position (x_i, y_i) , as shown in Figure (4.18), for each marker in a single frame. The 3D position for each marker (x, y, z) is calculated using Eqn (4.3). After all sets of position information were collected and calibrated, a set of position (x, y, z) was combined for each marker according to a single frame.

$$C[x, y, 1] = [X, Y, Z, 1] \begin{bmatrix} R \\ t \end{bmatrix} K \quad (4.3)$$

in which (X, Y, Z) are world coordinates of a point and (x, y) are coordinates of the

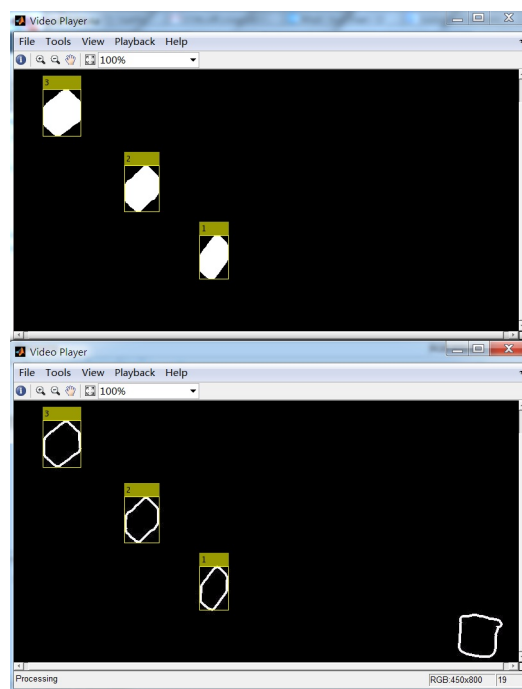


Figure 4.17: Markers tagged in each frame

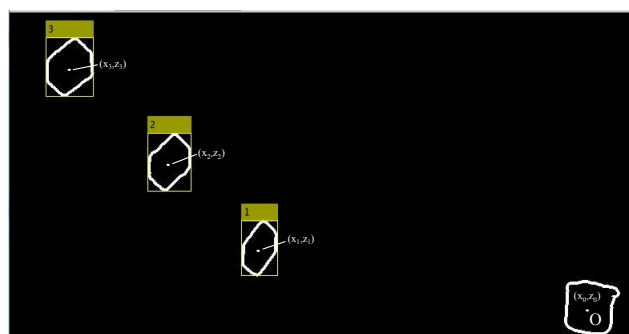


Figure 4.18: Position of markers and relative point O

corresponding image point. C is dimensional scale factor. K , a 3 by 3 matrix, is camera intrinsic matrix. R , a 3 by 3 matrix, is the matrix representing the 3-D rotation of the camera and t , a 1 by 3 matrix is translation of the camera relative to the world coordinate system.

Once again, the rigid body deformations in the scale of micrometers are negligible and difficult to be detected on the video images. Therefore, we are assuming that the length of object won't change, which implies the two-dimensional distance between any markers remains the same during impact. Also, if the actual dimensions of the object and location of reference point O are known, the position of markers in (x, y, z) reference frame can be easily scaled in the test. In other words, this dimensionless property makes our simulation and experiment results comparison much easier. Figure (4.19) shows an example of three markers positions stored in database.

Trajectories									
120									
Frame	marker 1			marker 2			marker 3		
	x	y	z	x	y	z	x	y	z
1	238.245	496.256	1105.35	197.304	366.71	1123.56	362.34	365.883	1039.82
2	238.212	496.352	1105.4	197.035	366.752	1123.81	362.248	365.957	1040.02
3	238.199	496.39	1105.37	196.426	366.703	1124.75	362.262	365.995	1040.06
4	238.275	496.541	1105.32	196.853	366.867	1124.17	362.259	365.992	1040.09
5	238.255	496.547	1105.36	197.198	366.983	1123.99	362.286	365.969	1039.92
6	238.674	496.744	1105.63	196.136	366.797	1125.8	362.325	366.052	1039.94
7	238.676	496.735	1105.71	195.972	366.87	1126.56	362.276	366.075	1040.2
8	238.773	496.795	1105.58	195.999	367.001	1126.56	362.311	366.093	1040.19
9	238.832	496.913	1105.65	196.182	367.06	1126.52	362.354	366.13	1040.18
10	238.74	496.882	1105.67	196.09	367.015	1126.59	362.323	366.229	1040.23
11	238.778	496.874	1105.76	196.151	367.032	1126.58	362.366	366.227	1040.28
12	238.808	496.88	1105.72	196.216	367.14	1126.68	362.352	366.319	1040.3
13	238.802	496.884	1105.73	196.207	367.142	1126.69	362.429	366.276	1040.15
14	238.716	496.835	1105.78	196.026	366.993	1126.62	362.45	366.312	1040.33
15	238.682	496.788	1105.86	196.253	367.005	1126.76	362.513	366.302	1040.15
16	238.756	496.794	1105.91	196.252	366.991	1126.82	362.486	366.292	1040.17
17	238.708	496.779	1105.99	196.262	366.99	1126.8	362.545	366.393	1040.34
18	238.747	496.789	1105.94	196.766	367.175	1126.32	362.552	366.361	1040.42
19	238.773	496.739	1106.07	196.468	366.935	1126.78	362.579	366.389	1040.33
20	238.793	496.608	1106.09	196.816	367.071	1126.33	362.621	366.267	1040.39
21	238.839	496.596	1106.17	196.523	366.806	1126.85	362.643	366.251	1040.38
22	238.802	496.55	1106.26	196.437	366.744	1126.97	362.641	366.253	1040.39
23	238.852	496.536	1106.35	196.471	366.763	1126.93	362.629	366.233	1040.35
24	238.847	496.492	1106.42	196.751	366.71	1126.59	362.575	366.21	1040.5
25	238.8	496.474	1106.49	196.343	366.529	1127.1	362.656	366.241	1040.4
26	238.896	496.363	1106.51	196.862	366.758	1126.56	362.617	366.195	1040.43
27	238.914	496.338	1106.51	196.376	366.426	1127.07	362.635	366.101	1040.42
28	238.851	496.301	1106.53	196.283	366.361	1127.18	362.673	366.13	1040.36
29	238.837	496.32	1106.64	196.569	366.459	1127.16	362.646	366.057	1040.24
30	238.882	496.324	1106.57	196.396	366.38	1127.23	362.686	366.07	1040.54
31	238.829	496.306	1106.66	196.573	366.46	1127.16	362.709	366.185	1040.52
32	238.933	496.308	1106.63	196.614	366.482	1127.12	362.766	366.08	1040.57
33	238.936	496.32	1106.65	197.085	366.671	1126.66	362.807	366.099	1040.53
34	238.94	496.32	1106.64	196.587	366.436	1127.19	362.891	366.23	1040.09
35	238.891	496.305	1106.72	196.501	366.377	1127.3	362.741	366.102	1040.48
36	238.958	496.332	1106.6	196.543	366.405	1127.25	362.763	366.212	1040.5
37	238.935	496.306	1106.69	196.767	366.514	1127.13	362.955	366.216	1040.17
38	239.029	496.34	1106.53	196.894	366.6	1127	363.027	366.207	1040.18
39	238.617	496.275	1107.16	196.91	366.602	1126.99	362.921	366.229	1040.49
40	238.997	496.446	1106.56	196.609	366.433	1127.2	362.969	366.251	1040.48
41	239.026	496.48	1106.52	196.846	366.55	1127.08	363.103	366.339	1040.3
42	239.036	496.502	1106.58	196.892	366.693	1127.05	363.055	366.238	1040.19
43	239.099	496.529	1106.49	197.389	366.893	1126.57	363.076	366.326	1040.37
44	239.101	496.506	1106.52	197.025	366.725	1127.05	363.118	366.406	1040.44
45	239.109	496.52	1106.46	196.747	366.47	1127.22	363.166	366.247	1040.23
46	239.097	496.543	1106.45	197.016	366.72	1127.06	363.08	366.366	1040.55
47	239.063	496.517	1106.55	196.981	366.537	1126.84	363.171	366.308	1040.46
48	239.175	496.453	1106.37	197.505	366.823	1126.46	363.192	366.233	1040.24
49	239.206	496.461	1106.33	197.631	366.862	1126.47	363.212	366.315	1040.54
50	239.165	496.45	1106.4	197.204	366.642	1127.04	363.315	366.339	1040.44

Figure 4.19: Three markers positions data collected from 50 frames

4.2.5 Calculation of Pre- and Post-impact Dynamic Quantities

As discussed before, 60 frames, which span a period of 0.5 sec, are used to estimate the kinematics of the object in each test. Then, the data is divided into pre- and post-collision parts. We developed an algorithm based on the free motion of the object in the gravitational field to interpolate both pre and post position data. The orientation angles (β, γ, δ) of the object at the contact point, the angular velocities of the object immediately before and after collision $(\dot{\theta}_1^-, \dot{\theta}_1^+)$ $(\dot{\theta}_2^-, \dot{\theta}_2^+)$ $(\dot{\theta}_3^-, \dot{\theta}_3^+)$, and the center of mass velocities $(\dot{x}^-, \dot{y}^-, \dot{z}^-)$, $(\dot{x}^+, \dot{y}^+, \dot{z}^+)$ are calculated from the interpolated data.

Dimensional Scale Factor C

In Euclidean geometry, uniform scaling (or isotropic scaling) is a linear transformation that enlarges (increases) or shrinks (diminishes) objects by a scale factor that is the same in all directions. The result of uniform scaling is similar (in the geometric sense) to the original. To scale the position from image to real geometry of object, a scale factor C is needed. The length l of the object won't change because of the rigid-body assumption. This means that the two-dimensional distance between any markers will not change during impact. The following equations (4.4,4.5) are used to calculate real position (x, y, z) of markers.

$$C = \frac{l}{\sqrt{(x_3 - x_1)^2 + (y_3 - y_1)^2 + (z_3 - z_1)^2}} \quad (4.4)$$

$$(x, y, z) = (C \cdot x, C \cdot y, C \cdot z) \quad (4.5)$$

From Table (4.1), the actual length of the rod is $298.5mm$ and the distance between the top and bottom markers is $248.8mm$. So $C = \frac{298.5}{248.8} = 1.20$.

Calculation for Dynamic Quantities

Houbolt method The Houbolt method is one of several approaches to calculate a derivative. It is based on third-order interpolation of displacements X_t and the multistep

implicit formulae for X_t . The time derivative \dot{X}_t is obtained in terms of X_t by using backward differences. [66] The difference formulae are summaried in the following:

$$X_t = X_{t+\Delta t} - \Delta t \dot{X}_{t+\Delta t} + \frac{\Delta t^2}{2} \ddot{X}_{t+\Delta t} - \frac{\Delta t^3}{6} \dddot{X}_{t+\Delta t} \quad (4.6)$$

$$X_{t-\Delta t} = X_{t+\Delta t} - (2\Delta t) \dot{X}_{t+\Delta t} + \left(\frac{2\Delta t}{2}\right)^2 \ddot{X}_{t+\Delta t} - \left(\frac{2\Delta t}{6}\right) \dddot{X}_{t+\Delta t} \quad (4.7)$$

$$X_{t-2\Delta t} = X_{t+\Delta t} - (3\Delta t) \dot{X}_{t+\Delta t} + \left(\frac{3\Delta t}{2}\right)^2 \ddot{X}_{t+\Delta t} - \left(\frac{3\Delta t}{6}\right)^3 \dddot{X}_{t+\Delta t} \quad (4.8)$$

Solving Eqns. (4.6,4.7,4.8), we obtain an estimate of the time derivative

$$\dot{X}_{t+\Delta t} = \left(\frac{1}{6\Delta t}\right)(11X_{t+\Delta t} - 18X_t + 9X_{t-\Delta t} - 2X_{t-2\Delta t}) \quad (4.9)$$

Note that a knowledge of X_t , $X_{t-\Delta t}$ and $X_{t-2\Delta t}$ is needed to find solution for $X_{t+\Delta t}$. We will use this method to solve for angular velocity and velocity from displacement information.

Angular Velocity First, as shown in Figure (4.20), the unit vectors $(\vec{e}_1, \vec{e}_2, \vec{e}_3)$ of the body fixed frame is bulit. By knowing (x, y, z) position of markers A_1, A_2, A_3 in the reference coordinate xyz , unit vectors $(\vec{e}_1, \vec{e}_2, \vec{e}_3)$ can be attained by the following equations. Note that point G is the centroid of triangle.

$$\vec{e}_1 = \frac{(x_2 - x_G)\vec{i} + (y_2 - y_G)\vec{j} + (z_2 - z_G)\vec{k}}{\sqrt{(x_2 - x_G)^2 + (y_2 - y_G)^2 + (z_2 - z_G)^2}} \quad (4.10)$$

$$\vec{e}_3 = \vec{e}_1 \times \overrightarrow{GA_1} \quad (4.11)$$

$$\vec{e}_2 = \vec{e}_3 \times \vec{e}_1 \quad (4.12)$$

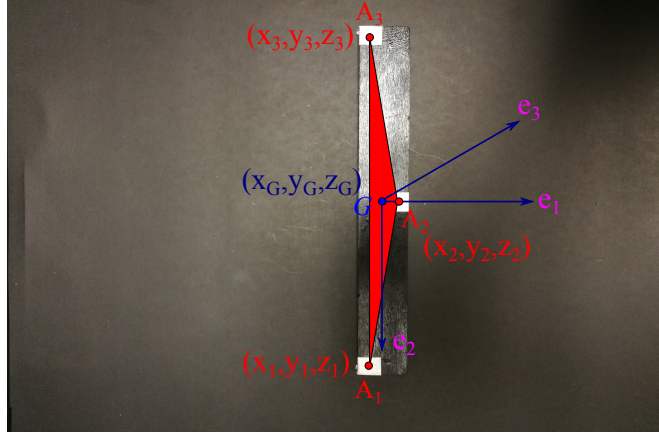


Figure 4.20: Frame constructed using three markers

in which

$$x_G = \frac{1}{3}(x_1 + x_2 + x_3) \quad y_G = \frac{1}{3}(y_1 + y_2 + y_3) \quad z_G = \frac{1}{3}(z_1 + z_2 + z_3) \quad (4.13)$$

An example of body fixed frame using triangle shape is shown in Figure (4.21). The centroid of object is located at (x_G, y_G, z_G) . It can be used to calculate the orientation angles β , γ and δ by

$$\tan^{-1} \beta = \frac{(x_G - x_1)}{\sqrt{(x_G - x_1)^2 + (y_G - y_1)^2 + (z_G - z_1)^2}} \quad (4.14)$$

$$\tan^{-1} \gamma = \frac{(y_G - y_1)}{\sqrt{(x_G - x_1)^2 + (y_G - y_1)^2 + (z_G - z_1)^2}} \quad (4.15)$$

$$\tan^{-1} \delta = \frac{(z_G - z_1)}{\sqrt{(x_G - x_1)^2 + (y_G - y_1)^2 + (z_G - z_1)^2}} \quad (4.16)$$

Euler angles are one of the most widely used parameterizations of rotations when studying the dynamic behavior of a moving object with rotation [9]. Let $\{E_1, E_2, E_3\}$ be a basis for a fixed reference frame, and let $\{e_1, e_2, e_3\}$ be a basis for a body attached frame. The 2 – 1 – 3 Euler angles provide an orthogonal matrix Q which maps $\{E_1, E_2, E_3\}$ to $\{e_1, e_2, e_3\}$. As shown in Figure (4.22), the rotation matrix Q can be

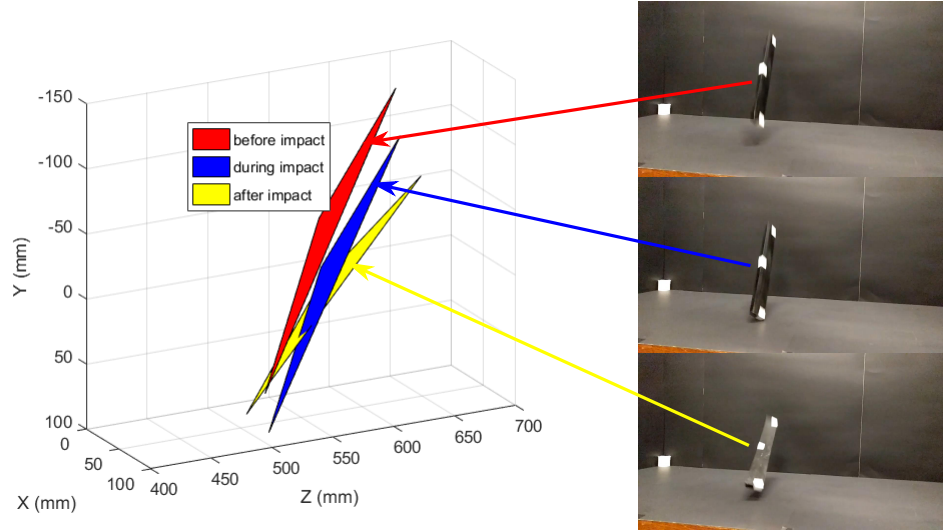


Figure 4.21: Examples of frame constructed using three markers positions

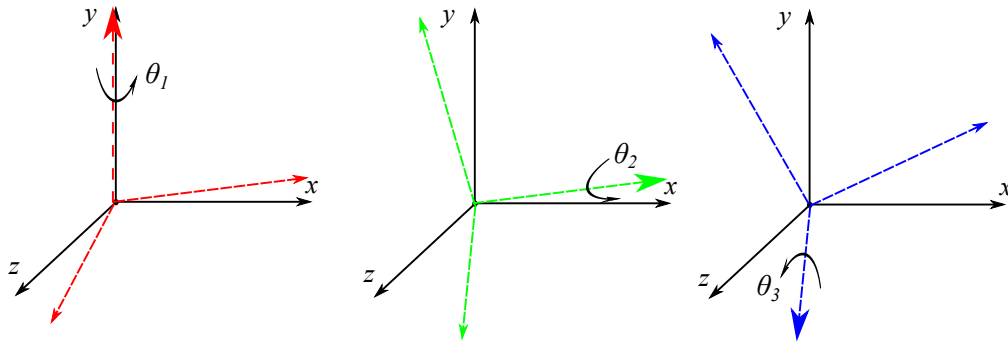


Figure 4.22: Schematic of the 2-1-3 motion in terms of the Euler angles $(\theta_1, \theta_2, \theta_3)$

seperated into three rotations and described as followed.

$$[Q]^T = [R(\theta_3)][R(\theta_2)][R(\theta_1)] \quad (4.17)$$

The mapping from reference basis to body frame basis is

$$e = Q^T E \quad (4.18)$$

$$\begin{bmatrix} e_1 \\ e_2 \\ e_3 \end{bmatrix} = \begin{bmatrix} s\theta_3 s\theta_2 s\theta_1 + c\theta_3 c\theta_1 & s\theta_3 c\theta_2 & s\theta_3 s\theta_2 c\theta_1 - c\theta_3 s\theta_1 \\ c\theta_3 s\theta_2 s\theta_1 - s\theta_3 c\theta_1 & c\theta_3 c\theta_2 & c\theta_3 s\theta_2 c\theta_1 + s\theta_3 s\theta_1 \\ c\theta_2 s\theta_1 & -s\theta_2 & c\theta_2 c\theta_1 \end{bmatrix} \begin{bmatrix} E_1 \\ E_2 \\ E_3 \end{bmatrix} \quad (4.19)$$

The shorthand notation $c\theta_i = \cos\theta_i$ and $s\theta_i = \sin\theta_i$ are used in Eqn (4.19). Given $\{E_1, E_2, E_3\}, \{e_1, e_2, e_3\}$ and specifying axis rotation sequence as 2-1-3, Euler angles $(\theta_1, \theta_2, \theta_3)$ can be calculated from a function in Matlab called “rotm2eul”. The Euler rate $(\dot{\theta}_1, \dot{\theta}_2, \dot{\theta}_3)$ in frame k^{th} can be solved from Eqns (4.20). Each of Euler angle sequences has singularities at certain values of the second angle. The Euler angle sequences where no index is repeated (3-2-1, 2-1-3, etc.) all have a singularity when the second angle, θ_2 , has the value $\theta_2 = \{\frac{\pi}{2}, \frac{3\pi}{2}\}$. In the experiment, if the singularities happened in k^{th} frame, the data from the frame was skipped and $\dot{\theta}_i$ was calculated between $(k-1)^{th}$ and $(k+1)^{th}$. And the time interval became $2 * \Delta t$. By applying the Houbolt method, we get

$$\begin{pmatrix} \dot{\theta}_1^k \\ \dot{\theta}_2^k \\ \dot{\theta}_3^k \end{pmatrix} = \begin{pmatrix} (\frac{1}{6\Delta t})(11\theta_1^k - 18\theta_1^{k-1} + 9\theta_1^{k-2} - 2\theta_1^{k-3}) \\ (\frac{1}{6\Delta t})(11\theta_2^k - 18\theta_2^{k-1} + 9\theta_2^{k-2} - 2\theta_2^{k-3}) \\ (\frac{1}{6\Delta t})(11\theta_3^k - 18\theta_3^{k-1} + 9\theta_3^{k-2} - 2\theta_3^{k-3}) \end{pmatrix} \quad (4.20)$$

Finally, the angular velocity in the body and reference frame were determined from Eqn (4.21,4.22) with a third-order approximation.

$$\begin{pmatrix} \omega_x \\ \omega_y \\ \omega_z \end{pmatrix}^{body} = \begin{bmatrix} c\theta_2 s\theta_3 & c\theta_3 & 0 \\ c\theta_2 c\theta_3 & -s\theta_3 & 0 \\ -s\theta_2 & 0 & 1 \end{bmatrix} \begin{pmatrix} \dot{\theta}_1 \\ \dot{\theta}_2 \\ \dot{\theta}_3 \end{pmatrix} \quad (4.21)$$

$$\begin{pmatrix} \omega_X \\ \omega_Y \\ \omega_Z \end{pmatrix}^{ref} = \begin{bmatrix} 0 & c\theta_1 & c\theta_2 s\theta_1 \\ 1 & 0 & -s\theta_2 \\ 0 & -s\theta_1 & c\theta_2 c\theta_1 \end{bmatrix} \begin{pmatrix} \dot{\theta}_1 \\ \dot{\theta}_2 \\ \dot{\theta}_3 \end{pmatrix} \quad (4.22)$$

in which $c\theta_i = \cos\theta_i$ and $s\theta_i = \sin\theta_i$.

Calculation for Velocity

The time interval Δt between each frame is equal to $\frac{1}{120} \text{ sec}$. And all positions (x, y, z) of markers have been attained from image processing. By applying the Houbolt method, we calculate velocities v_x, v_y, v_z from the displacement between the frame k^{th} and frame $(k-3)^{th}$ with a third-order approximation.

$$v_x^k = \left(\frac{1}{6\Delta t}\right)(11v_x^k - 18v_x^{k-1} + 9v_x^{k-2} - 2v_x^{k-3}) \quad (4.23)$$

$$v_y^k = \frac{(11v_y^k - 18v_y^{k-1} + 9v_y^{k-2} - 2v_y^{k-3}) + \frac{6}{2}g(\Delta t)^2}{6\Delta t} \quad (4.24)$$

$$v_z^k = \left(\frac{1}{6\Delta t}\right)(11v_z^k - 18v_z^{k-1} + 9v_z^{k-2} - 2v_z^{k-3}) \quad (4.25)$$

in which (x_G, y_G, z_G) is from Eqn (4.13), $\Delta t = \frac{1}{120} \text{ sec}$ and $g = 9.81 \text{ m/s}^2$. Note that point G in Figure (4.20) is the centroid of object and v_x, v_y, v_z are the velocities calculated at center of object.

4.2.6 Flow Chart for a Single Impact Test

The flow chart for calculating the impact parameters is shown in Figure (4.23). The analysis for a single impact test is completed.

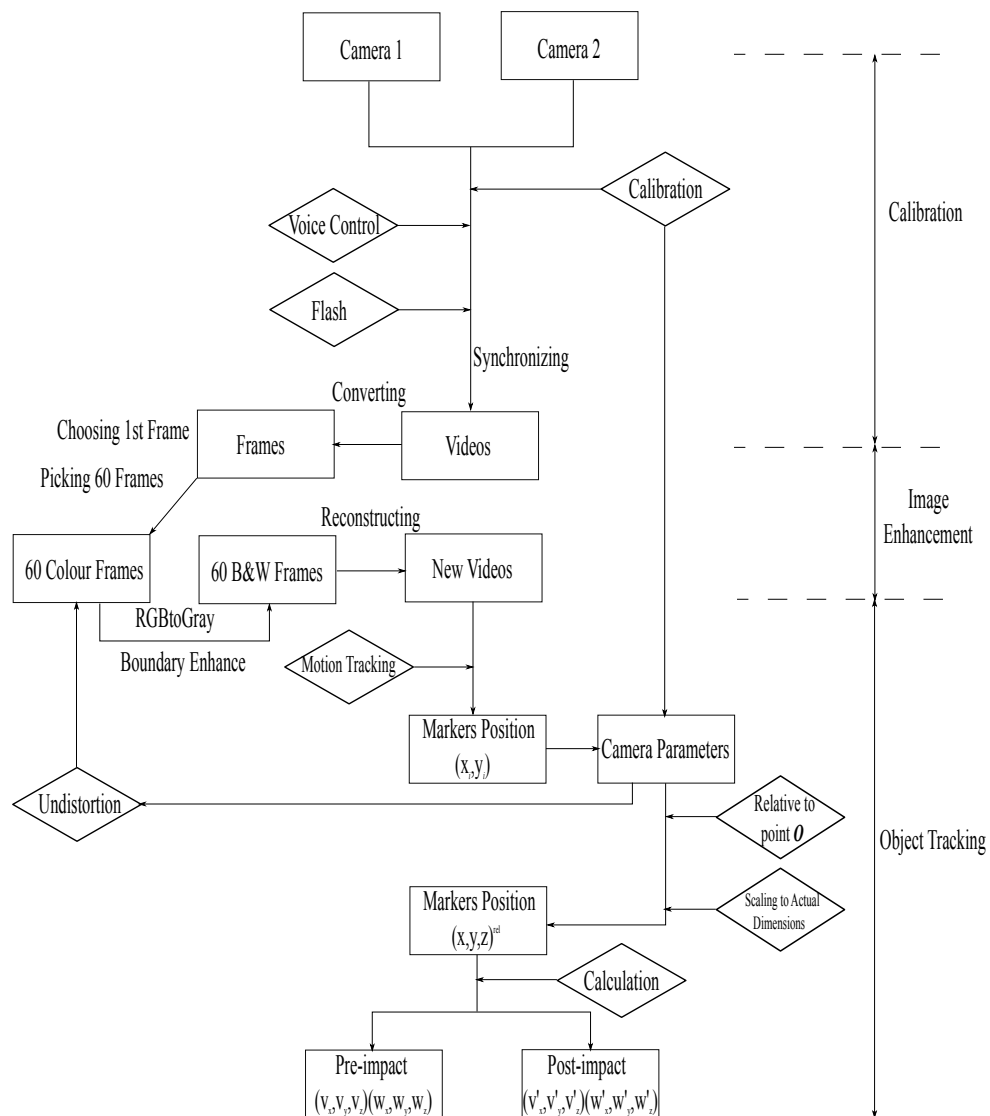


Figure 4.23: Flow chart for one impact test

4.3 Error Analysis

Properly reporting an experimental result along with its uncertainty allows us to make judgments about the quality of the experiment, and it facilitates meaningful comparisons with theoretical or numerical simulation results [67].

Measurement errors can be classified as either random or systematic, depending on how the measurement was obtained (an instrument could cause a random error in one situation and a systematic error in another). Random errors are statistical fluctuations (in either direction) in the measured data due to the precision limitations of the measurement device. And systematic errors are reproducible inaccuracies that are consistently in the same direction.

When making careful measurements, the goal is to reduce as many sources of error as possible and to keep track of those errors that we can not eliminate. It is useful to know the types of errors that may occur, so that we may recognize them when they arise. The sources of error in our 3D rigid-body impact experiments include:

1. Incomplete definition (random) — Although two cameras focus at the same reference object, the focus can be changed due to the auto-focus function. This can effect the intrinsic matrix K of the camera and the actual positions of the object. In order to minimize this uncertainty, the focus is set onto reference point before test started and checkerboard pattern and objects are placed no more than 400 *mm* away from reference point.
2. Instrument resolution (random) — The angle ruler and laser level have the smallest scale of 1 with uncertainty(± 0.5). The resolution of image is $1280 * 720$ pixels and has the smallest scale of 1 pixel with uncertainty(± 0.5 pixel). Ruler used in measuring dimensions of object has the smallest scale of 1*mm* with uncertainty($\pm 0.5*mm*). Time interval in video recording has the smallest scale of $\frac{1}{120}$ *sec* with uncertainty($\pm \frac{1}{240}$ *sec*).$
3. Calibration (systematic) — The calibration of an instrument need to be checked before taking data. According to Table (4.3), camera 1 had a mean error of 0.4686

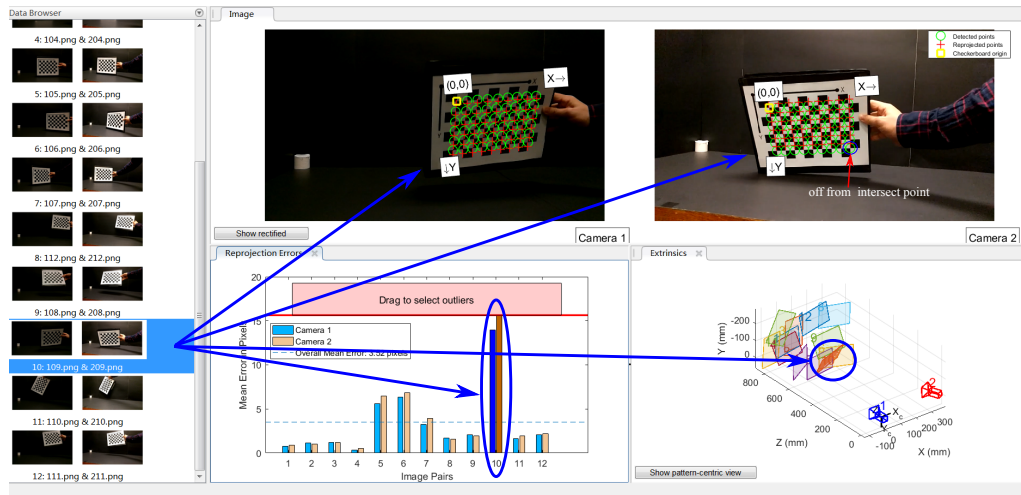


Figure 4.24: Large error occurs when object placed in large angle

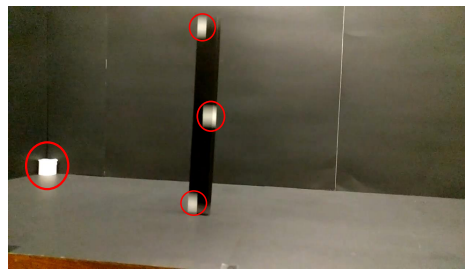


Figure 4.25: Example of blurry marker boundary

pixels and camera 2 had a mean error of 0.3992 pixels after image undistortion process. However, the error became larger when objects placed at an larger angle shown in Figure (4.24), specially when the angle is more than 45 degrees relative to the camera plane. To avoid this type of error, more cameras maybe needed to reduce the chance of large angles relative to the camera plane.

4. Lag time and hysteresis (systematic) — Due to the limitation of the camera for recording images in such a short time period($\frac{1}{120}sec$), part of the marker boundary may become blurry. Figure (4.25) shows blurry boundary of moving markers and clear boundary of reference point which was still. When measuring the location of marker boundary centroids, the uncertainty is ± 1.5 pixels.
5. Repeatability (test-retest reliability) — To evaluate the reliability of our experimental system, we conduct the experiment with same configurations 5, 10 and

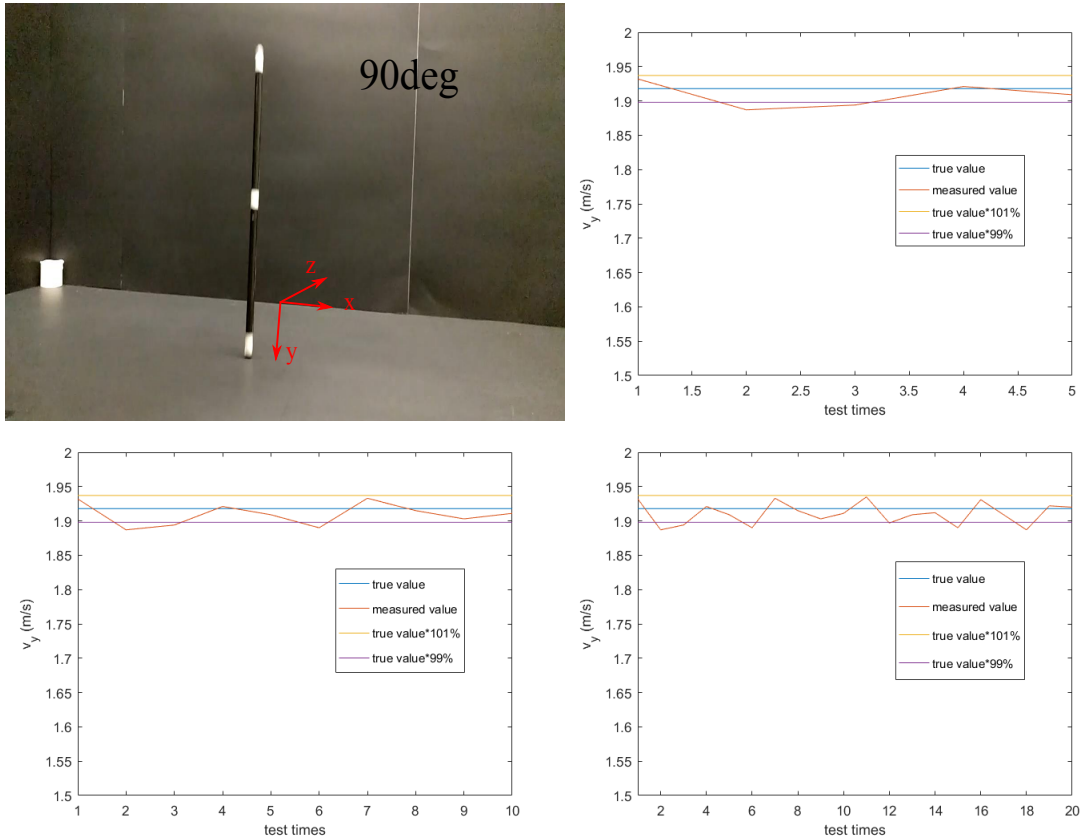


Figure 4.26: Repeatability test on same experiment configurations

20 times as shown in Figure (4.26). It shows that our measurement is repeatable since the variability of test is less than 1.0%.

In the experiment, the cylinder (reference point) is always still during video recording. Its actual position compared to camera 1, as shown in Figure (4.27), can be set as a true value in the measurement. The actual position is

$$x = -421 \pm 0.5mm \quad (4.26)$$

$$y = 142 \pm 0.5mm \quad (4.27)$$

$$z = 912 \pm 0.5mm \quad (4.28)$$

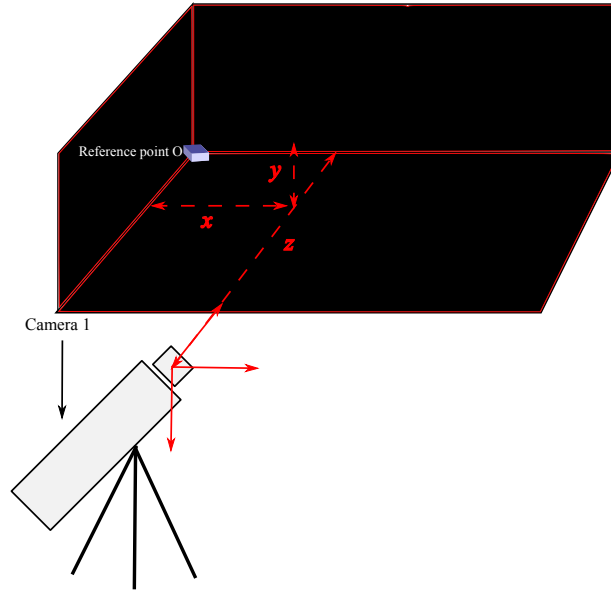


Figure 4.27: Relative position (x, y, z) of reference point to camera 1

Position calculated for camera is

$$x = -419 \pm 2.5mm \quad (4.29)$$

$$y = 141 \pm 2.5mm \quad (4.30)$$

$$z = 918 \pm 2.5mm \quad (4.31)$$

The overall error for the experiment is between 0.03% to 2.82% with uncertainty($\pm 3mm$).

4.4 Experiment Results for Coefficients of Friction and Restitution

4.4.1 Measuring Coefficients of Friction μ_s and μ_k

Dry friction is the force resisting lateral motion between two solid surfaces in contact. It can be divided into static and kinetic friction. Static friction is the force experienced when there is no relative motion between the two surfaces and kinetic friction is the force experienced when the surfaces are moving relative to each other. The commonly

used value is the coefficient of friction (COF), which describes the ratio of the frictional force between the surfaces of the two bodies, and the force pressing them together.

Measurement for Static Friction Coefficient μ_s

As shown in Figure (4.28), the thickness of the slope is $20mm$ and the object is placed on an incline with angle θ . The incline is increased and the angle θ at which sliding begins is recorded. The static friction coefficient μ_s is measured when the test object starts to slide down from the slope. From FBD for sliding condition, $\mu_s N - W \sin(\theta) = 0$, we will get $\mu_s W \cos(\theta) - W \sin(\theta) = 0$. So μ_s is estimated as

$$\mu_s = \sin\theta / \cos\theta \quad (4.32)$$

Two methods are imposed to measure the angle of incline θ . The first method is to use angle ruler to measure θ directly as shown in the top of Figure (4.28). The second one is to use the ratio of two sides (a and c) of the right triangle to measure the sine of θ , $\sin(\theta) = \frac{a}{c}$, as shown in the bottom of Figure (4.28).

For the rod, $a = 69.5mm$ and $c = 281mm$. The angle of incline θ measured from angle ruler is 14 ± 0.2 . So the static friction coefficient for the rod is

$$\mu_s = \sin 14.1 / \cos 14.1 = 0.251 \quad (4.33)$$

For the bar, $a = 71.5mm$ and $c = 283mm$. The angle of incline θ is 14.7 ± 0.2 . So the static friction coefficient for the bar is

$$\mu_s = \sin 14.7 / \cos 14.7 = 0.262 \quad (4.34)$$

Measurement for Kinetic Friction Coefficient μ_k

As shown in Figure (4.29), the thickness of the slope is $20mm$ and the object is placed on an incline with angle θ . The incline is increased and the angle at which sliding begins is recorded. From FBD for sliding condition, $W \sin(\theta) - \mu_k N = \frac{W}{g}a$, in which a is the

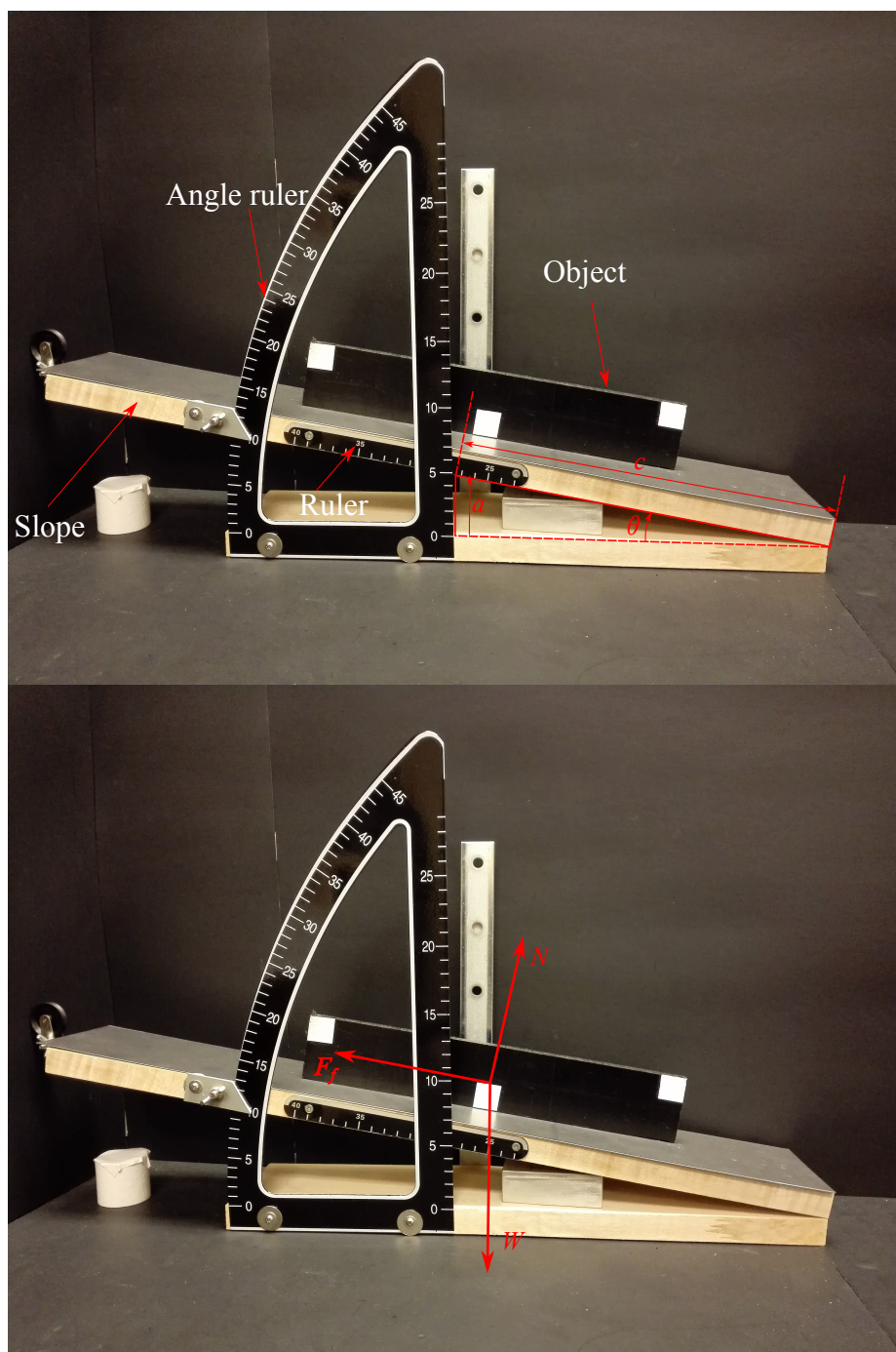


Figure 4.28: Measuring static friction coefficient μ_s

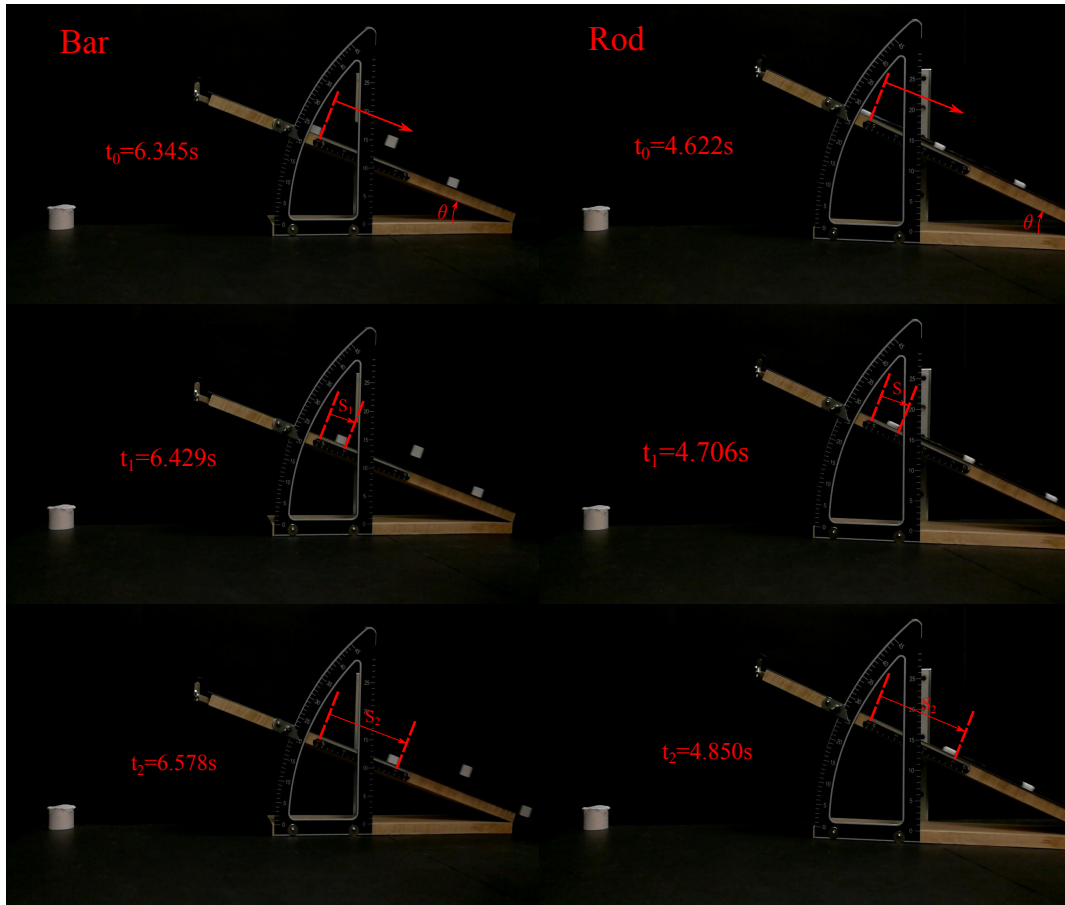


Figure 4.29: Measuring kinetic friction coefficient μ_k

acceleration of the object, we will get $g \sin(\theta) - \mu_k g \cos(\theta) = a$. So μ_k is estimated as

$$\mu_k = \frac{\sin(\theta)}{\cos(\theta)} - \frac{a}{g \cos(\theta)} \quad (4.35)$$

For the bar, in time periods $\Delta t_1 = 6.429 - 6.345 = 0.084 \text{ secs}$ and $\Delta t_2 = 6.578 - 6.345 = 0.233 \text{ secs}$, we get the displacements

$$S_1 = v_0 \Delta t_1 + 0.5 a \Delta t_1^2 = 50 \text{ mm} \quad (4.36)$$

$$S_2 = v_0 \Delta t_2 + 0.5 a \Delta t_2^2 = 150 \text{ mm} \quad (4.37)$$

The acceleration of the bar is

$$a = \frac{2(S_2\Delta t_1 - S_1\Delta t_2)}{\Delta t_1\Delta t_2(\Delta t_2 - \Delta t_1)} = 0.652 \quad (4.38)$$

Substituting a and $\theta = 20$ into Eqn. (4.35), the kinetic friction coefficient for the bar is

$$\mu_k = 0.243 \quad (4.39)$$

By following the same procedure, the kinetic friction coefficient for the rod is

$$\mu_k = 0.229 \quad (4.40)$$

4.4.2 Measuring Coefficient of Restitution e_n

As discussed in Chapter 2, the Stronge's model of COR is the best model for our two-dimensional simulation and experiments. In Stronge's model, based on the internal energy dissipation hypothesis, e_n , as shown in Eqn (4.41), is defined as the square root of the ratio of energy released during restitution to the energy absorbed during compression in normal direction[17, 18].

$$e_n^2 = \frac{W_r}{-W_c} \quad (4.41)$$

$$W_r = 0.5 * m * (v_y^r + \omega_z^r R_x - \omega_x^r R_z)^2 \quad (4.42)$$

$$W_c = -0.5 * m * (v_y^c + \omega_z^c R_x - \omega_x^c R_z)^2 \quad (4.43)$$

Where v_y^c and v_y^r are the velocities at the end of compression and end of restitution at the contact point which is marker 1 in the experiment, respectively. A simple drop test, shown in Figure (4.30), was conducted to find out the values of COR for different objects. In the test, $\omega_z^c = \omega_z^r = \omega_x^r = \omega_x^c = 0$ and the dropped object's orientation is vertical. For one-dimensional motion, Eqn (4.41) can be simplified as

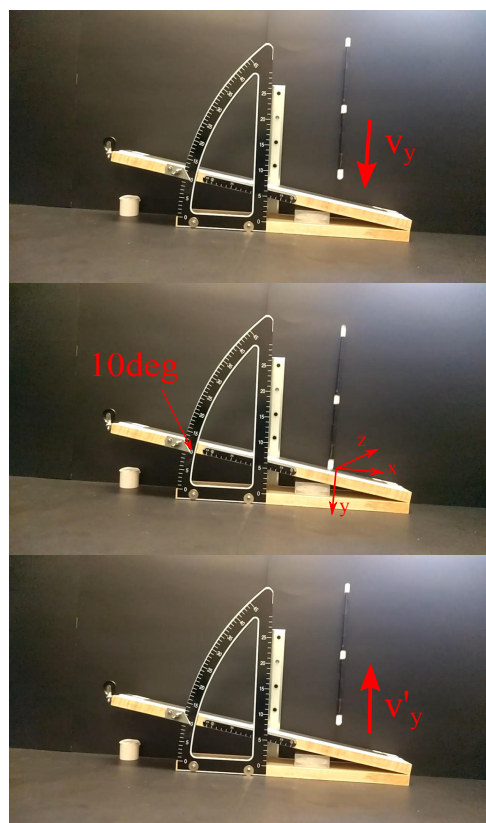


Figure 4.30: Drop test for measuring e_n

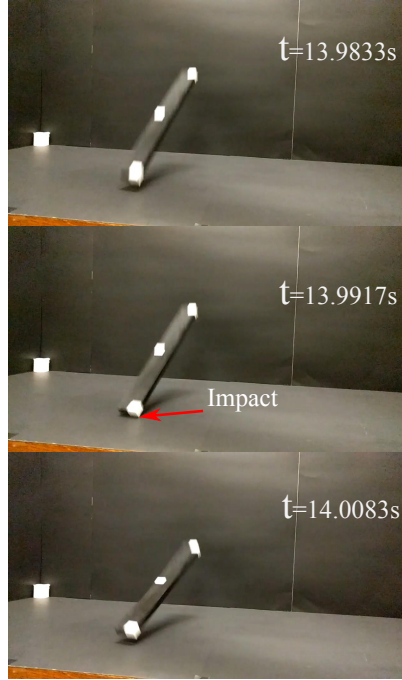


Figure 4.31: Impact example of a bar colliding with ground

$$e_n = \frac{-v'_y}{v_y} \quad (4.44)$$

For the rod, the coefficient of restitution $e_n = \frac{-(-0.562)m/s}{1.923m/s} = 0.292$.

For the bar, the coefficient of restitution $e_n = \frac{-(-0.881)m/s}{1.923m/s} = 0.458$.

4.4.3 Assumptions on Experimental Results

In Chapter 2, our basic assumption is that during the small time interval the positions and angle orientations of all bodies remain unchanged, since all velocities remain finite. To verify this, we conducted a test illustrated in Figure (4.31) on angled drop. The recorded images in Figure (4.30) show that impact happened in a very short time ($\Delta t = \frac{1}{120} \text{sec}$) and the object remained the same orientation. This indicates the assumption that the orientation angles (β, γ, δ) and Euler angles $(\theta_1, \theta_2, \theta_3)$ remain unchanged during the impact.

4.5 Comparison With Numerical Simulation Results

We have presented a numerical algorithm and an experiment for three dimensional rigid body impact. Pre-impact velocity and angular velocity, dimensions and the mass of the object are the parameters given for each impact. The coefficient of restitution e_n and friction coefficient μ_k measured experimentally are also used as inputs in simulation. Once these parameters are entered and the computation completed, the post-impact velocities and angular velocities are determined and compared to the experimental values.

4.5.1 Rod Impact

Six examples of impact from a rod to the ground are presented in Figures (4.32-4.37). These examples show different cases, sticking, sliding or reverse sliding, with different initial conditions. For a quantitative comparison, three frames are selected in each event. A frame comes from before impact and a frame comes from after impact, and the other frame comes from the instant of impact. The pictures shown are taken from camera 2 and time interval between each frame is $\frac{1}{120}$ second. Pre- and post-impact dynamic quantities from centroid of object are listed in Tables (4.4,4.5).

Experiment A shows a free drop for the rod when the slope angle is set to 10. In Figure (4.32), no sliding or reverse sliding occurred during impact. This example shows the sticking mode in frictional impact and is used to calculate the value of the restitution coefficient.

Experiment B shows the sliding mode when the slope angle is set to 45 during the impact. In Figure (4.33), the rod starts from sliding and continues to slide throughout the compression and restitution stages. And the direction of friction force remains the same during the impact.

Experiment C shows the reverse sliding mode when the slope angle is set to 70 during the impact. In Figure (4.34), the rod slides down the slope at the beginning of impact. It ends sliding and begins reverse sliding during the impact. In this case, the direction of friction force changes during the impact.

Experiment D shows the sticking mode when the rod is dropped from side with the

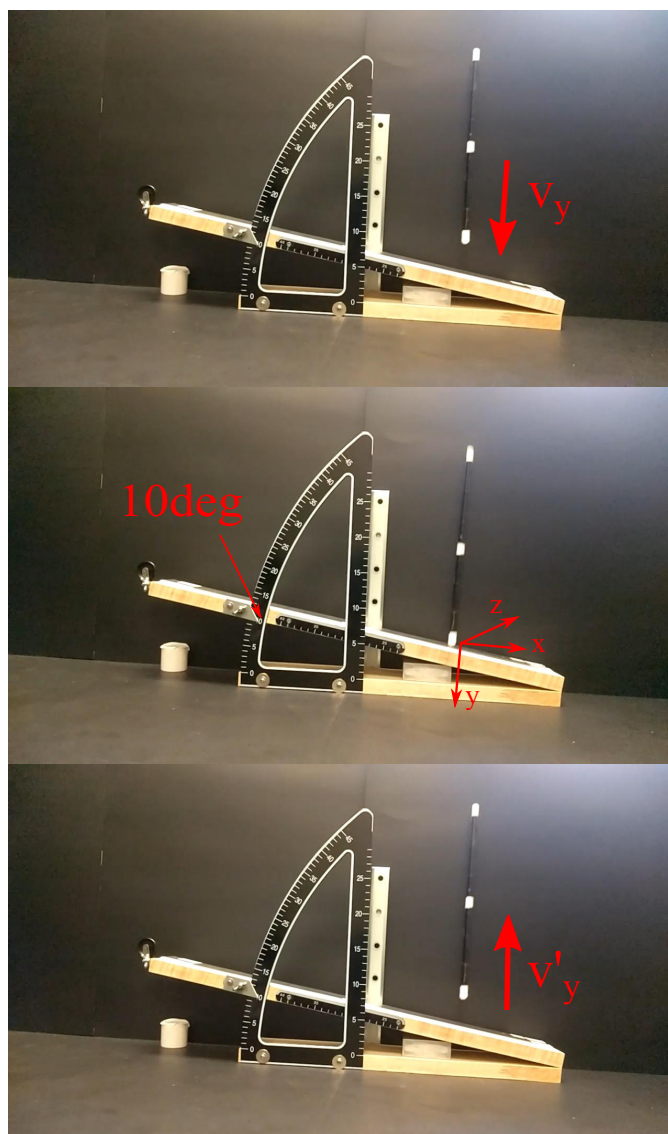


Figure 4.32: Example A for rod

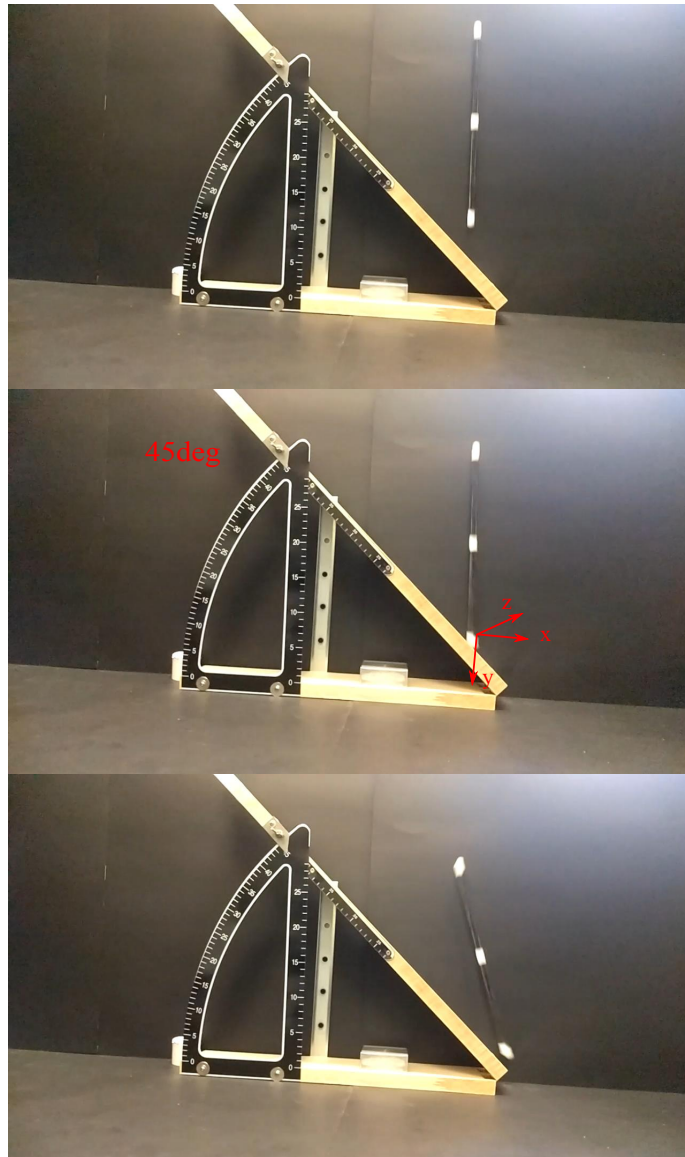


Figure 4.33: Example B for rod

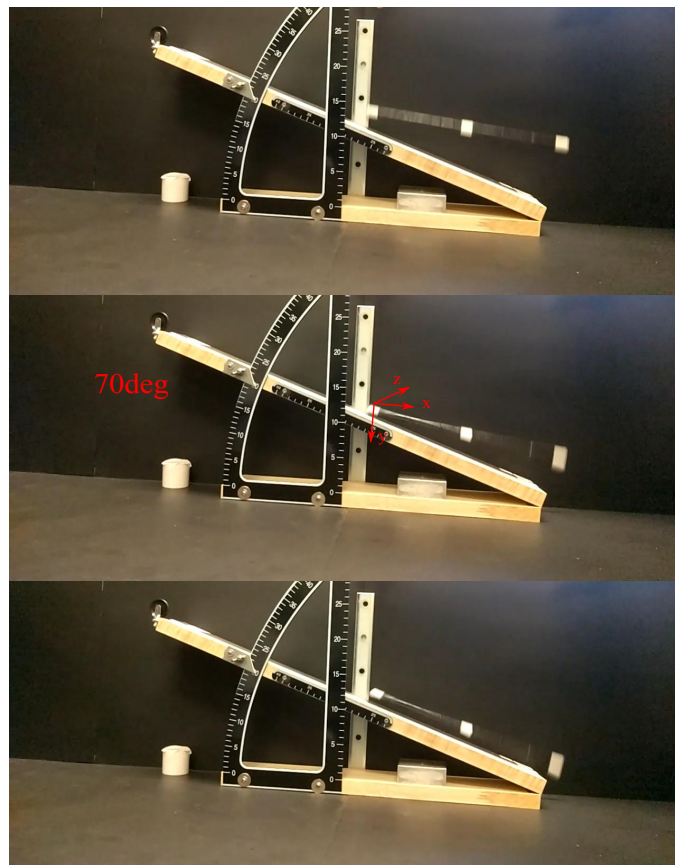


Figure 4.34: Example C for rod

Experiments	Pre-impact dynamic quantities	Post-impact dynamic quantities
	$(v_x, v_y, v_z)(m/s)$	$(v'_x, v'_y, v'_z)(m/s)$
	$(\omega_x, \omega_y, \omega_z)(rad/s)$	$(\omega'_x, \omega'_y, \omega'_z)(rad/s)$
EX. A	$(-0.07, 1.92, 0.08)$	$(-0.06, -0.56, 0.01)$
	$(0.12, 0.09, 0.07)$	$(0.02, 0.02, -0.39)$
EX.B	$(-0.03, 1.72, 0.13)$	$(0.55, 0.91, 0.08)$
	$(0.04, 0.24, 0.11)$	$(-0.22, 0.08, -15.1)$
EX.C	$(-0.07, 1.86, 0.17)$	$(-0.36, 0.61, 0.08)$
	$(0.02, 0.25, 0.05)$	$(-0.24, 0.19, 13.4)$

Table 4.4: Pre- and post-impact dynamic quantities for different tests on rod

Experiments	Pre-impact dynamic quantities	Post-impact dynamic quantities
	$(v_x, v_y, v_z)(m/s)$	$(v'_x, v'_y, v'_z)(m/s)$
	$(\omega_x, \omega_y, \omega_z)(rad/s)$	$(\omega'_x, \omega'_y, \omega'_z)(rad/s)$
EX.D	(0.05, 1.92, 0.07)	(−0.34, 0.87, 0.21)
	(0.04, −0.02, 0.05)	(−3.88, −0.33, −4.14)
EX.E	(0.02, 1.72, 0.04)	(0.37, 0.43, −0.26)
	(0.13, 0.03, 0.02)	(−11.8, 0.41, −15.8)
EX.F	(−0.05, 1.55, 0.06)	(−0.28, 0.24, 0.31)
	(0.06, 0.11, 0.08)	(−14.6, 1.47, −12.8)

Table 4.5: Pre- and post-impact dynamic quantities for different tests on rod

slope angle set to 10. With this setup of the slope, we have two initial velocities v_x and v_z instead of one initial velocity v_x in the previous experiment A, B and C. In Figure (4.35), no sliding or reverse sliding occurred during impact.

Experiment E shows the sliding mode when the rod is dropped from side with the slope angle set to 45. In Figure (4.36), the rod starts from sliding and continues to slide throughout the compression and restitution stages. The friction force is acting along x^- and z^+ direction and its direction remains the same during the impact.

Experiment F shows the reverse sliding mode when the rod is dropped from side with the slope angle set to 60. In Figure (4.37), the rod ends sliding and begins reverse sliding during the impact. In this case, The friction force is acting along x^- and z^+ direction but its direction changes during the impact.

The experimental data, as well as the computational results of post-impact dynamic quantities, cases and energy dissipation, are presented in Table (4.6). It shows that our computation model agrees very well with experimental results.

In all cases, the experimental post-impact velocities are identical to the computational results. Larger differences exist between experimental and computation Angular velocities. Because, in our image processing system, larger error occurs when the object rotates at an larger angle in a short amount of time, specially when the angle is more

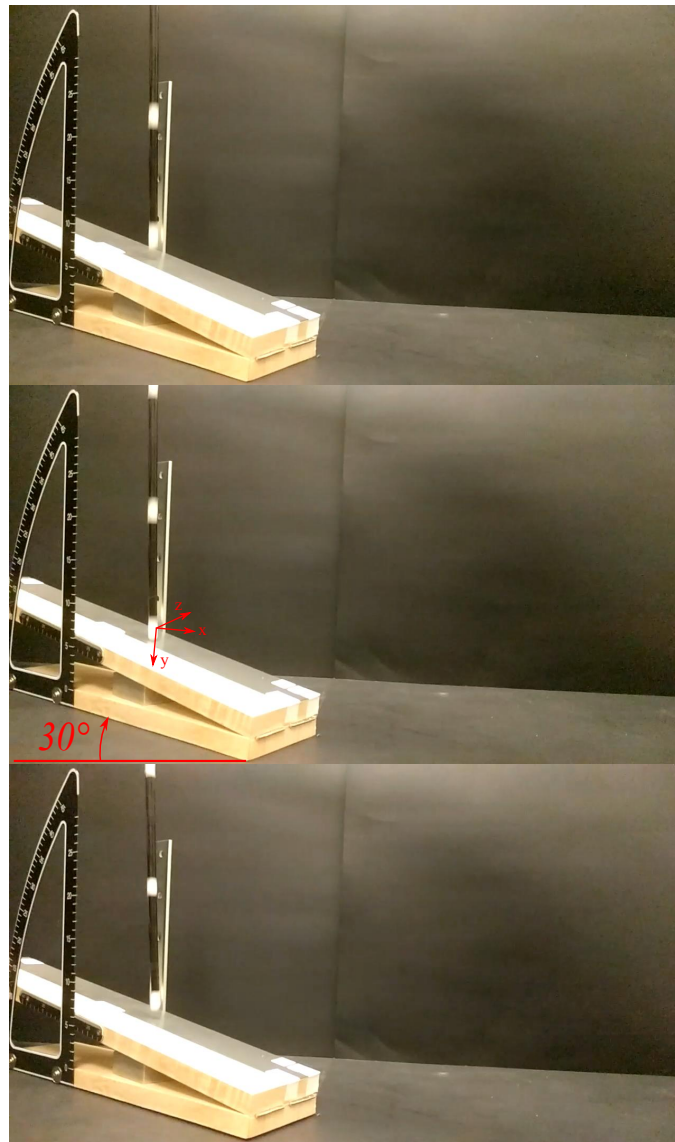


Figure 4.35: Example D for rod

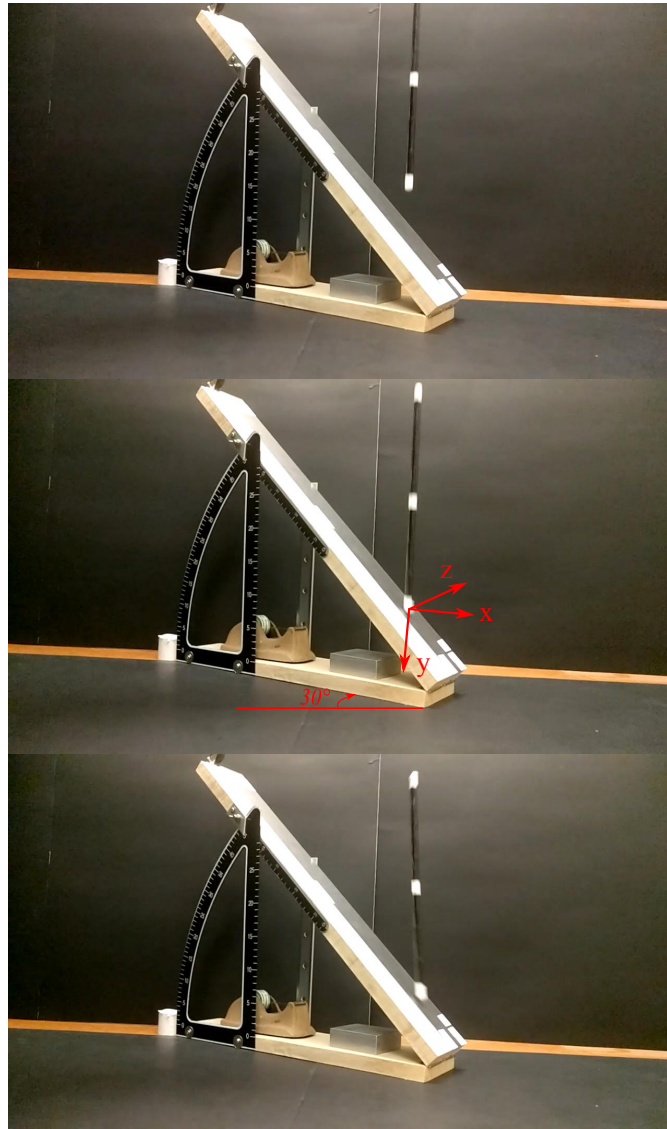


Figure 4.36: Example E for rod

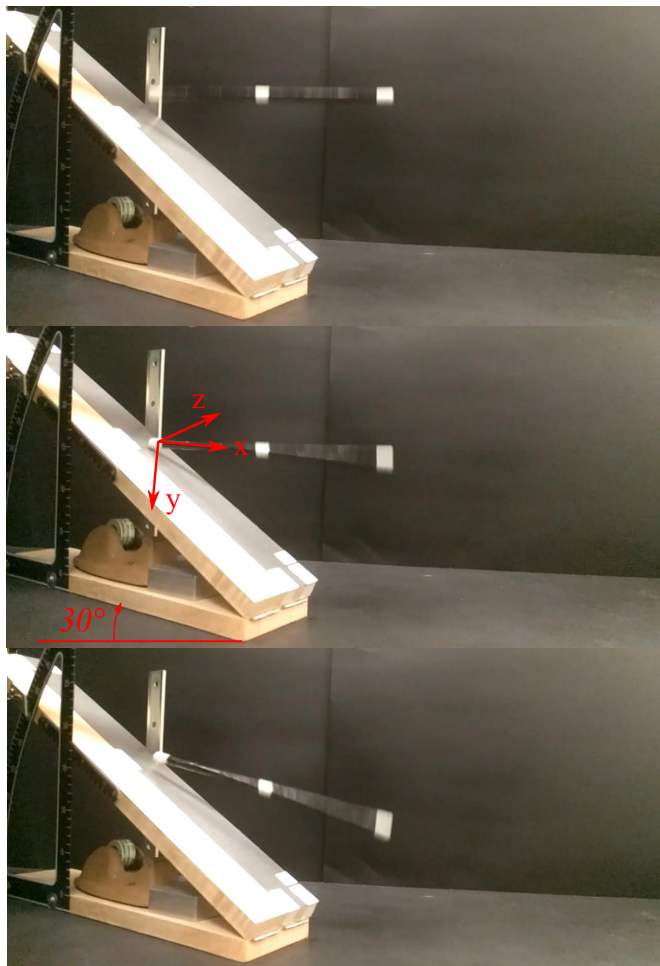


Figure 4.37: Experiments F for rod

Experiments	Post-impact Dynamic Quantities (v_x, v_y, v_z)(m/s) ($\omega_x, \omega_y, \omega_z$)(rad/s)		Case	Energy Dissipation
EX. A	Experiment	(-0.06, -0.56, 0.01) (0.02, 0.02, -0.39)	case #5 (Sticking)	Exp 81.5%
	Computation	(-0.05, -0.52, 0.01) (0.06, -0.02, 0.33)		Comp 81.1%
EX.B	Experiment	(0.55, 0.91, 0.08) (-0.22, 0.08, -15.1)	case #0 (Sliding)	Exp 46.2%
	Computation	(0.55, 0.92, 0.11) (-0.31, 0.02, -15.1)		Comp 47.0%
EX.C	Experiment	(-0.36, 0.61, 0.08) (-0.24, 0.19, 13.4)	case #2 (RSliding)	Exp 67.5%
	Computation	(-0.35, 0.62, 0.11) (-0.15, 0.12, 12.5)		Comp 63.7%
EX.D	Experiment	(-0.34, 0.87, 0.21) (-3.88, -0.33, -4.14)	case #5 (Sticking)	Exp 65.4%
	Computation	(-0.38, 0.87, 0.21) (-3.65, -0.42, -4.35)		Comp 65.8%
EX.E	Experiment	(0.37, 0.43, -0.26) (-11.8, 0.41, -15.8)	case #0 (Sliding)	Exp 41.1%
	Computation	(0.37, 0.42, -0.24) (-11.6, 0.53, -14.9)		Comp 40.9%
EX.F	Experiment	(-0.28, 0.24, 0.31) (-14.6, 1.47, -12.8)	case #2a (RSliding)	Exp 43.2%
	Computation	(-0.25, 0.22, 0.32) (-15.1, 1.64, -13.3)		Comp 45.1%

Table 4.6: Experiment validation for the rod with $\mu_s = 0.251$, $e_n = 0.292$

than 45 degrees relative to the camera plane. The error in energy dissipation varies from 0.5% to 5.6%. The largest difference occurs in reverse sliding cases which is expected as the physics of the impact is more complicated in reverse sliding. This conclusion is also identical to the conclusion reached in two-dimensional impact experimental and computational results comparison.

4.5.2 Rectangle Bar Impact Experiments

Six examples of impact from a bar to the ground are presented in Figures (4.38-4.43). These examples show different cases, sticking, sliding or reverse sliding, with different initial conditions. Pictures were taken from camera 2 and time interval between each frame is $\frac{1}{120}$ second. Pre- and post-impact dynamic quantities from centroid of object

Experiments	Pre-impact dynamic quantities	Post-impact dynamic quantities
	$(v_x, v_y, v_z)(m/s)$	$(v'_x, v'_y, v'_z)(m/s)$
	$(\omega_x, \omega_y, \omega_z)(rad/s)$	$(\omega'_x, \omega'_y, \omega'_z)(rad/s)$
EX. A	$(-0.07, 1.92, 0.08)$	$(-0.13, -0.88, -0.07)$
	$(0.02, 0.09, 0.07)$	$(0.05, -0.05, -0.23)$
EX.B	$(-0.03, 1.72, 0.08)$	$(0.46, 0.96, 0.06)$
	$(0.04, 0.04, 0.11)$	$(0.06, -0.04, -14.3)$
EX.C	$(-0.07, 1.86, 0.10)$	$(-0.11, 0.53, 0.07)$
	$(0.02, 0.12, 0.05)$	$(0.08, -0.11, -17.54)$

Table 4.7: Pre- and post-impact dynamic quantities for different tests on bar

are listed in Table (4.7,4.8).

Experiment A shows a free drop for the bar when the slope angle is set to 10. In Figure (4.38), no sliding or reverse sliding occurred during impact. This example shows the sticking mode in frictional impact and is used to calculate the value of the restitution coefficient.

Experiment B shows the sliding mode when the slope angle is set to 45 during the impact. In Figure (4.39), the bar starts from sliding and continues to slide throughout the compression and restitution stages. And the direction of friction force remains the same during the impact.

Experiment C shows the reverse sliding mode when the slope angle is set to 70 during the impact. In Figure (4.40), the bar slides down the slope at the beginning of impact. It ends sliding and begins reverse sliding during the impact. In this case, the direction of friction force changes during the impact.

Experiment D shows the sticking mode when the bar is dropped from side with the slope angle set to 10. With this setup of the slope, we have two initial velocities v_x and v_z instead of one initial velocity v_x in the previous experiment A, B and C. In Figure (4.41), no sliding or reverse sliding occurred during impact.

Experiment E shows the sliding mode when the rod is dropped from side with the

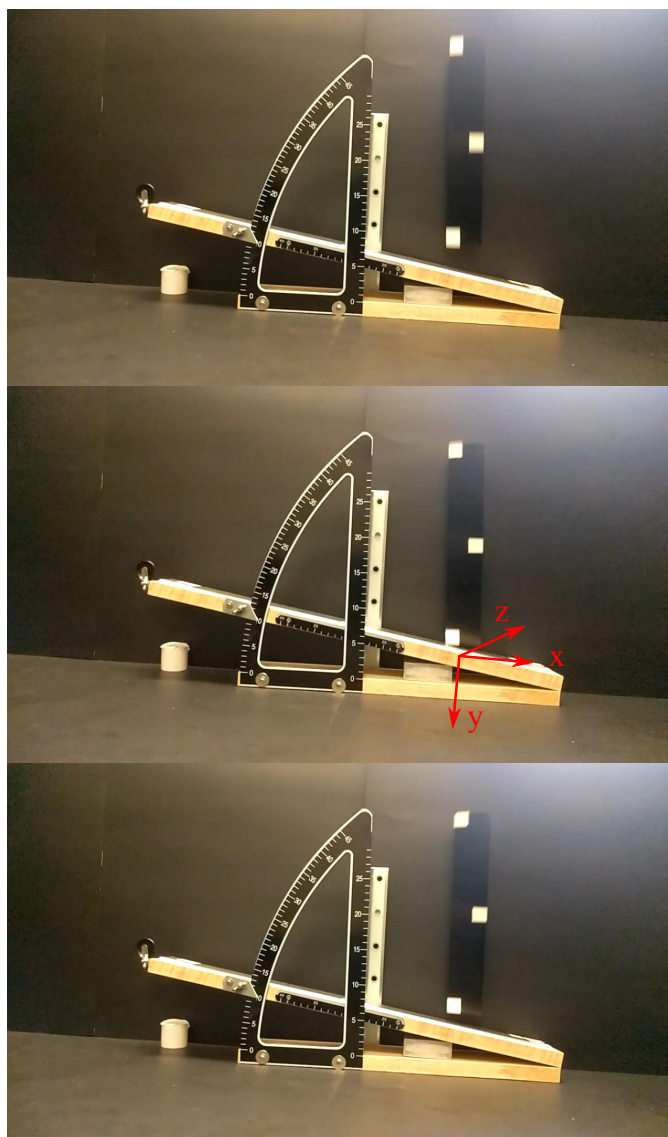


Figure 4.38: Example A for bar

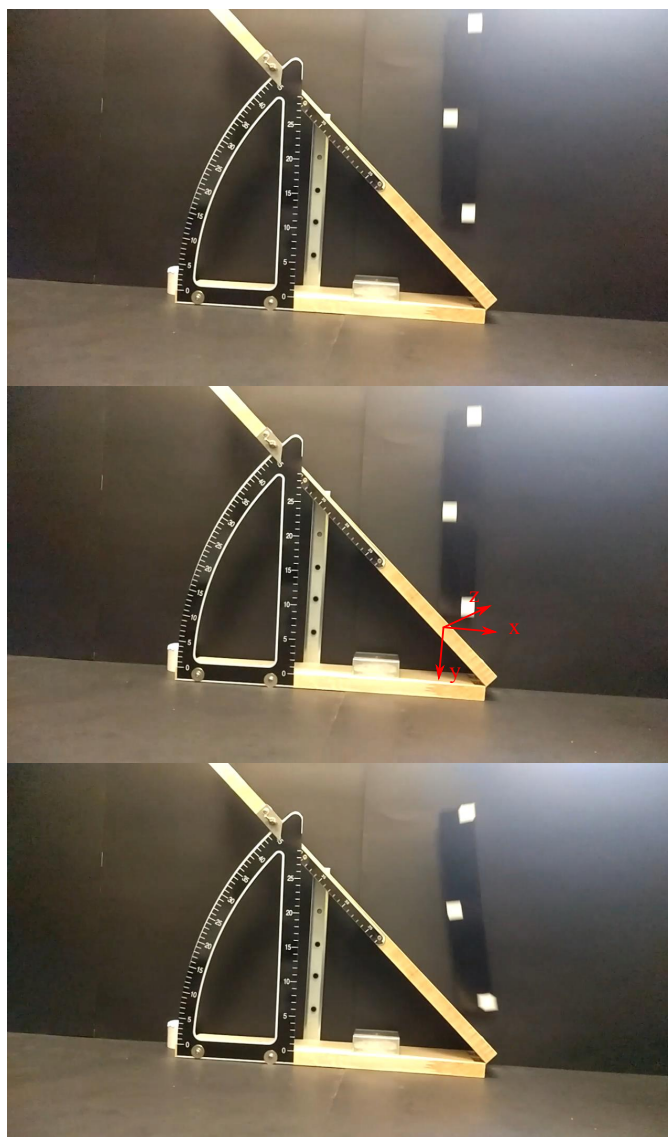


Figure 4.39: Example B for bar

Experiments	Pre-impact dynamic quantities	Post-impact dynamic quantities
	$(v_x, v_y, v_z)(m/s)$	$(v'_x, v'_y, v'_z)(m/s)$
	$(\omega_x, \omega_y, \omega_z)(rad/s)$	$(\omega'_x, \omega'_y, \omega'_z)(rad/s)$
EX.D	(0.05, 1.92, 0.04)	(0.19, -0.74, -0.11)
	(0.04, -0.02, 0.05)	(-0.31, 0.04, 0.82)
EX.E	(0.01, 1.72, 0.04)	(0.69, -0.52, -0.37)
	(0.08, 0.03, 0.02)	(-5.54, 0.50, -13.03)
EX.F	(0.08, 1.55, 0.06)	(-0.63, 0.45, 0.17)
	(0.06, 0.12, 0.08)	(-6.2, 0.27, 13.1)

Table 4.8: Pre- and post-impact dynamic quantities for different tests on bar

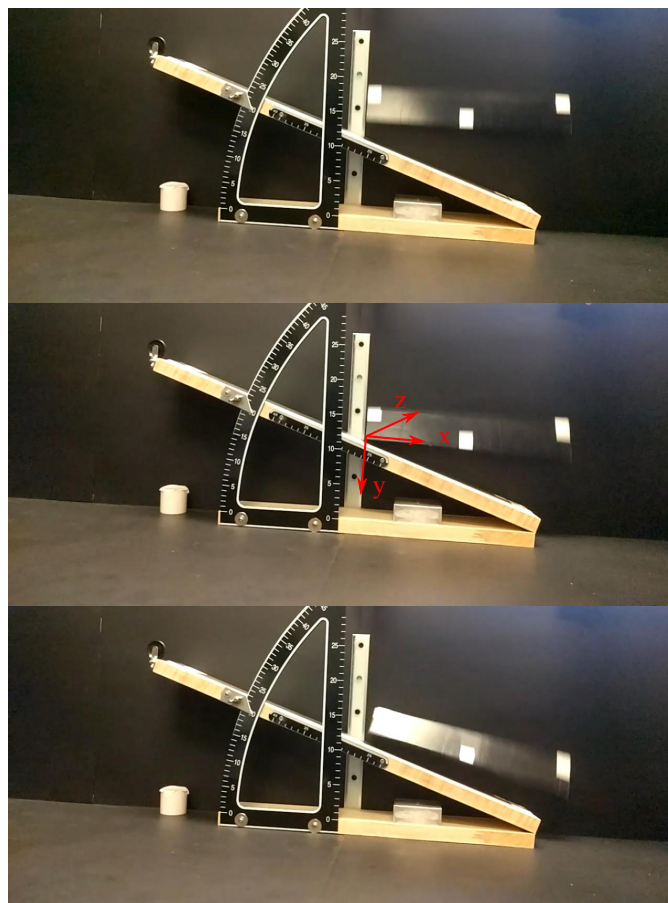


Figure 4.40: Example C for bar

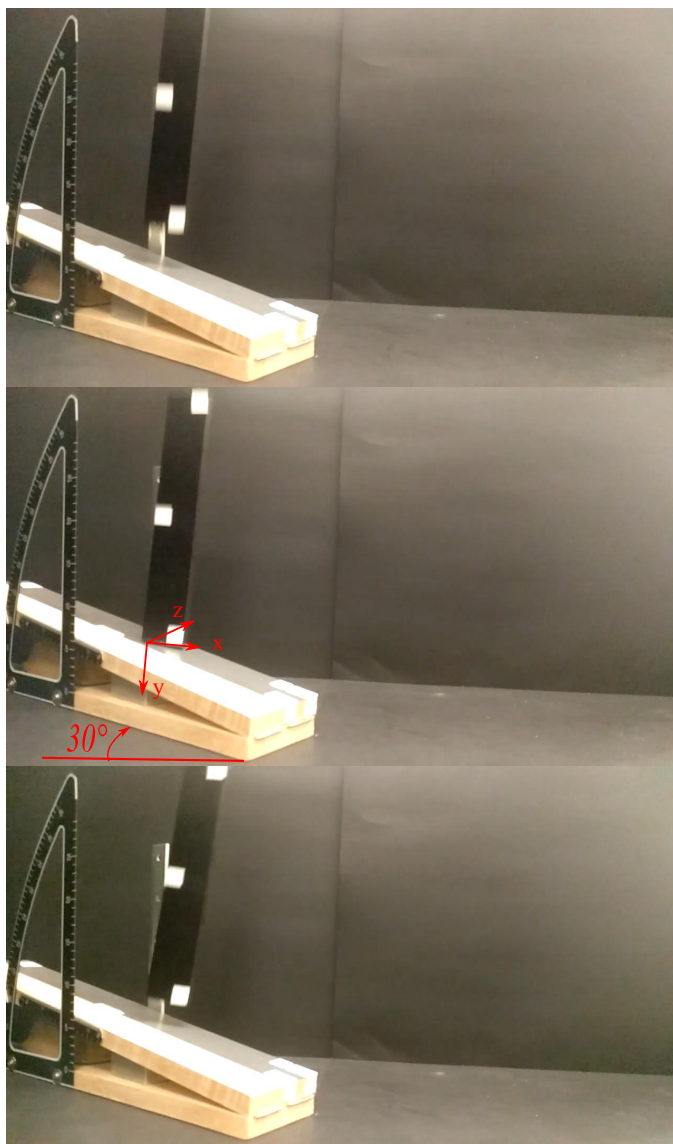


Figure 4.41: Example D for bar

slope angle set to 45. In Figure (4.42), the bar starts from sliding and continues to slide throughout the compression and restitution stages. The friction force is acting along x^- and z^+ direction and its direction remains the same during the impact.

Experiment F shows the reverse sliding mode when the rod is dropped from side with the slope angle set to 60. In Figure (4.43), the bar ends sliding and begins reverse sliding during the impact. In this case, The friction force is acting along x^- and z^+ direction but its direction changes during the impact.

The experimental data, as well as the computational results of these calculations for different objects, are presented in Table (4.9).

In all cases, the experimental post-impact velocities are very close to the computational results. Larger differences exist between experimental and computation Angular velocities. Because, in our image processing system, larger error occurs when the object rotates at an larger angle in a short amount of time, specially when the angle is more than 45 degrees relative to the camera plane. The error in energy dissipation varies from 0.8% to 4.4%. The largest difference occurs in reverse sliding cases which is expected as the physics of the impact is more complicated in reverse sliding. This conclusion is also identical to the conclusion reached in two-dimensional impact experimental and computational results comparison.

Overall, we validate the numerical 3D rigid-body impact model introduced in chapter 3 by comparing it to experimental results in chapter 4. The model is applied in a manner that requires the input of the coefficient of friction and restitution, which are accurately determined through comparison. It shows that our computation model agrees very well with experiment results and the error varies from 0.5% to 5.6%.

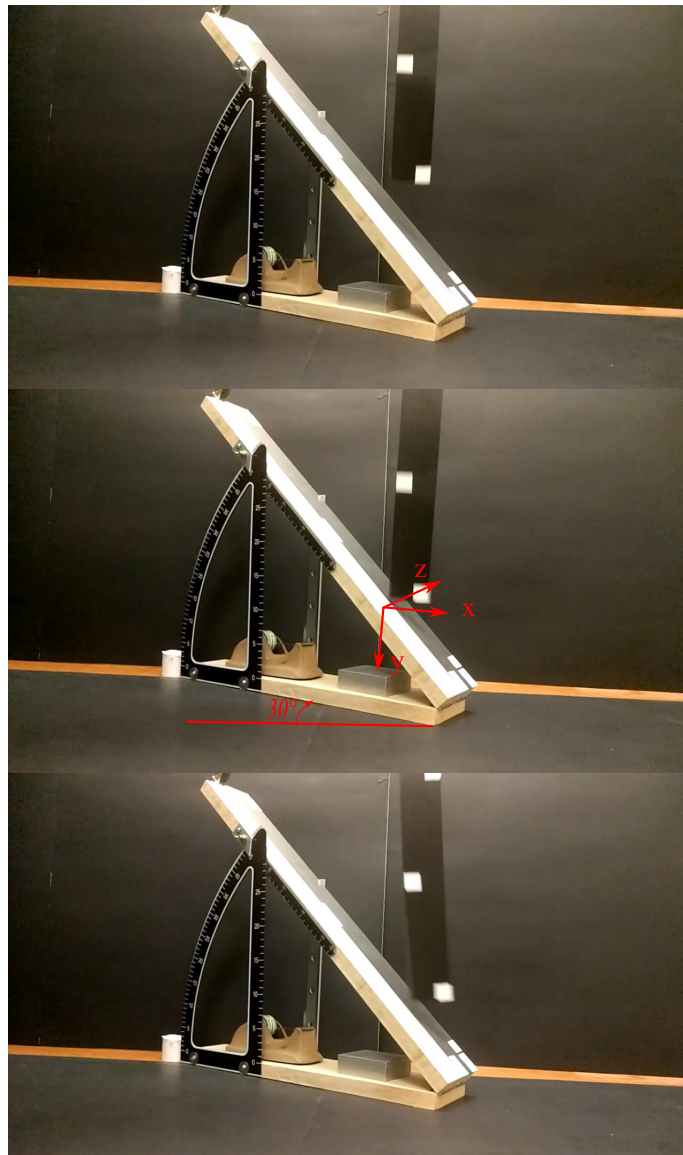


Figure 4.42: Example E for bar

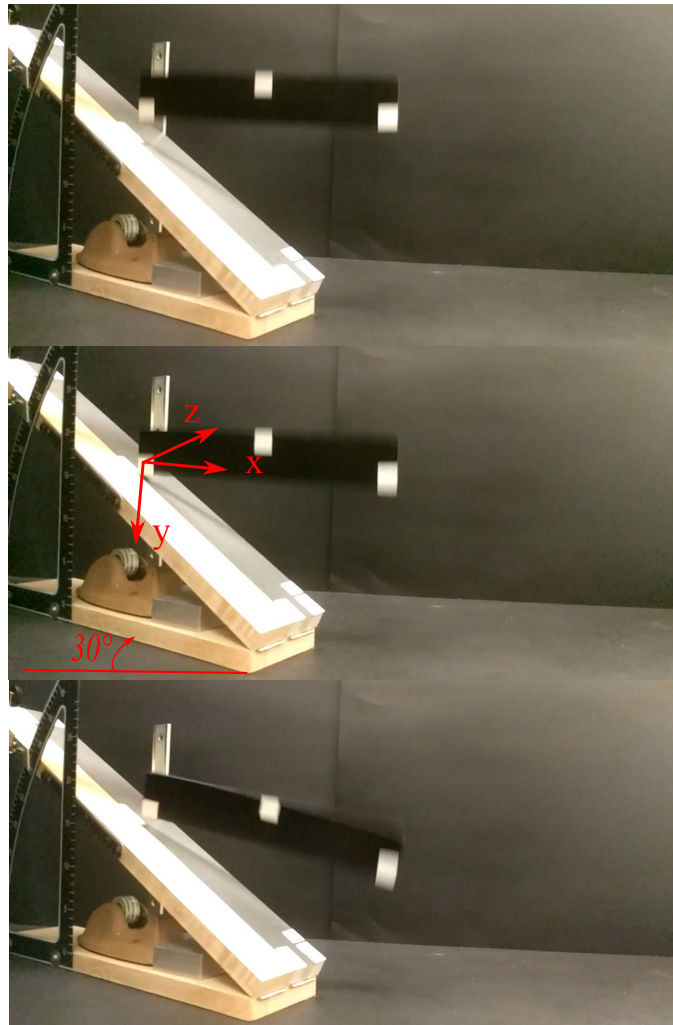


Figure 4.43: Example F for bar

Experiments	Pose-impact Dynamic Quantities		Case	Energy Dissipation
	$(v_x, v_y, v_z)(m/s)$ $(\omega_x, \omega_y, \omega_z)(rad/s)$			
EX. A	Experiment	$(-0.13, -0.88, -0.07)$ $(0.05, -0.05, -0.23)$	case #5 (Sticking)	$\frac{\text{Exp}}{\text{Comp}} \quad \frac{76.5\%}{75.2\%}$
	Computation	$(-0.15, -0.86, 0.03)$ $(0.06, -0.02, -0.31)$		
EX.B	Experiment	$(0.46, 0.96, 0.06)$ $(0.06, -0.04, -14.3)$	case #2.75 (Sliding)	$\frac{\text{Exp}}{\text{Comp}} \quad \frac{56.4\%}{57.7\%}$
	Computation	$(0.46, 1.02, 0.07)$ $(0.05, -0.12, -14.3)$		
EX.C	Experiment	$(-0.11, 0.53, 0.07)$ $(0.08, -0.11, -17.54)$	case #1 (RSliding)	$\frac{\text{Exp}}{\text{Comp}} \quad \frac{38.5\%}{36.8\%}$
	Computation	$(-0.09, 0.52, 0.11)$ $(0.10, -0.12, -16.32)$		
EX.D	Experiment	$(0.19, -0.74, -0.11)$ $(-0.31, 0.04, 0.82)$	case #1 (Sticking)	$\frac{\text{Exp}}{\text{Comp}} \quad \frac{23.5\%}{23.7\%}$
	Computation	$(0.18, -0.74, -0.12)$ $(-0.33, 0.05, 0.78)$		
EX.E	Experiment	$(0.69, -0.52, -0.37)$ $(-5.54, 0.50, -13.03)$	case #0 (Sliding)	$\frac{\text{Exp}}{\text{Comp}} \quad \frac{68.8\%}{67.4\%}$
	Computation	$(0.68, -0.55, -0.33)$ $(-5.60, 0.53, -12.90)$		
EX.F	Experiment	$(-0.63, 0.45, 0.17)$ $(-6.2, 0.27, 13.1)$	case #4c (Rsliding)	$\frac{\text{Exp}}{\text{Comp}} \quad \frac{68.2\%}{64.7\%}$
	Computation	$(-0.63, 0.42, 0.18)$ $(-5.7, 0.12, 14.3)$		

Table 4.9: Experiment validation for the bar with $\mu_s = 0.416$, $e_n = 0.458$

Chapter 5

Conclusions and Future Work

A reliable computational model for analyzing three dimensional rigid-body impact with the ground has been developed in this dissertation. The complicated structure of different objects and slide/stick/reverse slide modes existing on ground suggested that the rigid body impact model should be used, because it provides a better understanding of the dynamic quantities in instantaneous impact than do other more complicated approximations. Nevertheless, three-dimensional experiments were conducted to validate the simulation impact model.

5.1 Summary of Key Results

We started the dissertation with a planar oblique impact by formulating the rigid-body impact model and deriving the post-impact quantities. Dimensionless governing equations were derived for both sliding, reverse sliding and sticking modes. Then these three modes were classified into seven impact cases. By dividing a single impact into compression and restitution stages with seven cases, dynamic quantities and kinetic energy loss for axisymmetric as well as initially irrotational bodies were investigated. We obtained the kinetic energy loss dependence on the impact orientation and the initial angular velocity. This allowed us to specify the initial orientation and angular velocity which would yield the lowest energy loss. Also, 2D experiments were performed to validate our simulation results. With the comparison, a conclusion was reached that simulation results agreed well with experimental results with less than 6% error and Stronge's hypothesis of restitution was the best COR model among Newton's, Poisson's and Stronge's models. Moreover, both results showed that sliding and reverse sliding modes, as opposed to sticking at time of impact lead to more energy dissipation.

We next extended the impact model and experiment in three dimensional rigid-body impact by formulating the governing equations. The seven cases were extended to eleven possible cases. Then the rigid-body impact analysis was concluded with three examples, ball, rod and bar, which validated the use of the two dimensional model for analyzing certain three dimensional impacts. Several examples were presented to study the influence of input parameters such as orientation angles, coefficient of friction and coefficient of restitution on post-impact dynamic quantities, case study and energy dissipation. After the discussion, we concluded that the characteristics of 3D impact follow closely those of as two-dimensional impact.

The models developed were compiled in a simulation code capable of analyzing objects colliding with the ground in three-dimensional space. A three-dimensional experiment was conducted to validate the computational impact model. The values of friction coefficients μ_s and μ_k and coefficient of restitution e_n were treated as constant values during impact and they were measured before the impact tests. For processing of impact image, we developed Matlab programs for image enhancement and motion capture. After the positions of markers were collected and calculated into displacements. The Houbolt method, which is generally referred to as a third-order approximation for velocity and acceleration, was used to interpret the pre- and post-impact velocity and angular velocity from displacement measurements. Also, an error analysis was performed to study the accuracy of the experiment. Random or systematic measurement errors were stated with uncertainty to quantify the range of errors. With the comparison between experiment and computational modeling, we observed that the simulation predictions were quite close to the experimental results with less than 10% error in the dissipation energy thereby validating our analysis.

In summary, the tasks accomplished in this work are important steps toward the understanding of complex impact problems. The analytical tools provide quantitative prediction capabilities, and can be further used to study the problems with in-depth understanding. A mathematically rigorous model which can be applied in industrial field will be the main goal of future work.

5.2 Future Work

1. Impact mechanics needs an analytical model stemming from physical principles capable of describing the impact of an object with the ground. Considering the pre-impact parameters for a body that travels through air prior to impact requires the analysis of the aerodynamic drag experienced by the object.
2. Our current computational modeling can be extended and applied in Multi-body impacts.
3. Subsequent impacts and the trajectory of objects can be studied.
4. Instead of assuming constant values of coefficient of friction and restitution, a further study on the influence of these two variables can be discussed.
5. An use of computer software to aid in our analysis, such as finite element analysis (FEA) and multibody dynamics (MBD), and optimization, can be used to quantitatively develop our numerical simulation.
6. Following the limitation angles for two camera capturing, more cameras can be applied to get the object positions with better accuracy.
7. The motion capture program can be extended to detect multi-body motion.

Bibliography

- [1] J Wittenburg. *Dynamics of multibody systems*. Springer Berlin, 2008.
- [2] RA Wehage, EJ Haug, and RR Beck. Generalized coordinate partitioning in dynamic analysis of mechanical systems. Technical report, DTIC Document, 1981.
- [3] YA Khulief and AA Shabana. A continuous force model for the impact analysis of flexible multibody systems. *Mechanism and Machine Theory*, 22(3):213–224, 1987.
- [4] ET Whittaker. *A treatise on the analytical dynamics of particles and rigid bodies with an introduction to the problem of three bodies*. CUP Archive, 1970.
- [5] JB Keller. Impact with friction. *Journal of applied Mechanics*, 53(1):1–5, 1986.
- [6] I Han and BJ Gilmore. Multi-body impact motion with friction-analysis, simulation, and experimental validation. *Journal of Mechanical Design*, 115(3):412–422, 1993.
- [7] M Jean. Frictional contact in collections of rigid or deformable bodies: numerical simulation of geomaterial motions. *Studies in Applied Mechanics*, 42:463–486, 1995.
- [8] KH Hunt and FRE Crossley. Coefficient of restitution interpreted as damping in vibroimpact. *J. Appl. Mech.*, 1975.
- [9] H Baruh. *Analytical dynamics*. WCB/McGraw-Hill Boston, 1999.
- [10] RM Brach. *Mechanical impact dynamics: rigid body collisions*. Brach Engineering, LLC, 2007.
- [11] RM Brach. Formulation of rigid body impact problems using generalized coefficients. *International journal of engineering science*, 36(1):61–71, 1998.

- [12] SW Kim, AK Misra, VJ Modi, and X Cyril. Modelling of contact dynamics of two flexible multi-body systems. *Acta Astronautica*, 45(11):669–677, 1999.
- [13] M Ciavarella. The generalized cattaneo partial slip plane contact problem. ii:examples. *International journal of solids and Structures*, 35(18):2363–2378, 1998.
- [14] J Jaeger. Analytical solutions of contact impact problems. *Appl. Mech. Rev*, 47(2):35–54, 1994.
- [15] EJ Routh. *The advanced part of a treatise on the dynamics of a system of rigid bodies*. 1905.
- [16] Y Wang and MT Mason. Two-dimensional rigid-body collisions with friction. *J. Appl. Mech.*, 59:635, 1992.
- [17] WJ Stronge. Rigid body collisions with friction. *Proceedings of the Royal Society of London. Series A: Mathematical and Physical Sciences*, 431(1881):169–181, 1990.
- [18] WJ Stronge. *Impact mechanics*. Cambridge university press, 2004.
- [19] RM Brach. Rigid body collisions. *Journal of Applied Mechanics*, 56(1):133–138, 1989.
- [20] CE Smith. Predicting rebounds using rigid-body dynamics. *Journal of applied mechanics*, 58(3):754–758, 1991.
- [21] SC Wu, SM Yang, and EJ Haug. Dynamics of mechanical systems with coulomb friction, stiction, impact and constraint addition-deletion in spatial systems. *Mechanism and Machine Theory*, 21(5):417–425, 1986.
- [22] YA Khulief and AA Shabana. Impact responses of multi-body systems with consistent and lumped masses. *Journal of Sound and Vibration*, 104(2):187–207, 1986.
- [23] AS Yigit, AG Ulsoy, and RA Scott. Dynamics of a radially rotating beam with impact. i: Theoretical and computational model. *Journal of vibration, acoustics, stress, and reliability in design*, 112(1):65–70, 1990.

- [24] GP Mac Sithigh. Rigid-body impact with friction-various approaches compared. *ASME APPLIED MECHANICS DIVISION-PUBLICATIONS-AMD*, 205:307–307, 1995.
- [25] Y Wang and V Kumar. Simulation of mechanical systems with multiple frictional contacts. *Journal of Mechanical Design*, 116:571, 1994.
- [26] KH Hwang and AA Shabana. Effect of mass capture on the propagation of transverse waves in rotating beams. *Journal of sound and vibration*, 186(3):495–525, 1995.
- [27] CY Wu, LY Li, and C Thornton. Energy dissipation during normal impact of elastic and elastic-plastic spheres. *International Journal of Impact Engineering*, 32(1):593–604, 2005.
- [28] WS Howard and V Kumar. A minimum principle for the dynamic analysis of systems with frictional contacts. In *Robotics and Automation, 1993. Proceedings., 1993 IEEE International Conference on*, pages 437–442. IEEE, 1993.
- [29] H Hertz. *Miscellaneous papers*. Macmillan, 1896.
- [30] W Goldsmith. *Impact, the theory and physical behavior of colliding solids*. 1964.
- [31] T Lee and A Wang. On the dynamics of intermittent motion mechanisms. *ASME Paper*, (82-DET):65, 1982.
- [32] HM Lankarani and PE Nikravesh. A contact force model with hysteresis damping for impact analysis of multibody systems. *Journal of Mechanical Design*, 112(3):369–376, 1990.
- [33] O Ma. Contact dynamics modelling for the simulation of the space station manipulators handling payloads. In *Robotics and Automation, 1995. Proceedings., 1995 IEEE International Conference on*, volume 2, pages 1252–1258. IEEE, 1995.
- [34] SW Kim. *Contact dynamics and force control of flexible multi-body systems*. PhD thesis, McGill University Montreal, Quebec, Canada, 1999.

- [35] W Goldsmith. The theory and physical behavior of colliding solids. *Arnold, London*, 1960.
- [36] D W Marhefka and DE Orin. A compliant contact model with nonlinear damping for simulation of robotic systems. *Systems, Man and Cybernetics, Part A: Systems and Humans, IEEE Transactions on*, 29(6):566–572, 1999.
- [37] YB Jia. Energy-based modeling of tangential compliance in 3-dimensional impact. In *Algorithmic Foundations of Robotics IX*, pages 267–284. Springer, 2011.
- [38] I Han and SU Park. Impulsive motion planning for positioning and orienting a polygonal part. *The International Journal of Robotics Research*, 20(3):249–262, 2001.
- [39] KL Johnson and KL Johnson. *Contact mechanics*. Cambridge university press, 1987.
- [40] CT Lim and WJ Stronge. Oblique elastic–plastic impact between rough cylinders in plane strain. *International Journal for Parasitologyjournal of Engineering Science*, 37(1):97–122, 1999.
- [41] Z Zhao, CS Liu, and B Brogliato. Planar dynamics of a rigid body system with frictional impacts. ii. qualitative analysis and numerical simulations. *Proceedings of the Royal Society A: Mathematical, Physical and Engineering Science*, 465(2107):2267–2292, 2009.
- [42] R Cross. Impact of a ball on a surface with tangential compliance. *American Journal of Physics*, 78(7):716–720, 2010.
- [43] YB Jia, M Mason, and M Erdmann. A state transition diagram for simultaneous collisions with application in billiard shooting. In *Algorithmic Foundation of Robotics VIII*, pages 135–150. Springer, 2009.
- [44] YB Jia. Three-dimensional impact: energy-based modeling of tangential compliance. *The International Journal of Robotics Research*, 32(1):56–83, 2013.

- [45] PZ Qiao, M Yang, and F Bobaru. Impact mechanics and high-energy absorbing materials: review. *Journal of Aerospace Engineering*, 21(4):235–248, 2008.
- [46] G Darboux. Etude géométrique sur les percussions et le choc des corps. *Bulletin des Sciences Mathématiques et Astronomiques*, 4(1):126–160, 1880.
- [47] J Coaplen, WJ Stronge, and B Ravani. Work equivalent composite coefficient of restitution. *International journal of impact engineering*, 30(6):581–591, 2004.
- [48] B Crüger, V Salikov, S Heinrich, S Antonyuk, VS Sutkar, NG Deen, and JAM Kuipers. Coefficient of restitution for particles impacting on wet surfaces: An improved experimental approach. *Particuology*, 2015.
- [49] LJ Wang, WX Zhou, ZJ Ding, XX Li, and CG Zhang. Experimental determination of parameter effects on the coefficient of restitution of differently shaped maize in three-dimensions. *Powder Technology*, 284:187–194, 2015.
- [50] J Van Vliet, I Sharf, and O Ma. Experimental validation of contact dynamics simulation of constrained robotic tasks. *The International Journal of Robotics Research*, 19(12):1203–1217, 2000.
- [51] S Kolev and E Todorov. Physically consistent state estimation and system identification for contacts. In *Humanoid Robots (Humanoids), 2015 IEEE-RAS 15th International Conference on*, pages 1036–1043. IEEE, 2015.
- [52] JP Nobre, AM Dias, and R Gras. A study on elasto-plastic impact friction. *Wear*, 230(2):133–145, 1999.
- [53] M Eriten, CH Lee, and AA Polycarpou. Measurements of tangential stiffness and damping of mechanical joints: direct versus indirect contact resonance methods. *Tribology international*, 50:35–44, 2012.
- [54] G Gilardi and I Sharf. Literature survey of contact dynamics modelling. *Mechanism and machine theory*, 37(10):1213–1239, 2002.
- [55] R Cross. Increase in friction force with sliding speed. *American journal of physics*, 73(9):812–816, 2005.

- [56] Bo NJ Persson. *Sliding friction: physical principles and applications*, volume 1. Springer, 2000.
- [57] R Hartley and A Zisserman. *Multiple view geometry in computer vision*. Cambridge university press, 2003.
- [58] K Tagawa, K Hirota, and M Hirose. Manipulation of dynamically deformable object using impulse-based approach. *Advances in Haptics*, pages 16–33, 2010.
- [59] WH Huang and MT Mason. Mechanics, planning, and control for tapping. *The International Journal of Robotics Research*, 19(10):883–894, 2000.
- [60] T Higuchi. Application of electromagnetic impulsive force to precise positioning tools in robot systems. In *International Symposium on Robotics Research*, pages 281–285, 1985.
- [61] T Izumi and Y Kitaka. Control of a hitting velocity and direction for a hammering robot using a flexible link. *Journal of the RSJ*, 11(3):436–443, 1993.
- [62] S Hirai, M Niwa, and S Kawamura. Development of impulsive object sorting device with air floating. In *ICRA*, pages 3065–3070, 1999.
- [63] S Ahmed, HM Lankarani, and MFOS Pereira. Frictional impact analysis in open-loop multibody mechanical systems. *Journal of Mechanical Design*, 121(1):119–127, 1999.
- [64] J Heikkila and O Silvén. A four-step camera calibration procedure with implicit image correction. In *Computer Vision and Pattern Recognition, 1997. Proceedings., 1997 IEEE Computer Society Conference on*, pages 1106–1112. IEEE, 1997.
- [65] ZY Zhang. A flexible new technique for camera calibration. *IEEE Transactions on pattern analysis and machine intelligence*, 22(11):1330–1334, 2000.
- [66] RV Dukkipati, MA Rao, and RB Bhat. *Computer aided analysis and design of machine elements*. New Age International, 2006.

- [67] J Taylor. *Introduction to error analysis, the study of uncertainties in physical measurements*, volume 1. 1997.